

## ABSTRACT

Title of Dissertation:           Understanding and Mimicking the Fly's Directional Hearing: Modeling, Sensor Development, and Experimental Studies

Haijun Liu, Doctor of Philosophy, 2012

Dissertation directed by:       Professor Miao Yu  
Department of Mechanical Engineering

Microphone arrays have been widely used in sound source localization for many applications. In order to locate the sound in a discernible manner, the separation between microphones needs to be greater than a critical distance, which poses a fundamental constraint for the miniaturization of directional microphones. In nature, animal hearing organs are also governed by the size constraint; the smaller the organ size, the smaller the available directional cues for directional hearing. However, with an auditory organ separation of only 520  $\mu\text{m}$ , the fly *Ormia ochracea* is found to exhibit remarkable ability to pinpoint its host cricket at 5 kHz. The key to this fly's phenomenal directional hearing

ability is believed to be the mechanical coupling between the eardrums. This innovative solution can inspire one to find alternative approaches to tackle the challenge of developing miniature directional microphones.

The overall goal of this dissertation work is to unravel the underlying physics of the fly ear hearing mechanisms, and to apply this understanding to develop and study novel bio-inspired miniature directional microphones. First, through mechanics and optimization analysis, a fundamental biological conclusion is reached: the fly ear can be viewed as a nature-designed optimal structure that is endowed with the dual optimality characteristic of maximum average directional sensitivity and minimum nonlinearity, at its working frequency of 5 kHz. It is shown that this dual optimality characteristic is only achievable when the right mechanical coupling between the eardrums is used (i.e., proper contributions from both rocking and bending modes are used). More importantly, it is further revealed that the dual optimality characteristic of the fly ear is replicable in a synthetic device, whose structural parameters can be tailored to work at any chosen frequency. Next, a novel bio-inspired directional microphone with mechanically coupled diaphragms is designed to capture the essential dynamics of the fly ear. To study the performance of this design, a novel continuum mechanics model is developed, which features two coupling modules, one for the mechanical coupling of the two diaphragms through a beam and the other for each diaphragm coupled through an air gap. Parametric studies are carried out to explore how the key normalized parameters affect the performance of this directional microphone. Finally, this mechanics model is used to guide the development of a large-scale microphone and a fly-ear sized microphone, both

of which are experimentally studied by using a low-coherence fiber optic interferometric detection system. With the large-scale sensor, the importance of using proper contribution from both rocking and bending modes is validated. The fly-ear sized sensor is demonstrated to achieve the dual optimality characteristic at 8 kHz with a ten-fold amplification in the directional sensitivity, which is equivalent to that obtainable from a conventional microphone pair that is ten times larger in size. To best use this sensor for sound source localization, a robotic platform with a control scheme inspired by the fly's localization/lateralization scheme is developed, with which a localization accuracy of better than  $\pm 2^\circ$  (the same as the fly ear) is demonstrated in an indoor lab environment.

This dissertation work provides a quantitative and mechanistic explanation for the fly's sound localization ability for the first time, and it provides a framework for the development of fly-ear inspired acoustic sensors that will impact many fronts.

UNDERSTANDING AND MIMICKING THE FLY'S DIRECTIONAL HEARING:  
MODELING, SENSOR DEVELOPMENT, AND EXPERIMENTAL STUDIES

by

Haijun Liu

Dissertation submitted to the Faculty of the Graduate School of the  
University of Maryland, College Park in partial fulfillment  
of the requirements for the degree of  
Doctor of Philosophy  
2012

Advisory Committee:

Associate Professor Miao Yu, Chair  
Professor Bala Balachandran  
Professor Amr Baz  
Assistant Professor Jin-Oh Hahn  
Professor Inderjit Chopra, Dean's Representative

© Copyright by

Haijun Liu

2012

## Dedication

*To my wife Jing and my parents*

## Acknowledgements

First and foremost, I would like to express my sincere gratitude to my advisor, Professor Miao Yu. It is in the intellectual discussions with her that this dissertation was conceived, and it is her encouragement, insights, and support that have guided me through the five years. Whenever I was frustrated with the problems encountered in experiments or simulations, she is always there to help me with her thorough knowledge and generous patience. She challenges me to become a better scientist, and encourages me to pursue success in academia. The experience working with her benefited me and will keep benefiting me in my future career.

I would also like to thank Professor Bala Balachandran for his advice and help since my application to the graduate school at Maryland. He not only recommended me to join Prof. Yu's group, but has been instrumental in my research since. The scientific thinking and analytical skills I learned from his classes is a treasure that I will always value. I thank him for recommending me to the Future Faculty Program and letting me access his lab equipment for my research.

I am most thankful to other professors in my dissertation committee. I am indebted to the classes with Prof. Amr Baz and Prof. Inderjit Chopra. They are both so knowledgeable with their expertise area that they can lecture without notes. Their enthusiasm in scientific academia and precise and critical way of doing research has inspired my passion in pursuing academic career. Prof. Sarah Bergbreiter provided me very constructive

comments on my dissertation proposal with her immense expertise in micro-fabrication and micro-robotics. I would also like to thank Prof. Jin-Oh Hahn, who was generous enough to agree to serve on my committee in the last minute and offered help. All in all, I thank them for serving on my dissertation committee and their valuable advice on my research.

I also want to thank all the colleagues and friends in the Sensors and Actuators Lab, Yuxiang Liu, Zhong Chen, Dr. Xuming Zhang, Hyungdae Bae, Cheng Pang, Felix Stief, Laith Sawaqed, Andrew Lisiewski, and Zhijiang Zhang. Their support and friendship makes my life at College Park enjoyable and memorable. Specific thanks go to Yuxiang, who helped me set up the optical detection system early in my research and has given me his sincere and valuable advice whenever I seek for his help. I appreciate the help from Dr. Luke Currano, Danny Gee, and Tristan Helms on the MEMS device fabrication. I also appreciate the generosity of Nick Vlajic for accommodating my use of the equipment in Prof. Balachandran's lab.

My deepest gratitude goes to my wife, Jing, for her love and sacrifice. She was the reason that I came to the United States and applied to the graduate school at UMD. Without her company over the last dozen years, my life would not have been so colorful and full of joy. I also want to thank my parents, my sister, and my parents-in-law for their unconditional love and support through the years.



# TABLE OF CONTENTS

<b>CHAPTER 1 INTRODUCTION AND BACKGROUND.....</b>	<b>1</b>
1.1 PROBLEM OF INTEREST .....	1
1.2 PREVIOUS WORK.....	5
1.2.1 <i>Directional hearing in insects</i> .....	5
1.2.2 <i>Fly-ear inspired directional microphones</i> .....	12
1.3 MOTIVATION FOR THIS DISSERTATION WORK.....	18
1.4 OVERVIEW OF THE DISSERTATION WORK .....	21
<b>CHAPTER 2 UNDERSTANDING THE BIO-PHYSICS OF THE FLY EAR: DUAL-OPTIMALITY .....</b>	<b>24</b>
2.1 LUMPED MODEL OF THE FLY EAR AND ITS ANALYTICAL SOLUTION .....	24
2.2 PARAMETRIC STUDIES.....	32
2.2.1 <i>Stiffness ratio</i> .....	32
2.2.2 <i>Damping</i> .....	36
2.2.3 <i>Separation-to-wavelength ratio</i> .....	39
2.3 DUAL-OPTIMALITY IN THE FLY EAR.....	42
2.4 MIMICKING THE FLY EAR'S DUAL-OPTIMALITY.....	48
2.5 SUMMARY .....	52
<b>CHAPTER 3 FLY-EAR INSPIRED DIRECTIONAL MICROPHONES: DESIGN AND MODEL DEVELOPMENT .....</b>	<b>55</b>
3.1 FLY-EAR INSPIRED DIRECTIONAL MICROPHONE DESIGN.....	55
3.2 OVERVIEW OF MODEL DEVELOPMENT.....	56
3.3 MODELS OF INDIVIDUAL COMPONENTS OF THE SENSOR STRUCTURE .....	59
3.3.1 <i>Diaphragm</i> .....	59
3.3.2 <i>Air gap</i> .....	63
3.3.3 <i>Bridge</i> .....	66

3.4	DIAPHRAGM COUPLED WITH AN AIR GAP .....	71
3.4.1	<i>Continuum mechanics model</i> .....	74
3.4.2	<i>Simplified model</i> .....	76
3.4.3	<i>Parametric studies</i> .....	88
3.5	MODELING OF DIAPHRAGMS COUPLED THROUGH A BRIDGE.....	90
3.6	VALIDATION OF THE CONTINUUM MECHANICS MODEL .....	97
3.6.1	<i>Validation of the model with a finite element model</i> .....	97
3.6.2	<i>Comparison of the continuum mechanics model with the lumped model</i> .....	100
3.7	PARAMETRIC STUDIES.....	102
3.7.1	<i>Air gap height</i> .....	104
3.7.2	<i>Young's modulus of the coupling bridge</i> .....	105
3.7.3	<i>Density of the coupling bridge</i> .....	106
3.8	SUMMARY .....	107
<b>CHAPTER 4 FLY-EAR INSPIRED DIRECTIONAL MICROPHONES: SENSOR SYSTEM</b>		
<b>DEVELOPMENT AND EXPERIMENTAL STUDIES..... 109</b>		
4.1	OVERVIEW OF SENSOR SYSTEM DEVELOPMENT .....	109
4.2	DEVELOPMENT OF OPTICAL DETECTION SYSTEM.....	110
4.3	LARGE-SCALE PROOF-OF-CONCEPT DIRECTIONAL MICROPHONE .....	116
4.4	DEVELOPMENT OF A MICRO-SCALED SENSOR MIMICKING THE FLY-EAR'S DUAL OPTIMALITY CHARACTERISTIC .	120
4.4.1	<i>Sensor design based on dual-optimality</i> .....	120
4.4.2	<i>Sensor fabrication</i> .....	123
4.4.3	<i>Experiment study of the MEMS sensor</i> .....	126
4.5	FLY INSPIRED LOCALIZATION SCHEME.....	130
4.6	SUMMARY .....	135
<b>CHAPTER 5 SUMMARY..... 137</b>		
5.1	SUMMARY OF THE DISSERTATION WORK.....	137
5.2	FUTURE WORK.....	142
<b>APPENDIX A: MATLAB CODES AND ANSYS INPUT FILES..... 145</b>		
A1	MATLAB CODES FOR THE LUMPED TWO DEGREES-OF-FREEDOM MODEL.....	145

A2	MATLAB CODES FOR PROCESSING THE ACQUIRED SIGNALS TO CALCULATE DIRECTIONAL CUES.....	147
A3	MATLAB CODES FOR THE CONTINUUM MECHANICS MODEL .....	150
A4	ANSYS INPUT FILES.....	156
<b>APPENDIX B: LIST OF PUBLICATIONS .....</b>		<b>160</b>
<b>BIBLIOGRAPHY .....</b>		<b>162</b>

## LIST OF TABLES

Table 2-1: Parameters used in the lumped model for the fly ear (Miles et al., 1995).....	25
Table 3-1: Natural frequency and mode shapes of circular clamped plate without in-plane tension .....	62
Table 3-2: Natural frequencies (normalized) of center-pinned beams (zero axial load).....	70
Table 3-3: Parameters of a representative fly-ear inspired directional microphone .....	98
Table 3-4: Mode shapes and natural frequencies of mechanically coupled microphone without air gap (comparison between analytical model and finite element model) .....	99
Table 3-5: Mode shapes and natural frequencies of mechanically coupled microphone with air gap (comparison between analytical model and finite element model) .....	99
Table 4-1: Parameters of the large-scale directional microphone.....	118

## LIST OF FIGURES

Figure 1-1: An inherently directional microphone for hearing aid: (a) schematic; (b) a cardioid shaped directivity pattern. ....	2
Figure 1-2: Tymapnal ears in insects. Pure pressure receivers in large noctuid moths (a). Pressure difference receivers in locusts and grasshoppers (b), bushcrickets (c), field crickets (d). Mechanically coupled pressure receivers in tachinid flies (e), and sacrophagid flies (f). (Popper & Fay, 2005).....	6
Figure 1-3: Photographs of fly <i>Ormia ochracea</i> on the back of a cricket. (Lab of Prof. Ronald R. Hoy, <a href="http://hoylab.cornell.edu">http://hoylab.cornell.edu</a> ) .....	8
Figure 1-4: Equivalent lumped model (two degrees-of-freedom (2-DOF) model ) of the fly ear where each eardrum is modeled as a rigid bar supported by a spring ( $k_1$ , $k_2$ ) and a dashpot ( $c_1$ , $c_2$ ), and the bridge connecting the two eardrums is modeled as a combination of a spring ( $k_3$ ) and a dashpot ( $c_3$ ). (Miles et al., 1995).....	8
Figure 1-5: The auditory acuity of the fly ear. (a) The acoustical inputs. ITD is 1.45 $\mu$ s and IID is too small to be measured. (b) The mechanically coupled tympanal ears to amplify the acoustical inputs. (c) Directional cues at the mechanical response level. <i>mITD</i> is about 50 $\mu$ s. (d) Time difference at the neural level compared with ITD and <i>mITD</i> . (Robert & Göpfert, 2002) .....	10
Figure 1-6: Coding schemes for directional sensitivity in the auditory system of the fly <i>Ormia</i> . (a) Latency coding scheme where there is a latency difference in the spikes of the predominant type 1 afferents. (b) Population coding scheme where the number of active afferents depends on the stimulus intensity. (Oshinsky & Hoy, 2002).....	11
Figure 1-7: Turn size of fly <i>Ormia ochracea</i> as a function of speaker azimuth. (Mason et al., 2001) .....	12
Figure 1-8: (a) A fly-ear inspired differential microphone (Miles et al., 2009). (b) A conventional pressure gradient microphone (Beranek, 1954) .....	13
Figure 1-9: The measured directivity pattern (black solid line) and the ideal pattern (red dashed line) of the diaphragm of a fly-ear inspired pressure differential microphone (Miles et al., 2009). The sound frequency is 800 Hz.....	16
Figure 1-10: A fly-ear inspired directional microphone developed by Touse et al. (a) Photograph of the sensor consisting of two square wings connected by a bridge and pinned to the substrate. The inset shows scanning electron microscope image of one section of the comb	

fingers used for electronic readout of amplitudes of wing oscillations. (b) Normalized directivity pattern compared to a sine wave at the bending mode natural frequency of 5931 Hz. (Touse et al., 2010).....	17
Figure 1-11: Microphone design with a gimbal supported diaphragm. (a) Top view of the circular diaphragm. (b) Cross-section view. (Saito et al., 2002) .....	18
Figure 2-1: Schematic of the fly ear and its equivalent two degrees-of-freedom model. ....	25
Figure 2-2: Vibration modes of the fly ear – rocking mode and bending mode. ....	26
Figure 2-3: Interpretation of <i>mIPD</i> and <i>mIID</i> on a complex plane. $\Gamma$ is the unit modal response ratio, and $\phi$ is the initial phase difference at the acoustic stimulus. <i>mIPD</i> is equal to the angle between $\overline{DB}$ and $\overline{DC}$ , and <i>mIID</i> is equal to the vector length ratio $ \overline{DC} / \overline{DB} $ . ....	30
Figure 2-4: Effects of the stiffness ratio $k_3/k_1$ on the phase difference <i>mIPD</i> . All the parameters used in the simulations are the fly ear’s structural parameters listed in Table 2-1, with $k_3$ modified for three scenarios $\eta = 2$ , $\eta = 4.36$ (fly ear’s case), and $\eta = 10$ . $k_3/k_1$ is related to the natural frequency ratio $k_3/k_1 = (\eta^2 - 1)/2$ . (a)-(c): Spectra of <i>mIPD</i> for azimuths of 10°, 30°, and 90°. (d)-(f): Spatial distributions of <i>mIPD</i> for frequencies of 2 kHz, 5 kHz, and 8 kHz. ....	34
Figure 2-5: Effects of the stiffness ratio $k_3/k_1$ on directional sensitivity <i>DS</i> . All the parameters used in the simulations are the fly ear’s structural parameters listed in Table 2-1, with $k_3$ modified for three scenarios $\eta = 2$ , $\eta = 4.36$ (fly ear’s case), and $\eta = 10$ . $k_3/k_1$ is related to the natural frequency ratio $k_3/k_1 = (\eta^2 - 1)/2$ . (a)-(c): Spectra of <i>DS</i> for azimuths of 10°, 30°, and 90°. (d)-(f): Spatial distributions of <i>DS</i> for frequencies of 2 kHz, 5 kHz, and 8 kHz. ...	35
Figure 2-6: Effects of the damping ratios on the phase difference <i>mIPD</i> . All the parameters used in the simulations are the fly ear’s structural parameters listed in Table 2-1, with the two damping ratios $\xi_1$ and $\xi_2$ modified for three scenarios, $\xi_1 = 0.10$ and $\xi_2 = 0.14$ , $\xi_1 = 0.50$ and $\xi_2 = 0.69$ , and $\xi_1 = 0.89$ and $\xi_2 = 1.23$ (fly ear’s case). (a)-(c): Spectrums of <i>mIPD</i> for azimuth 10°, 30°, and 90°. (d)-(f): Spatial distributions of <i>mIPD</i> for frequencies 2 kHz, 5 kHz, and 8 kHz. ....	37
Figure 2-7: Effects of the damping ratios on the directional sensitivity <i>DS</i> . All the parameters used in the simulations are the fly ear’s structural parameters listed in Table 2-1, with the two damping ratios $\xi_1$ and $\xi_2$ modified for three scenarios: $\xi_1 = 0.10$ and $\xi_2 = 0.14$ , $\xi_1 = 0.50$ and $\xi_2 = 0.69$ , and $\xi_1 = 0.89$ and $\xi_2 = 1.23$ (fly ear’s case). (a)-(c): Spectra of <i>DS</i> for azimuths 10°, 30°, and 90°. (d)-(f): Spatial distribution of <i>DS</i> for frequencies 2 kHz, 5 kHz, and 8 kHz. ....	38
Figure 2-8: Effects of the interaural separation $d$ on the phase difference <i>mIPD</i> . All the parameters used in the simulations are the fly ear’s structural parameters listed in Table 2-1, with $d$ modified for three scenarios, $d = 0.4$ mm, $d = 1.2$ mm (fly ear’s case), and $d = 3.6$ mm. (a)-(c): Spectra of <i>mIPD</i> for azimuths of 10°, 30°, and 90°. (d)-(f): Spatial distributions of <i>mIPD</i> for frequencies of 2 kHz, 5 kHz, and 8 kHz. ....	40

Figure 2-9: Effects of the interaural separation $d$ on the directional sensitivity $DS$ . All the parameters used in the simulations are the fly ear's structural parameters listed in Table 2-1, with $d$ modified for three scenarios, $d = 0.4$ mm, $d = 1.2$ mm (fly ear's case), and $d = 3.6$ mm. (a)-(c): Spectra of $DS$ for azimuth $10^\circ$ , $30^\circ$ , and $90^\circ$ . (d)-(f): Spatial distributions of $DS$ for frequencies 2 kHz, 5 kHz, and 8 kHz. ....	41
Figure 2-10: Phase difference $mIPD$ at 5 kHz as a function of azimuth for different coupling strength scenarios: stiff (natural frequency ratio $\eta = 20$ ), fly ear ( $\eta = 4.36$ ), soft ( $\eta = 2$ ), and uncoupled ( $\eta = 1$ ). The results are obtained by using the fly ear's structural parameters with varying bridge stiffness $k_3$ . ....	44
Figure 2-11: Directional sensitivity $DS$ at 5 kHz as a function of azimuth for different coupling strength scenarios: stiff (natural frequency ratio $\eta = 20$ ), fly ear ( $\eta = 4.36$ ), soft ( $\eta = 2$ ), and uncoupled ( $\eta = 1$ ). The results are obtained by using the fly ear's structural parameters with varying bridge stiffness $k_3$ . (a) and (b) are shown in different scales for clarity. ....	45
Figure 2-12: Dual-optimality of the fly-ear and fly-ear inspired sensor. (a) $DS$ at three different frequencies. (b) Spectra of average directional sensitivity ( $ADS$ ) and nonlinearity ( $NL$ ). ....	46
Figure 2-13: Contour of (a) $mIPD$ and (b) $DS$ in the space of azimuth and frequency for the rigid system in Figure 2-11. ....	48
Figure 2-14: Natural frequencies (normalized by the optimal working frequency) obtained in optimization analysis to ensure dual-optimality characteristic as a function of the wavelength-to-separation ratio $\chi$ . (a) High damping case ( $\xi_1 = 0.89$ , $\xi_2 = 1.23$ ). (b) Low damping case ( $\xi_1 = 0.09$ , $\xi_2 = 0.12$ ). ....	49
Figure 2-15: Dual optimality of three designs, which have the same damping and center-to-center separation as the fly ear, to work at 2 kHz, 5 kHz, and 8 kHz, respectively. (a) Average directional sensitivity ( $ADS$ ) and nonlinearity ( $NL$ ) in the frequency domain. (b) Directional sensitivity in the spatial domain at the corresponding optimal working frequencies. ....	51
Figure 2-16: Three design examples with different damping scenarios, given the same center-to-center separation (1.2mm) and working frequency of 5 kHz as the fly ear. (a) $ADS$ and $NL$ in the frequency domain. (b) Variation of $DS$ at frequencies slightly off the optimal frequency for the low damping system ( $\xi_1 = 0.09$ , $\xi_2 = 0.12$ ). (c) Variation of $DS$ at frequencies slightly off the optimal frequency for the high damping system ( $\xi_1 = 0.89$ , $\xi_2 = 1.23$ ). ....	52
Figure 3-1: A fly-ear inspired directional microphone. (a) Schematic. (b) Cross-section view. ....	56
Figure 3-2: Mechanical analog of the fly's hearing organ. (a) The two prosternal tympanal membranes (PTM) are connected by a cuticular intertympanal bridge (K3). $K_3'$ is the stiffness due to the air space of the tracheal sac. (b) A mechanical stimulation is applied to one end of the bridge by a vibrating pin. One side of the air space is opened to study the relative contribution of $K_3$ and $K_3'$ . (Robert et al., 1998). ....	57
Figure 3-3: Coordinate system for the circular clamped diaphragm. ....	60

Figure 3-4: Cylindrical air gap with rigid walls and a top surface. (a) Coordinate system. (b) Cross-section view. ....	64
Figure 3-5: First three mode shapes of the beam (zero axial load). ....	70
Figure 3-6: A pressure sensor diaphragm backed by an air gap. (a) Schematic of the coordinate system. (b) Cross-section view. ....	74
Figure 3-7: Static sensitivity of the center displacement of a diaphragm backed by air gaps with respect to air gap height. The static sensitivity is normalized by that for the same diaphragm without the air gap ( <i>in vacuo</i> ). ....	82
Figure 3-8: The fundamental frequency of an air-backed diaphragm (normalized by that of the same diaphragm <i>in vacuo</i> ) for various air gap heights. The diaphragm is made of silicon, and its dimensions are $500 \mu\text{m} \times 0.5 \mu\text{m}$ (radius $\times$ thickness). In this plot, the continuum model and simplified model are compared to the close-ended cavity and the diaphragm <i>in vacuo</i> . ....	83
Figure 3-9: Effects of number of modes used in the simplified model on the calculated fundamental frequency (normalized by that of the same diaphragm <i>in vacuo</i> ). The diaphragm is made of silicon, and its dimensions are $500 \mu\text{m} \times 0.5 \mu\text{m}$ (radius $\times$ thickness). ....	84
Figure 3-10: A 3-stage approximation of the fundamental frequency of an air-backed diaphragm (normalized by that of the same diaphragm <i>in vacuo</i> ) as air gap height changes. The diaphragm is made of silicon, and its dimensions are $500 \mu\text{m} \times 0.5 \mu\text{m}$ (radius $\times$ thickness). In this plot, the fundamental frequency (red solid line) is obtained by using the simplified model ( $N = 2, M = 2$ ). ....	85
Figure 3-11: The variation of the fundamental frequency of an air-backed diaphragm (normalized by that of the same diaphragm <i>in vacuo</i> ) as a function of air gap height. (a) The Young's modulus of the diaphragm changing from 0.5 to 100 times Silicon's. (b) The diaphragm's density changing from 0.1 to 10 times Silicon's. (c) Pressure level of the air gap changing from 0.01 atm to 1 atm (assuming the temperature does not change). (d) The diaphragm thickness changing from $0.2 \mu\text{m}$ to $10 \mu\text{m}$ . ....	89
Figure 3-12: Finite element modeling (ANSYS) of fly-ear inspired directional microphones. ....	97
Figure 3-13: Comparison of center displacement spectra of a fly-ear inspired directional microphone using the continuum mechanics model and the lumped model. (a) Without considering the effects of air gap. (b) Effects of air gap included. Incident azimuth is $90^\circ$ . The two diaphragms have the same responses. ....	101
Figure 3-14: Comparison of phase difference <i>mIPD</i> of a fly-ear inspired directional microphone obtained by using the continuum mechanics model and the lumped model. (a) Without air gap. (b) With the air gap included. ....	101
Figure 3-15: The effects of air gap on the natural frequencies of the fly-ear inspired directional microphone. (a) The natural frequencies of the first rocking mode and first bending mode as a function of the air gap height. (b) The ratio of the two natural frequencies. ....	105



Figure 3-16: The effects of the Young’s modulus of the diaphragm on the natural frequencies of the fly-ear inspired directional microphone. (a) The natural frequencies of the first and second rocking modes and bending modes as a function of Young’s modulus ratio. (b) The ratio of natural frequencies to the first rocking mode natural frequency. .... 106

Figure 3-17: The effects of the diaphragm’s density on the natural frequencies of the fly-ear inspired directional microphone. (a) The natural frequencies of the first and second rocking modes and bending modes as a function of the density ratio. (b) The ratio of natural frequencies to the first rocking mode frequency. .... 107

Figure 4-1: Overview of the sensor system development. (a) Mechanical part which consists of two diaphragms coupled by a bridge. (b) Detection system where a fiber optic interferometric detection system is used. .... 110

Figure 4-2: Schematics of two beam interferometers: (a) Mach-Zehnder, (b) Fabry-Perot, and (c) Michelson. (Wild & Hinckley, 2008)..... 112

Figure 4-3: Basic configuration of low coherence fiber optic interferometric system ..... 114

Figure 4-4: schematic of a low-coherence fiber optic interferometric system for the fly-ear inspired directional microphone..... 115

Figure 4-5: Photograph of large-scale bio-inspired directional microphone. The separation between the two diaphragm centers is 25.4 mm (one inch). .... 116

Figure 4-6: Low-coherence fiber optic interferometer system using one tunable filter for the large-scale bio-inspired directional microphone. .... 118

Figure 4-7: Directional cues of large-scale prototype. (a) *mITD* versus incident angle for 1.1 kHz; (b) *mITD* in the frequency domain when incident angle is fixed at 40°. (Liu, Yu, & Zhang, 2008) ..... 120

Figure 4-8: Design guideline based on the fly ear’s dual-optimality. (a) Optimal natural frequencies for designing fly-ear like systems (damping ratio  $\xi_1 = 0.18$ ,  $\xi_2 = 0.05$ ). With an interaural separation of 1.2 mm, three examples are marked on this plot for working frequencies at 2 kHz, 8 kHz, and 12 kHz, respectively, (b) Spectra of average directional sensitivity (*ADS*) and nonlinearity (*NL*) for the three examples in (a). (c) Spatial distribution of directional sensitivity (*DS*) for the three examples in (a) at their respective optimal working frequencies. (d) Spatial distribution of *DS* for the representative system B in (a) at three different frequencies..... 122

Figure 4-9: Design of a miniature MEMS directional microphone inspired by the fly ear. It consists of four layers, device layer (Layer 1), perforated holes plate (Layer 2), back chamber (Layer 3), and back plate (Layer 4). .... 123

Figure 4-10: Fabrication and assembly process of the bio-inspired sensor. (a)-(g) Fabrication process for the front plate layer. (h)-(j) Fabrication process for the remaining three layers: damping layer, perforated holes layer, and back plate layer. (k) The assembled device after thermally bonding the four layers, inserting the fibers to the desired positions, and gluing them to the back plate layer using ultraviolet cured epoxy. .... 125

Figure 4-11: A fabricated MEMS directional microphone placed next to a house fly .....	126
Figure 4-12: Experimental setup to characterize the fabricated miniature directional microphone inspired by the fly ear.....	127
Figure 4-13: Phase difference <i>mIPD</i> for fabricated directional microphone inspired by the fly ear. (a) Experiment. (b) Simulation.....	128
Figure 4-14: Mode shapes obtained by laser Doppler vibrometer measurement for the miniature directional microphone inspired by the fly ear. (a) Rocking mode (9.8 kHz). (b) Bending mode (22.0 kHz).....	128
Figure 4-15: Dual-optimality of the fly-ear inspired directional microphone. (a) Spectra of averaged directional sensitivity ( <i>ADS</i> ) and nonlinearity ( <i>NL</i> ). It shows the device works best at 8 kHz, where it has maximal <i>ADS</i> and minimal <i>NL</i> . (b) Spatial distribution of phase difference <i>mIPD</i> at 8 kHz .....	130
Figure 4-16: Approximation of the relationship between the phase difference <i>mIPD</i> and azimuth $\theta$ by a sigmoid function (blue solid line). Red dots are experimental results. ....	131
Figure 4-17: An example of applying the bio-inspired sound source localization scheme for an initial azimuth of $80^\circ$ .....	132
Figure 4-18: Trajectories of sound source localization using fly's localization/lateralization scheme. (a) Trajectories when the fly's localization scheme is implemented on a fly-ear inspired sensor using a motorized rotational stage. Blue dots on the periphery represent the initial azimuth position, red dots near the origin are the final position, and magenta dots are the positions in between. (b) Virtual path of the fly in the phonotactic experiment (Mason et al., 2001).....	133
Figure 4-19: Estimation error using the fly-ear inspired sensor and bio-inspired localization/lateralization scheme. The mean and standard deviation of the error are $1.88^\circ$ and $0.85^\circ$ , respectively. ....	134
Figure 4-20: Tracking of a randomly moving source using the developed robotic platform. (a) Time history of the readings from the speaker and sensor stages. (b) Time history of the actual and estimated azimuths of the sound source.....	135

## **Chapter 1 Introduction and background**

### **1.1 Problem of interest**

Directional microphones have been widely used in a variety of applications for sound source localization, including hearing aid devices, robotic navigation, and underwater sensor networks (Brandstein & Ward, 2001). To build a directional microphone, there are mainly two approaches: either the microphone itself is inherently directional, or the microphone is omnidirectional but two or more of them form a microphone pair or array to extract directional cues (Csermak, 2000).

In inherently directional microphones, the net pressure force deflecting the diaphragm varies with incident azimuth. One example of inherently directional microphones used for hearing aids is illustrated in Figure 1-1(a). The acoustic waves travel along two paths to arrive at the diaphragm, the front wave (Wave B) acting on the external surface directly, the rear one (Wave A) experiencing a time delay due to the mechanical screen before reaching the internal side. The mechanical screen is typically designed to match the time difference of sound wave propagating from the rear port to the front port so that the sound coming from the rear is completely suppressed. On the other hand, the propagation distance difference is maximal for sound wave from the front, which is usually the sound of interest for the hearing aid wearers. Like a pressure gradient microphone (Beranek,

1954), the microphone's response is proportional to the pressure gradient times the propagation distance difference. The cardioid shape directivity pattern in Figure 1-1(b) shows the variation of the response as the incident azimuth changes. When it is used for sound source localization, the performance is determined by how the propagation distance difference will change with the azimuth, which is limited by the distance between the front port and the rear port. It should be noted that this type of directional microphone requires an extra sensor to measure the pressure or pressure gradient in order to decouple it from the azimuth in the directivity pattern.

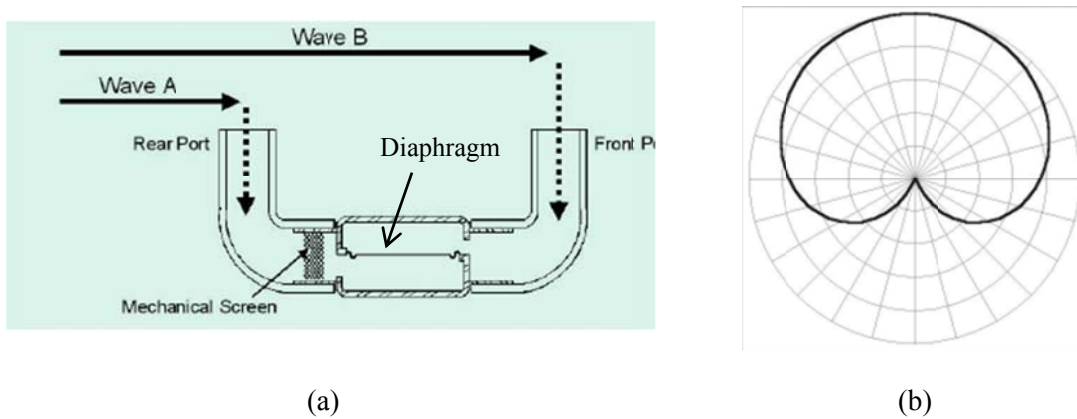


Figure 1-1: An inherently directional microphone for hearing aid: (a) schematic; (b) a cardioid shaped directivity pattern.

In the case of a microphone pair or array using omni-directional microphones, the most popular method to determine the sound direction is based on the time delay of arrival (TDOA) (Benesty, Chen, & Huang, 2008; Brandstein & Ward, 2001), which is proportional to the separation between microphones. Thus, in order for a microphone pair to detect the TDOA in some discernible manner, the microphones need to be separated greater than a critical distance. Such distance is dependent on a number of factors, including the signal-to-noise ratio (SNR), choice of estimator, number of samples, etc.

Therefore, no matter how the directional microphone is constructed, there is a fundamental size limit; the smaller the device size, the worse the localization performance. However, it is desirable to develop miniature directional microphones for many scenarios. One situation is when only miniature acoustic sensors are feasible, e.g., on a micro air vehicle (MAV) or in a hearing aid device where a smaller size is favored in order to be cosmetically acceptable for the hearing impaired individuals. A smaller size also means the perturbation to the primary sound field caused by the sensor itself is greatly reduced, enabling high accuracy measurements. Furthermore, miniaturization is advantageous from a physics viewpoint when the microphone array works in the near field, in which the far field or plane wave assumption made in the design and analysis of microphone arrays is no longer valid (Gay & Benesty, 2000). Many attempts have been undertaken to deal with near-field effects by using either modal expansion or multi-dimensional filter techniques (Asano, Asoh, & Matsui, 2000; Kennedy, Abhayapala, & Ward, 1998; Ryan & Goubran, 2000; Zheng, Goubran, & El-Tanany, 2004). Rather than compensating for wave-front curvature at the cost of computational complexity, by using miniature directional microphones, one can effectively deal with the near-field effects since the array's aperture can be chosen to be much smaller than the wave-front curvature (Brooks & Humphreys, 1999).

To develop miniature directional microphones for the above-mentioned applications and other applications, a solution needs to be sought to overcome the size constraint. The natural world has served as an inspiration for countless inventions and innovations, and it is conceivable that miniaturization of sensor technology can significantly benefit from

biology-inspired ideas (Bar-Cohen, 2006; Bhushan, 2009; Bleckmann, Schmitz, & Von der Emde, 2004; Vincent, Bogatyreva, Bogatyrev, Bowyer, & Pahl, 2006).

To detect the direction of a sound source, humans use the directional cues such as interaural intensity difference (IID), also known as interaural level difference (ILD), interaural time difference (ITD), and the spectral composition difference (Popper & Fay, 2005). When the dimension of the head is larger than one-tenth of the sound wavelength, the sound wave is disturbed (diffraction). In this case, human brain makes use of the spectra received from the two ears to estimate the direction of the sound wave, which are different with respect to most directions. In the case of a narrow-band sound source, the spectra difference reduces to IID at the center frequency. Human ears can also localize long pure tones that are less than 1400 Hz by extracting the TDOA at the two ears. Given that the average diameter of an adult head is 17 cm and the sound propagation speed in air is 344 m/s, this time difference is about 50 ms.

For much smaller insects, due to their limited capacities of frequency analysis, narrow-band sound is commonly detected. Because the part of the body that the ears are placed is about 10-50 times smaller than the human head, the diffraction occurs only at very high frequencies, and the expected maximum time difference is only in the ranges of tens of microseconds or even smaller (Hoy, Popper, & Fay, 1998). Even though they have much smaller directional cues in the sound stimulus and limited neural processing capability, some insects still possess phenomenal sound source localization abilities.

One striking example is found in the parasitoid fly *Ormia Ochracea*, which shows a remarkable ability to locate the calling song (at  $\sim 5$  kHz) of its host cricket even though

its ears are separated by only 520  $\mu\text{m}$  (Cade, 1975; Mason, Oshinsky, & Hoy, 2001; Robert, Amoroso, & Hoy, 1992; Walker, 1993). Despite the minute directional cues (the best possible ITD of 1.5  $\mu\text{s}$  and IID of less than 1 dB), the fly is able to localize the sound source with a resolution of  $2^\circ$  (Mason et al., 2001), which is equal to that of humans. The key to the fly's exceptionally accurate directional hearing is that the fly possesses a unique mechanical structure called the intertympanal bridge to couple the motions of the two tympanal membranes (eardrums) (Miles, Robert, & Hoy, 1995; Robert, Miles, & Hoy, 1996, 1998). With such a mechanically coupled structure, the IID and ITD at the mechanical response level are amplified significantly to 13 dB and 50  $\mu\text{s}$ , respectively (Robert et al., 1996). The time delay after neural processing is further amplified to 313  $\mu\text{s}$ , because the latency, defined as the time difference between the onset stimulus and the afferent neuron spike, increases as the stimulus intensity decreases (Mason et al., 2001; Oshinsky & Hoy, 2002).

This dissertation work is aimed to achieve enhanced understanding of the hearing mechanism of the fly ear and apply such understanding to the development of a novel miniature directional microphone to overcome the size constraint.

## **1.2 Previous work**

### **1.2.1 Directional hearing in insects**

The ears of insects can be classified into two categories, the flagellar ears and the tympanal ears (Hoy et al., 1998; Popper & Fay, 2005). The inherently directional flagellar ears (also called near-field detectors), such as the antennae in mosquitoes, are

sensitive to the air particle velocity of a sound field. There have been much more studies on the tympanal ears. Tympanal ears are characterized by three features, which include a tympanal membrane, an air-filled sac or tracheal expansion, and an associated chordotonal sensory organ (Hoy & Robert, 1996). There are three types of tympanal ears: pressure receivers, pressure difference receivers, and mechanically coupled receivers (Axel Michelsen & Larsen, 2008; Yager, 1999), as shown in Figure 1-2.

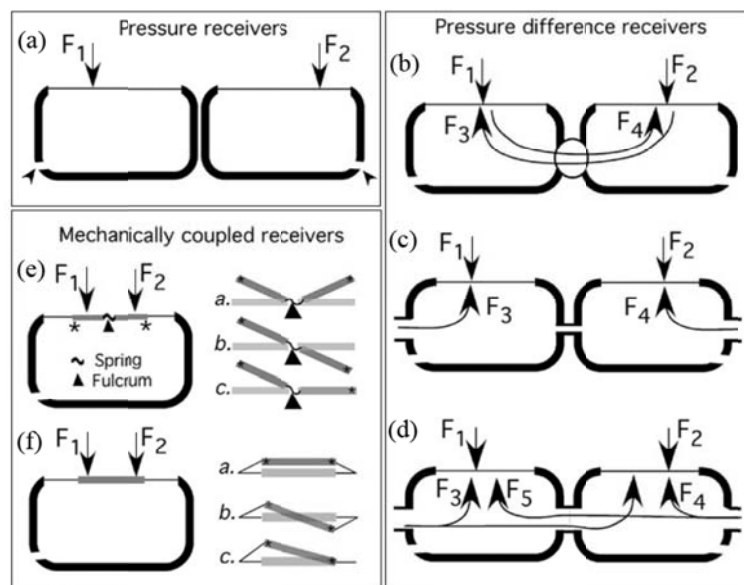


Figure 1-2: Tympanal ears in insects. Pure pressure receivers in large noctuid moths (a). Pressure difference receivers in locusts and grasshoppers (b), bushcrickets (c), field crickets (d). Mechanically coupled pressure receivers in tachinid flies (e), and sacrophagid flies (f). (Popper & Fay, 2005)

The main difference between the three types of ears is how the two ears are coupled. There is no coupling in the pure pressure receivers, see Figure 1-2(a). Due to the large size of this category of insects relative to the sound wavelength, the main directional cue used for the pressure receivers is IID. In the pressure difference receivers, shown in



Figure 1-2(b)-(d), the sound pressure are applied to both the external and internal surface of the tympanum. The vibration of the tympanum can be excited by the sound amplitude difference or by the phase difference. Due to the smaller size of the insects in this category (usually a fraction of sound wavelength), the frequency-dependent phase difference plays a more important role than the amplitude difference. The mechanically coupled pressure receivers are found in the smallest insects, such as the parasitoid flies, as shown in Figure 1-2(e)-(f). In this case, the pressure is applied only to the external surface of the tympanum. The average pressure causes the ipsilateral and contralateral ears to move in phase (called bending mode or translational mode), while the pressure difference causes the two ears to move out-of-phase (called rocking mode or rotational mode). A typical response of the ears is a combination of these two modes.

It has been found that the parasitoid fly *Ormia ochracea* (tachinid family) (Miles et al., 1995; Robert et al., 1996) has superior performance compared with the fly *Emblemasoma* sp. (sarcophagid family), which lacks a central fulcrum (Robert, Miles, & Hoy, 1999). The ear of the fly *Ormia ochracea* also differs significantly from that of the cricket hosts of both parasitoid flies, where the tympanal is a four-input pressure difference system (Axel Michelsen & Larsen, 2008; A. Michelsen, Popov, & Lewis, 1994).

By localizing the calling song of the male cricket, the parasitoid fly *Ormia ochracea* locates its host and deposits its larvae on it (Cade, 1975; Mason et al., 2001; Robert et al., 1992; Walker, 1993), as shown in Figure 1-3. Although its ears are separated by only 520  $\mu\text{m}$  (the best possible ITD of 1.5  $\mu\text{s}$  and IID of less than 1 dB) (Robert et al., 1996), a phonotactic experiment has shown that fly can resolve an azimuthal deviation as small as

2° when a loudspeaker was used to broadcast a cricket song (Mason et al., 2001). It has been found that the key to this remarkable localization ability is that the two tympana are coupled by a cuticular bridge pivoted about its center (Miles et al., 1995; Robert et al., 1996), as shown in Figure 1-4.



Figure 1-3: Photographs of fly *Ormia ochracea* on the back of a cricket. (Lab of Prof. Ronald R. Hoy, <http://hoylab.cornell.edu>)

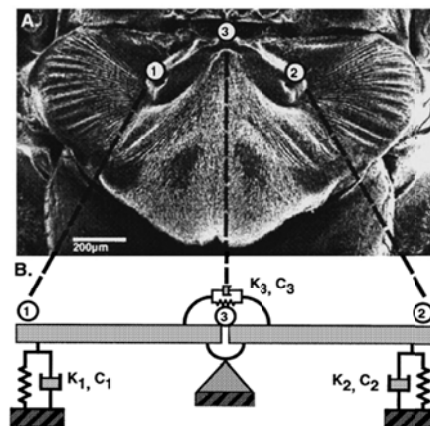


Figure 1-4: Equivalent lumped model (two degrees-of-freedom (2-DOF) model ) of the fly ear where each eardrum is modeled as a rigid bar supported by a spring ( $k_1$ ,  $k_2$ ) and a dashpot ( $c_1$ ,  $c_2$ ), and the bridge connecting the two eardrums is modeled as a combination of a spring ( $k_3$ ) and a dashpot ( $c_3$ ). (Miles et al., 1995)

The whole process from the acoustical input to the neural time difference is depicted in Figure 1-5. First, when the tympana are excited by a sound wave, the minute ITD and IID are transformed to the cues at the mechanical response level; that is, mechanical IID (*mIID*) and mechanical ITD (*mITD*). It is found that the ipsilateral tympanum is 50  $\mu$ s ahead of the contralateral one, and its amplitude is about 10 dB larger. Next, when the vibrations of the tympana are detected by the sensory organs (acoustical afferents), the directional cues are converted to the neuron latency, defined as the time delay between the sound stimulus and the first spike. It is striking that the latency difference between the two ears (neuron ITD) further amplifies *mITD* (Robert & Göpfert, 2002). The underlying mechanism is found to be the intensity-level dependent latency shift, in which the latency and the stimulus intensity are inversely related, as shown in Figure 1-6(a) (Oshinsky & Hoy, 2002). Finally, the neuron ITD is processed via the inter-neuron cross-correlation and a decision is made by the Central Nervous System (CNS).

In addition to the latency coding scheme as described above, the fly may use a population coding scheme, where the number of active afferents depends on the sound stimulus intensity, as shown in Figure 1-6(b). It is due to the fact that different afferents have different thresholds to elicit spikes.

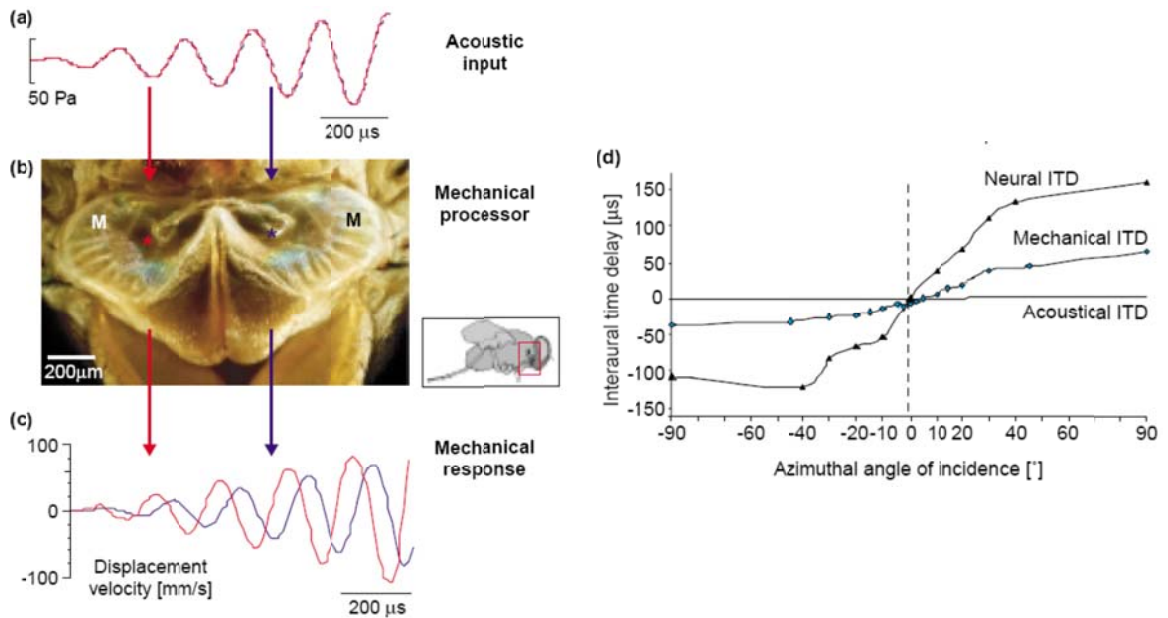
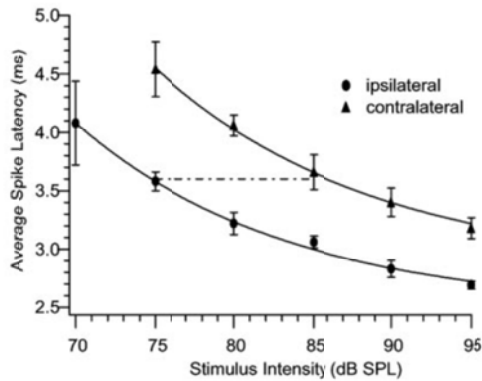
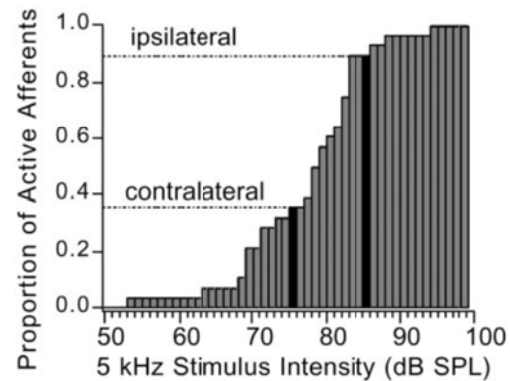


Figure 1-5: The auditory acuity of the fly ear. (a) The acoustical inputs. ITD is  $1.45 \mu\text{s}$  and IID is too small to be measured. (b) The mechanically coupled tympanal ears to amplify the acoustical inputs. (c) Directional cues at the mechanical response level. *mITD* is about  $50 \mu\text{s}$ . (d) Time difference at the neural level compared with ITD and *mITD*. (Robert & Göpfert, 2002)

In terms of the relationship of the coding scheme to the available directional cues (i.e., *mITD* and *mIID*), the latency coding uses a combination of both, while the population coding solely utilize *mIID*. Whether the latency or population coding scheme is used by the fly's CNS is not clear yet (Oshinsky & Hoy, 2002). However, it should be noted that in latency coding, the latency difference between the ipsilateral and contralateral afferents depends on the stimulus intensity, as shown in Figure 1-6(a). It has been shown that the neuron ITD increases with decreasing stimulus intensity. This may indicate the fly uses both coding schemes, which means both *mITD* and *mIID* are available to the fly for carrying out sound source localization.



(a)



(b)

Figure 1-6: Coding schemes for directional sensitivity in the auditory system of the fly *Ormia*. (a) Latency coding scheme where there is a latency difference in the spikes of the predominant type 1 afferents. (b) Population coding scheme where the number of active afferents depends on the stimulus intensity. (Oshinsky & Hoy, 2002)

Answers have been sought for an important question: when the directional cues are made available to the CNS, and how does the fly localize its cricket host? In the experiments carried out by Mason, et al, the fly was found to be able to reliably locate the sound source by continuously turning the midline of its head towards the speaker (Mason et al., 2001). When the turn size was measured as a function of the speaker azimuth, a sigmoid response curve was found, as shown in Figure 1-7. It was proposed that sound source localization ability of the fly is simply limited to lateralization when the source is beyond  $\sim 20^\circ$  azimuth, namely just deciding if the source is from the left or right. Only when the source is within  $\sim 20^\circ$  azimuth, the fly can truly localize the calling song.

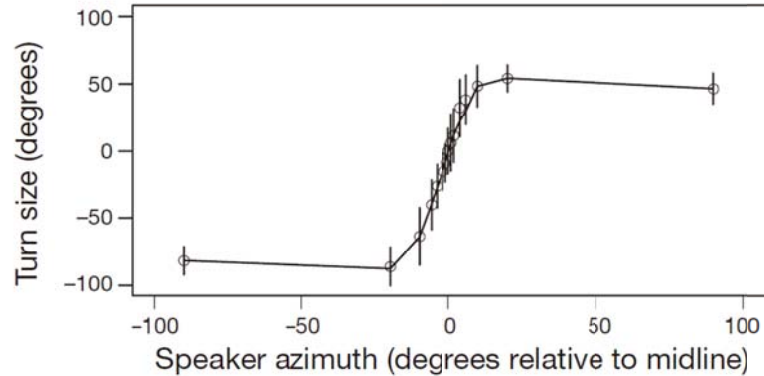


Figure 1-7: Turn size of fly *Ormia ochracea* as a function of speaker azimuth. (Mason et al., 2001)

In another study, the fly was found to have ability to distinguish the elevation in the vertical plane, but the performance is not as good as that in azimuth (Arthur & Hoy, 2006). Moreover, the phonotactic experiment carried out by Muller and Robert demonstrated that the fly can localize the sound source in three dimensions and land in the vicinity of a loudspeaker, even after the sound is turned off during the latter half of the trajectory (Muller & Robert, 2001).

### 1.2.2 Fly-ear inspired directional microphones

The observations of the directional hearing ability of the fly in the biological experiments have elicited a variety of research activities to study the fly's hearing mechanism from the mechanical perspective and to seek novel bio-inspired designs for sound localization..

Inspired by the fly ear, Miles et al have presented pioneering work in developing miniature directional microphones (Cui et al., 2006; Miles et al., 2009; Yoo, Gibbons, Su, Miles, & Tien, 2002). Guided by a two-degree-of-freedom (2-DOF) model (Miles et al., 1995), these microphones typically consist of two micro-machined poly-silicon plates that are supported by a flexible pivot, as shown in Figure 1-8(a). Typical dimensions of

these microphones are about  $1 \text{ mm} \times 2 \text{ mm}$ . When a sound wave is incident on these microphones, the pressure difference causes the two plates to rotate in opposite directions (rocking mode) while the average pressure causes them to move in the same direction (bending mode).

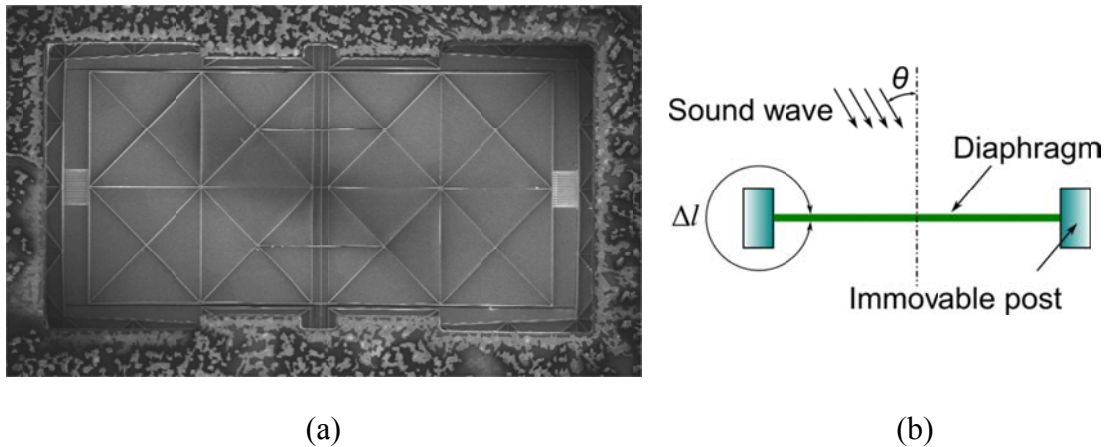


Figure 1-8: (a) A fly-ear inspired differential microphone (Miles et al., 2009). (b) A conventional pressure gradient microphone (Beranek, 1954) .

In these microphones, because the pivot is very compliant and the diaphragms are rib-reinforced, the natural frequency of the rocking mode (15220 Hz) is far higher than that of the bending mode (735 Hz) and the working frequency (800 Hz) (Miles et al., 2009). In this way, the influence of the bending mode to the microphone response is greatly suppressed, and the rocking mode is primarily utilized. The intention of this design is to make the diaphragm have a good rotational sensitivity even when subject to a minute sound pressure gradient (Miles et al., 2009).

In essence, the above mentioned differential microphones are similar to the conventional pressure gradient microphone as shown in Figure 1-8(b), in which the driving force is given by

$$f_D = \left( \frac{\partial p}{\partial x} \cos \theta \right) S \Delta l, \quad (1-1)$$

where  $S$  is the diaphragm area,  $\partial p/\partial x$  is the pressure gradient in the propagation direction  $x$ ,  $\Delta l$  is the sound propagation path difference, and  $\theta$  is the incident azimuth (Beranek, 1954). For comparison, in the design of the pressure differential microphone by Miles et al, the driving moment for the rocking mode is given by

$$M_D = \left( \frac{\partial p}{\partial x} \sin \theta \right) I_A, \quad (1-2)$$

where  $I_A$  is the area moment of inertia about the fulcrum (Miles et al., 2009). The difference is that the sound waves are applied to both sides of the diaphragm in the conventional design, while in microphones developed by Miles group, the sound wave is applied on the external side of a rigid plate that rotates about its pivot.

As for the detection method, a Polytec laser vibrometer (OFV 302 optical head and OFV-2100 electronics unit) is used in the early system (Yoo et al., 2002). Later designs (Cui et al., 2006; Miles et al., 2009) are based on an optical detection system demonstrated by Hall et al (Hall et al., 2005; Hall & Degertekin, 2002; Hall, Okandan, Littrell, Bicen, & Degertekin, 2007). The structure is similar to a typical capacitive acoustic sensor, except the back electrode is shaped as an optical diffraction grating used in an optical interferometer system, which uses vertical-cavity surface-emitting laser (VCSEL) as the light source. The diaphragm deflection is obtained by measuring the intensity of reflected beams with different diffraction orders. A bias voltage is applied to the two plates to adjust the initial gap to achieve maximal sensitivity.



The directivity pattern achieved by this differential microphone is a figure eight pattern, as shown in Figure 1-9 for its response to an 800 Hz sound wave (Miles et al., 2009). To obtain this directivity pattern, the sound source is at a fixed location above the diaphragm plane while the microphone is mounted on a rotational stage. In this setup, it is assumed that the pressure gradient is constant at the microphone, and as a result its response is proportional to  $|\cos\theta|$ , where  $\theta$  is the azimuth angle.

Another similar fly-ear inspired directional microphone is shown in Figure 1-10(a), which makes use of a comb fingers based electronic readout (Touse et al., 2010). It consists of two square wings ( $1\text{ mm} \times 1\text{ mm}$ ) connected by a  $500\text{ }\mu\text{m}$  bridge. The entire substrate under the wings is removed to prevent the squeezed film damping. The two natural frequencies are at 2689 Hz and 5931 Hz, which were measured by a laser vibrometer. Because of the large surface area of the flexible wings, the measured frequency response of the microphone has a much higher peak at the bending mode natural frequency than that at the rocking mode natural frequency, which is different from that obtained from the microphone developed by Miles group (Miles et al., 2009).

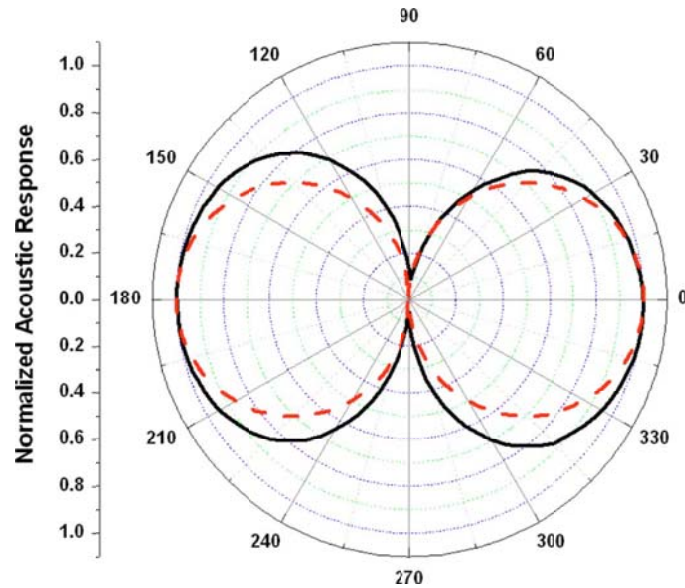


Figure 1-9: The measured directivity pattern (black solid line) and the ideal pattern (red dashed line) of the diaphragm of a fly-ear inspired pressure differential microphone (Miles et al., 2009). The sound frequency is 800 Hz.

When this microphone is excited by a sound wave at the bending mode frequency, the sound wave reaches the front and back sides of the wings through different propagation paths. Similar to conventional pressure gradient microphones, the net sound pressure that bends the flexible wings is proportional to  $|\cos\theta|$ , when the sound wavelength is much larger than the sensor dimensions. As a result, a  $|\cos\theta|$  pattern is observed for its angular response, as shown in Figure 1-10(b).

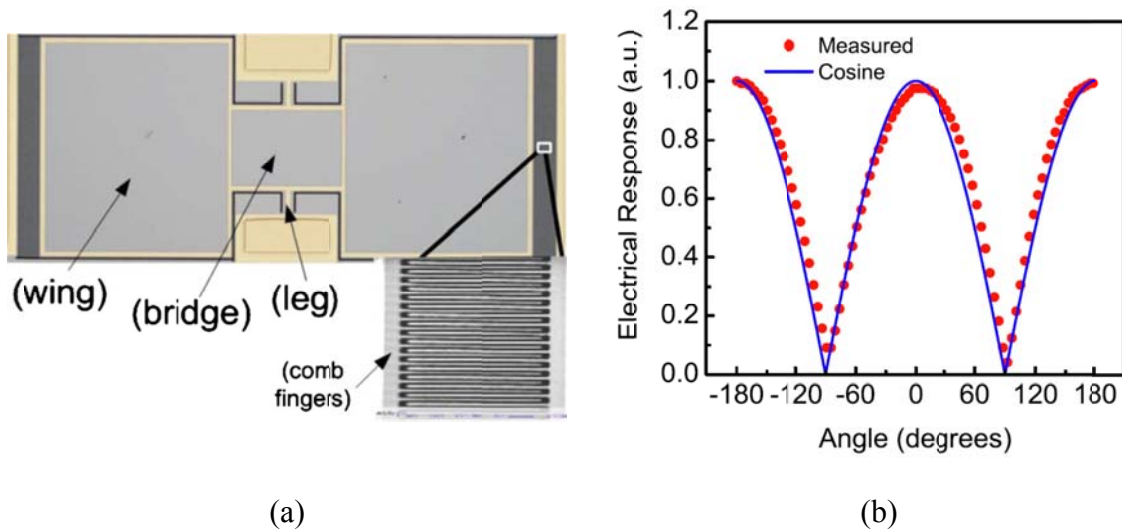


Figure 1-10: A fly-ear inspired directional microphone developed by Touse et al. (a) Photograph of the sensor consisting of two square wings connected by a bridge and pinned to the substrate. The inset shows scanning electron microscope image of one section of the comb fingers used for electronic readout of amplitudes of wing oscillations. (b) Normalized directivity pattern compared to a sine wave at the bending mode natural frequency of 5931 Hz. (Touse et al., 2010)

In another design, a circular bronze diaphragm with its center supported by a gimbal is proposed (Ono, Arita, Senjo, & Ando, 2005; Ono, Saito, & Ando, 2003; Saito, Ono, & Ando, 2002), as shown in Figure 1-11. The radius and thickness of the diaphragm are 10.8 mm and 30  $\mu\text{m}$ , respectively. This diaphragm structure has one in-phase mode and two out-phase modes for localization of the sound source in a two-dimensional plane.

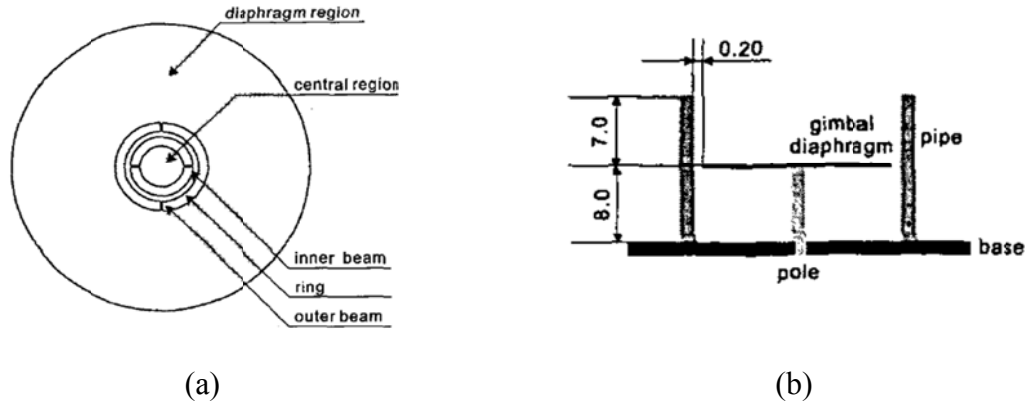


Figure 1-11: Microphone design with a gimbal supported diaphragm. (a) Top view of the circular diaphragm. (b) Cross-section view. (Saito et al., 2002)

A laser vibrometer is used to detect the vibrations at four points on the diaphragm (forming a  $10 \text{ mm} \times 10 \text{ mm}$  square), from which the in-phase and two reversed-phase waveforms can be calculated. Because the wavelength is much larger than the diameter of the diaphragm, the in-phase vibration is independent of the sound source location. Thus, from the two reversed-phase waveforms, the azimuth and elevation angles can be obtained.

More recently, another gimbal diaphragm design with a clover-stem-like structure as the center pivot is reported (Chen & Cheng, 2012). The analysis shows that this new design can achieve 47% improvement of net diaphragm displacement.

### 1.3 Motivation for this dissertation work

While it appears that the puzzle of the fly-ear mechanism has been solved, there are still many unresolved questions about the fly's superior sound source localization capability. To unravel the underlying science of the fly ear, this dissertation seeks to answer the following important but largely unexplored fundamental questions: i) how have the

structural parameters of the fly ears been tailored for achieving its superior localization ability at 5 kHz, ii) does the fly ear represent a natural optimal structure to facilitate the fly's unique localization-lateralization scheme, and iii) can a synthetic device be developed to truly replicate the fly-ear characteristics.

Furthermore, another goal of the dissertation work is to develop novel fly-ear inspired miniature directional microphones for sound source localization. Although various fly-ear inspired directional microphones have been proposed and developed, there are several major limitations in the existing work.

First, the key to the superior directional hearing of the fly *Ormia ochracea* is the mechanical coupling, which enables great amplification of the minute directional cues at the acoustic stimulus level to much higher values at the mechanical response level (Miles et al., 1995). Moreover, the coupling bridge in the fly ear has a finite stiffness, which suggests that proper contribution from both the rocking and bending modes of the fly ear structure are utilized. However, in the differential microphone design (Miles et al., 2009), the rocking mode is greatly suppressed, and only the bending mode is used. Similarly, in a later reported directional sound sensor, only the second mode (bending mode) is used (Touse et al., 2010).

Second, the above mentioned directional microphones (Miles et al., 2009; Touse et al., 2010) have a similar working principle to a conventional pressure gradient microphone, in which the response amplitude depends not only on the sound source direction, but also on the sound stimulus intensity or the pressure gradient. This is similar to a monaural hearing system. Due to the limitation of such a system, an additional sensor is required to

measure the local sound pressure or pressure gradient in order to determine the sound source direction (Miles et al., 2009; Touse et al., 2010). In contrast, mostly animals, including the fly *Ormia ochracea*, rely on binaural hearing in which the difference between the signals received by the auditory organs is utilized. These interaural directional cues are usually much more reliable and accurate than the purely intensity based monaural hearing, as they are independent of the excitation sound level.

Third, to detect the minute diaphragm response in miniature microphones, a detection system with high sensitivity and large signal-to-noise ratio (SNR) is needed. There are a variety of methods that have been used to detect the deflection of the diaphragm, including piezo-resistive, capacitive, and optical techniques (Eaton & Smith, 1997). Touse group uses an electronic readout with comb fingers to implement a capacitive detection system (Touse et al., 2010). Although it has better pressure sensitivity and less temperature sensitivity over piezo-resistive microphones, capacitive detection technique suffers by the excess signal loss from parasitic capacitance and the requirement of expensive and bulky high-impedance preamps at the sensor head. In addition, when the size is reduced, capacitive microphones are very susceptible to the mechanical noise due to molecular agitation, and thus a tradeoff has to be made between the sensitivity and the noise floor. Miles group intended to use the diffraction-based optical displacement detection system (Hall et al., 2005). However, this optical detection system has not been integrated with its directional microphone design yet, and the data reported in the literature were obtained by using laser Doppler vibrometer (Miles et al., 2009). In this dissertation work, a versatile and robust detection system based on low-coherence fiber

optic interferometry will be developed. It has advantages of optical microphones include high pressure sensitivity, high SNR, immunity to electromagnetic interference (EMI), and safety in hazardous and explosive environments.

#### **1.4 Overview of the dissertation work**

The overall goal of this dissertation work is to develop an enhanced understanding of the underlying science of the fly ear's hearing mechanism and use this understanding to design, develop, and study a novel bio-inspired miniature directional microphone for sound source localization.

This dissertation work includes the following three research thrusts.

**Research thrust 1: Achieve an enhanced understanding of the underlying science of the fly's hearing mechanism.**

Based on the equivalent 2-DOF model of the fly ear and its structural parameters reported in the literature, this research thrust is aimed to provide a quantitative and mechanistic explanation for the fly's superior sound localization ability at 5kHz and establish a correlation between the fly ear's structural characteristics and its localization performance. The gained understanding will be used to establish a framework for developing synthetic devices that can capture the characteristics of the fly-ear.

**Research thrust 2: Carry out analytical and numerical investigations into a fly-ear inspired sensor with structurally coupled diaphragms.**

In this research thrust, a fly-ear inspired directional microphone design is proposed that fully incorporates the fly ear's mechanical coupling mechanism and its unique characteristics revealed in the first research thrust. To achieve a fundamental understanding of the structural dynamics of the sensor, a continuum mechanics model will be developed first, which will feature two coupling modules, one for the mechanical coupling of the two diaphragms through a bridge and the other for each diaphragm coupled through an air-backed cavity. Parametric studies will then be conducted to investigate the effects of key parameters on the sensor performance.

**Research thrust 3: Develop novel fly-ear inspired directional microphones and carry out experimental studies on these microphones for sound source localization.**

In this research thrust, the established framework and mechanics model for the fly-ear inspired directional microphone will be first used to develop a large-scale proof-of-concept sensor. A low-coherence fiber optic interferometer system will be developed to detect the microphone's responses. Following a similar approach, a fly-ear sized miniature directional microphone will be developed, which captures the fly ear's essential characteristics. Moreover, a fly-ear inspired localization/lateralization scheme will be developed and implemented on a robotic system that aims to achieve a comparable localization accuracy of the fly.

The rest of this dissertation is organized as following. In Chapter 2, by using an equivalent 2-DOF model, the fly ear's unique characteristic, i.e., dual optimality at its working frequency 5 kHz, will be revealed and studied. Then, a framework will be established to mimic the fly's dual optimality feature in a synthetic device for any



frequency or size. In Chapter 3, the design of a bio-inspired directional microphone will be described, and a continuum mechanics model will be developed and used to study the performance of the bio-inspired directional microphone. The effects of an air gap on the sensor characteristics will also be investigated. In Chapter 4, the detection system based on low-coherence fiber optic interferometer will be described. The fabrication process and experiment results of a large-scale proof-of-concept directional microphone will be presented. Then, the previously established framework will be used to develop a fly-ear sized acoustic sensor that has dual optimality characteristic at 8 kHz. Further, a bio-inspired localization scheme will be implemented on a robotic platform. In Chapter 5, the dissertation work and the contributions will be summarized along with an outline for future work.

## **Chapter 2 Understanding the bio-physics of the fly ear: dual-optimality**

In the literature (Miles et al., 1995), a two-degree-of-freedom (2-DOF) model of the fly ear has been used to investigate the exceptional directional hearing ability of the fly. However, no further efforts have been made to explain whether the fly ear represents a natural optimal design and how the structural parameters of the fly ear are evolved to facilitate the superior localization performance at its working frequency of 5 kHz. Furthermore, the fly's unique localization/lateralization scheme (Mason et al., 2001) has never been well understood. In this chapter, the equivalent 2-DOF model and the fly ear parameters obtained experimentally (Miles et al., 1995) will be used to unravel the underlying physics of the fly ear mechanism.

### **2.1 Lumped model of the fly ear and its analytical solution**

In the 2-DOF model (Miles et al., 1995), as shown in Figure 2-1, each tympanum is modeled as a mass-spring-dashpot system, i.e. a mass ( $m_1$ ,  $m_2$ ) supported by a spring ( $k_1$ ,  $k_2$ ) and a dashpot ( $c_1$ ,  $c_2$ ). The two masses are connected by a torsion spring  $k_3$  and a dashpot  $c_3$ . All the parameters used to study the fly ear structure are listed in Table 2-1 as reported in the literature (Miles et al., 1995).

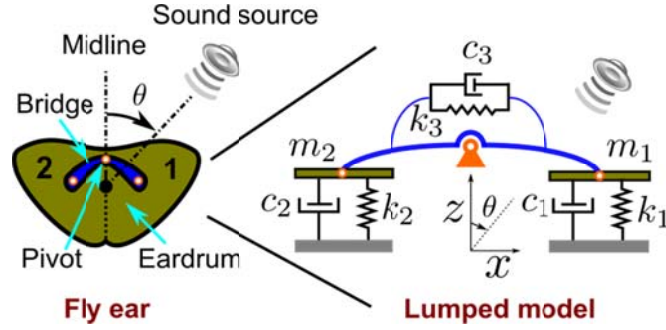


Figure 2-1: Schematic of the fly ear and its equivalent two degrees-of-freedom model.

Table 2-1: Parameters used in the lumped model for the fly ear (Miles et al., 1995)

Parameters	Values
Mass of bar $m$	$2.88 \times 10^{-10}$ kg
Translational spring $k_1, k_2$	0.576 N/m
Translation dashpot $c_1, c_2$	$1.15 \times 10^{-5}$ N s/m
Torsional spring $k_3$	5.18 N/m
Torsional dashpot $c_3$	$2.88 \times 10^{-5}$ N s/m
Separation of force locations $d$	$1.2 \times 10^{-3}$ m
Tympanum area $s$	$0.288 \times 10^{-6}$ m <sup>2</sup>
Excitation frequency $\omega$	$3.14 \times 10^4$ rad/s (5 kHz)
Sound speed $c$	344 m/s

The governing equations of the lumped model can be written as follows

$$\mathbf{M} \begin{Bmatrix} \ddot{x}_1 \\ \ddot{x}_2 \end{Bmatrix} + \mathbf{C} \begin{Bmatrix} \dot{x}_1 \\ \dot{x}_2 \end{Bmatrix} + \mathbf{K} \begin{Bmatrix} x_1 \\ x_2 \end{Bmatrix} = \begin{Bmatrix} F_1 \\ F_2 \end{Bmatrix}, \quad (2-1)$$

where

$$\mathbf{M} = \begin{bmatrix} m & \\ & m \end{bmatrix}, \quad (2-2)$$

$$\mathbf{C} = \begin{bmatrix} c_1 + c_3 & c_3 \\ c_3 & c_2 + c_3 \end{bmatrix}, \quad (2-3)$$

$$\mathbf{K} = \begin{bmatrix} k_1 + k_3 & k_3 \\ k_3 & k_2 + k_3 \end{bmatrix}. \quad (2-4)$$

For free vibrations, the natural frequencies and mode shapes of the system can be obtained as

$$\omega_1 = \sqrt{k_1 / m}, \omega_2 = \sqrt{(k_1 + 2k_3) / m}, \quad (2-5)$$

$$\mathbf{v}_1 = \begin{Bmatrix} 1 \\ -1 \end{Bmatrix}, \mathbf{v}_2 = \begin{Bmatrix} 1 \\ 1 \end{Bmatrix}. \quad (2-6)$$

The two eardrums move 180° out of phase in the first mode (rocking mode), and in phase in the second mode (bending mode). The two modes are illustrated in Figure 2-2.

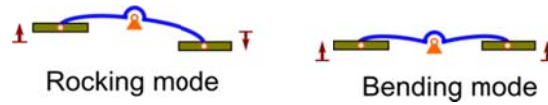


Figure 2-2: Vibration modes of the fly ear – rocking mode and bending mode.

Assuming the eardrum is much smaller than the sound wavelength, the harmonic forcing terms due to the sound pressure can be written as

$$\begin{Bmatrix} F_1 \\ F_2 \end{Bmatrix} = p_0 S \cdot e^{j\omega t} \begin{Bmatrix} e^{j\omega d \sin \theta / 2c} \\ e^{-j\omega d \sin \theta / 2c} \end{Bmatrix} = p_0 S \cdot e^{j\omega t} (p_1 \mathbf{v}_1 + p_2 \mathbf{v}_2), \quad (2-7)$$

where  $p_1$  and  $p_2$  are the modal forces that can be written as

$$p_1 = j \sin(\phi / 2), p_2 = \cos(\phi / 2), \quad (2-8)$$

and  $\phi$  is the initial phase difference at the acoustic stimulus. Note that

$$\phi = \omega d \sin \theta / c = 2\pi\chi \sin \theta, \quad (2-9)$$

where  $\chi$  is the ratio between the separation and wavelength; i.e.

$$\chi = d / \lambda. \quad (2-10)$$

By using modal analysis (Meirovitch, 2001), the modal coordinates of the response can be obtained as

$$u_1 = \frac{P_0 S}{k_1} \frac{P_1}{1 - \Omega^2 + 2j\Omega\xi_1}, u_2 = \frac{P_0 S}{k_1} \frac{P_2}{\eta^2 - \Omega^2 + 2j\eta\Omega\xi_2}, \quad (2-11)$$

where  $\Omega$  is the frequency normalized by the first natural frequency

$$\Omega = \omega / \omega_1, \quad (2-12)$$

$\eta$  is the ratio between the two natural frequency as the following

$$\eta = \omega_2 / \omega_1 = \sqrt{1 + 2k_3 / k_1}, \quad (2-13)$$

and  $\xi_1$  and  $\xi_2$  are the damping ratios defined by

$$\xi_1 = c_1 / (2\omega_1 m), \quad (2-14)$$

$$\xi_2 = (c_1 + 2c_3) / (2\omega_2 m). \quad (2-15)$$

In terms of the physical coordinates of the two DOFs, the responses can be determined to be

$$\begin{Bmatrix} x_1 \\ x_2 \end{Bmatrix} = \begin{Bmatrix} A_1 \\ A_2 \end{Bmatrix} e^{j\omega t} = \frac{p_0 s}{k_1} \cdot \frac{\cos(\phi/2)}{1 - \Omega^2 + j2\xi_1\Omega} e^{j\omega t} \begin{Bmatrix} \Gamma + j \tan(\phi/2) \\ \Gamma - j \tan(\phi/2) \end{Bmatrix}, \quad (2-16)$$

where  $\Gamma$  is the unit modal response ratio defined as

$$\Gamma = \frac{1 - \Omega^2 + j2\xi_1\Omega}{\eta^2 - \Omega^2 + j2\eta\xi_2\Omega}. \quad (2-17)$$

Note that  $\phi$  represents the phase difference of the incident sound pressure applied to the eardrums, which determines the ratio of modal forces  $p_1$  and  $p_2$  as

$$p_1 / p_2 = j \tan(\phi/2). \quad (2-18)$$

The directional cues, *mIID* and mechanical interaural phase difference (*mIPD*) can be obtained from the mechanical responses of the two eardrums as

$$mIID = 20 \log_{10} \frac{|A_1|}{|A_2|} = 20 \log_{10} \left| \frac{\Gamma + j \tan(\phi/2)}{\Gamma - j \tan(\phi/2)} \right|, \quad (2-19)$$

$$mIPD = \angle \frac{A_1}{A_2} = \angle \frac{\Gamma + j \tan(\phi/2)}{\Gamma - j \tan(\phi/2)}. \quad (2-20)$$

The range of *mIPD* is from  $-\pi$  to  $\pi$ . *mITD* can be calculated from *mIPD* by

$$mITD = \frac{mIPD}{\omega}. \quad (2-21)$$

The derivative of  $mIPD$  with respect to  $\theta$  is defined as the directional sensitivity ( $DS$ ); that is,

$$DS = \frac{\partial mIPD}{\partial \theta}. \quad (2-22)$$

To have a better understanding of how the mechanical coupling helps amplify the directional cues, the solution of the 2-DOF model is interpreted in the complex plane. In Figure 2-3, the trajectory of  $\Gamma$  is first drawn, and a point D is selected for any given frequency  $\Omega$ . When the azimuth  $\theta$  increases from  $0^\circ$  to  $90^\circ$ , point B ( $j\tan(\phi/2)$ ) and point C ( $-j\tan(\phi/2)$ ) moves along the vertical axis from the origin to the farthest point possible. Consequently,  $mIPD$  can be interpreted as the angle between vectors  $\overline{DB}$  and  $\overline{DC}$ , and  $mIID$  as the magnitude ratio of these two vectors.

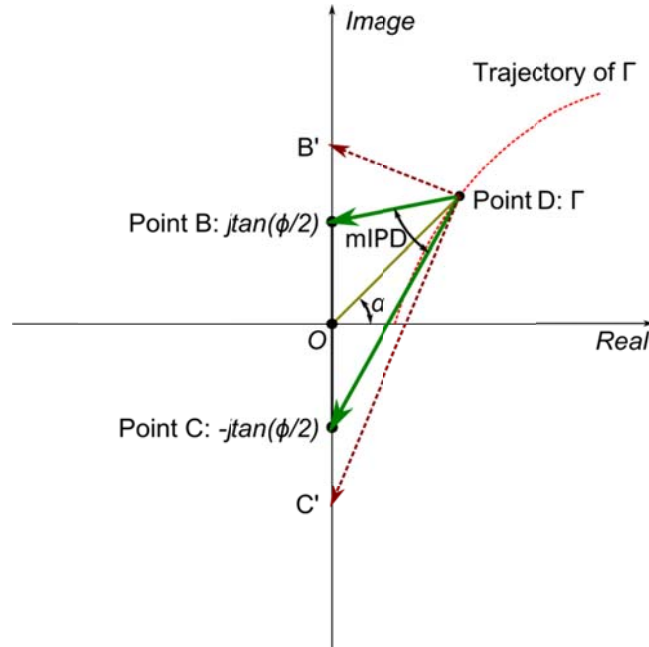


Figure 2-3: Interpretation of  $mIPD$  and  $mIID$  on a complex plane.  $\Gamma$  is the unit modal response ratio, and  $\phi$  is the initial phase difference at the acoustic stimulus.  $mIPD$  is equal to the angle between  $\overline{DB}$  and  $\overline{DC}$ , and  $mIID$  is equal to the vector length ratio  $|\overline{DC}|/|\overline{DB}|$ .

This geometric representation can help us explain how the mechanical coupling helps amplify the directional cue. First, as long as point D is not on the real axis, vectors  $\overline{DB}$  and  $\overline{DC}$  have different lengths, rendering a nonzero  $mIID$ . This also implies that in order to have significant amplification of  $mIID$ , the damping of the system cannot be close to zero. Second, to explain how the phase difference is amplified, let us assume point D is on the real axis (i.e., zero damping). In this case,  $mIPD$  and  $\phi$  have the following relationship

$$\tan \frac{mIPD}{2} = \frac{1}{\Gamma} \tan \frac{\phi}{2}. \quad (2-23)$$



To have the phase difference amplified, i.e.  $|mIPD| > |\phi|$ ,  $|\Gamma|$  has to be less than one ( $|\Gamma| < 1$ ), which requires that the excitation frequency is below a critical frequency, namely

$$\Omega < \sqrt{\frac{1+\eta^2}{2}}. \quad (2-24)$$

From this geometric representation of the directional cues, the following characteristics of the mechanically coupled 2-DOF system can be observed. As  $\theta$  increases, points B and C move further away from the origin, and thus the angle between  $\overline{DB}$  and  $\overline{DC}$  increases. In other words,  $mIPD$  increases/decreases monotonically with respect to  $\theta$ . It can also be proven that  $mIID$  achieves maximum when  $\overline{DB}$  is perpendicular to  $\overline{DC}$ . To prove this, let

$$\tau = \frac{\tan(\phi/2)}{|\Gamma|}, \alpha = \angle \Gamma. \quad (2-25)$$

Then the two directional cues  $mIID$  and  $mIPD$  can be written as

$$mIID = 20 \log_{10} \sqrt{\frac{1+\tau^2+2\tau \sin \alpha}{1+\tau^2-2\tau \sin \alpha}} = 20 \log_{10} \sqrt{1 + \frac{4 \sin \alpha}{\tau + \frac{1}{\tau} - 2 \sin \alpha}}, \quad (2-26)$$

$$mIPD = \cos^{-1} \frac{1-\tau^2}{\sqrt{(1-\tau^2)^2 + 4\tau^2 \cos^2 \alpha}}. \quad (2-27)$$

It can be readily verified that when  $\tau = 1$ ,  $mIPD$  is equal to  $90^\circ$ , and  $|mIID|$  reaches the maximum; that is,

$$\max |mIID| = \left| 10 \log_{10} \frac{1 + \sin \alpha}{1 - \sin \alpha} \right|. \quad (2-28)$$

If  $mIID$  needs to be a monotonic function of  $\theta$ ,  $mIPD$  cannot exceed  $90^\circ$ . This implies that there is a tradeoff between the two directional cues.

## 2.2 Parametric studies

In this section, the analytical solutions obtained in the previous section will be used to investigate the effects of key parameters in the lumped model on the characteristics of directional cues. For sound source localization, the relative relationship between the two ears is more important than the transfer function of each individual ear, although they are closely related. As such, three parameters are identified in Equation (2-19), namely the stiffness ratio  $k_3/k_1$  (which determines the natural frequency ratio  $\omega_2/\omega_1$ ), damping ratios  $\xi_1$  and  $\xi_2$ , and separation-to-wavelength ratio  $\chi = d/\lambda$ . All these parameters affect the relative contributions from the rocking and bending modes.

### 2.2.1 Stiffness ratio

The coupling strength is determined by the stiffness ratio  $k_3/k_1$ , which is related to the natural frequency ratio  $\eta = \omega_2/\omega_1$  by  $\eta^2 = 1 + 2k_3/k_1$ . As the coupling becomes stiffer ( $\eta$  becomes larger), the contribution from the rocking mode is more dominant than that from the bending mode. In Figure 2-4, the frequency spectra and spatial distributions of  $mIPD$  are compared for three coupling scenarios:  $\eta = 2$ ,  $\eta = 4.36$ , and  $\eta = 10$ . Since the  $mIPD$  is  $180^\circ$  at the rocking mode frequency and  $0^\circ$  at the bending mode frequency, a stiffer coupling usually renders a higher phase difference. Another phenomenon observed from

Figure 2-4(b)-(c) is that  $mIPD$  as a function of frequency may experience a sign change (from  $180^\circ$  to  $-180^\circ$  or vice versa) around the rocking mode natural frequency for a stiffer coupling.

However, when designing a directional microphone with mechanically coupled diaphragms, the amplification of  $mIPD$  or the absolute value of  $mIPD$  should not be the sole objective. If the contribution from the bending mode is negligible,  $mIPD$  is always  $\pm 180^\circ$  regardless of the incident azimuth. In this case,  $mIPD$  cannot be used as an indicator to differentiate azimuth angles of the sound source.

A more important parameter for sound source localization is the change of  $mIPD$  with respect to azimuth perturbation, which is defined as the directional sensitivity ( $DS$ ). As shown in Figure 2-5(d)-(f), increasing the coupling strength will generally help increase  $DS$  near the midline (i.e.,  $\theta = 0$ ). However, if the coupling is too stiff, the increase of  $DS$  will only happen in the range near the midline, and at large azimuth angles near  $\pm 90^\circ$ , the  $DS$  is significantly reduced. Another disadvantage of stiff coupling is that the rapid change of  $DS$  will cause a strongly nonlinear relationship between  $mIPD$  and  $\theta$ .

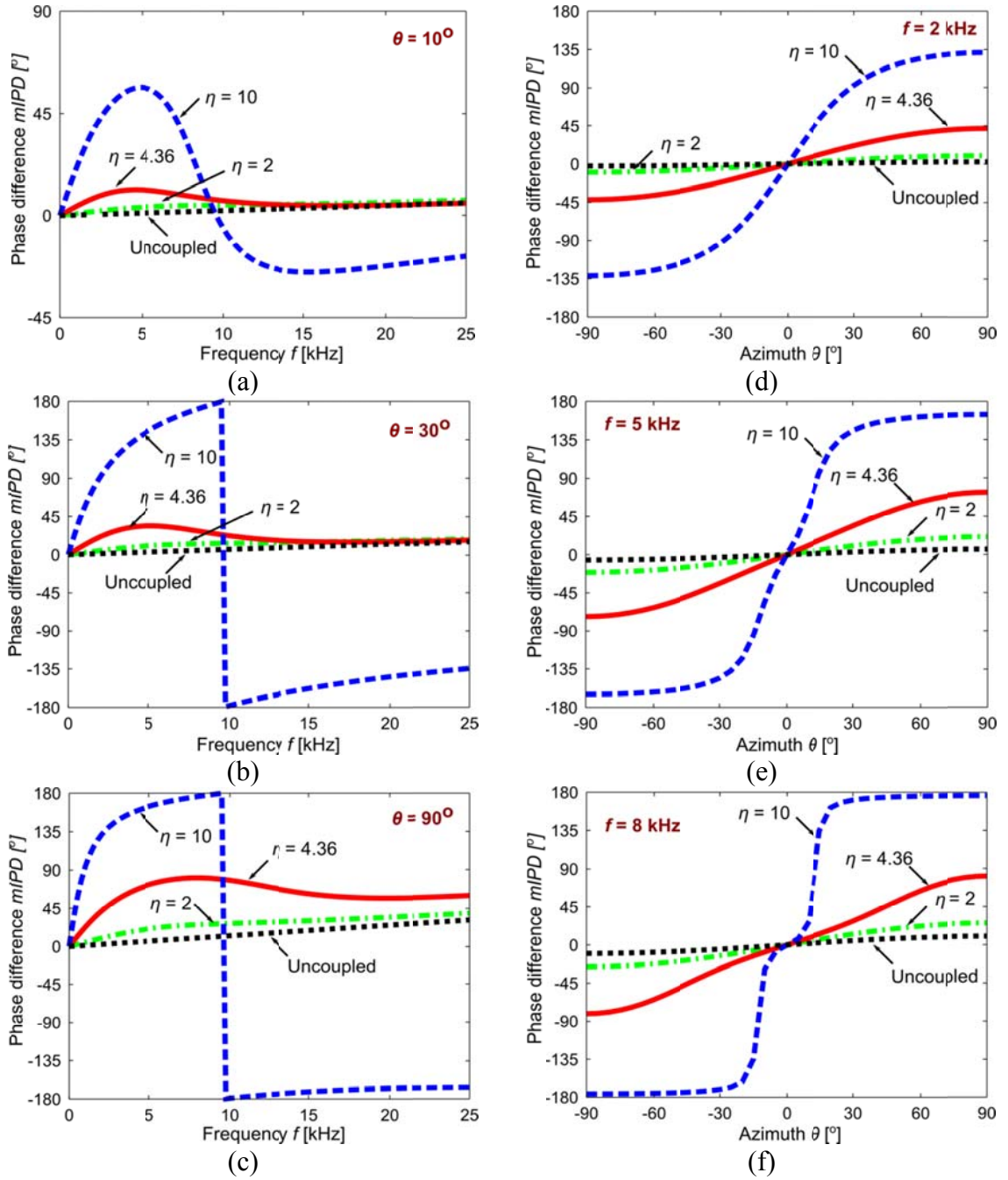


Figure 2-4: Effects of the stiffness ratio  $k_3/k_1$  on the phase difference  $mIPD$ . All the parameters used in the simulations are the fly ear's structural parameters listed in Table 2-1, with  $k_3$  modified for three scenarios  $\eta = 2$ ,  $\eta = 4.36$  (fly ear's case), and  $\eta = 10$ .  $k_3/k_1$  is related to the natural frequency ratio  $k_3/k_1 = (\eta^2 - 1)/2$ . (a)-(c): Spectra of  $mIPD$  for azimuths of  $10^\circ$ ,  $30^\circ$ , and  $90^\circ$ . (d)-(f): Spatial distributions of  $mIPD$  for frequencies of 2 kHz, 5 kHz, and 8 kHz.

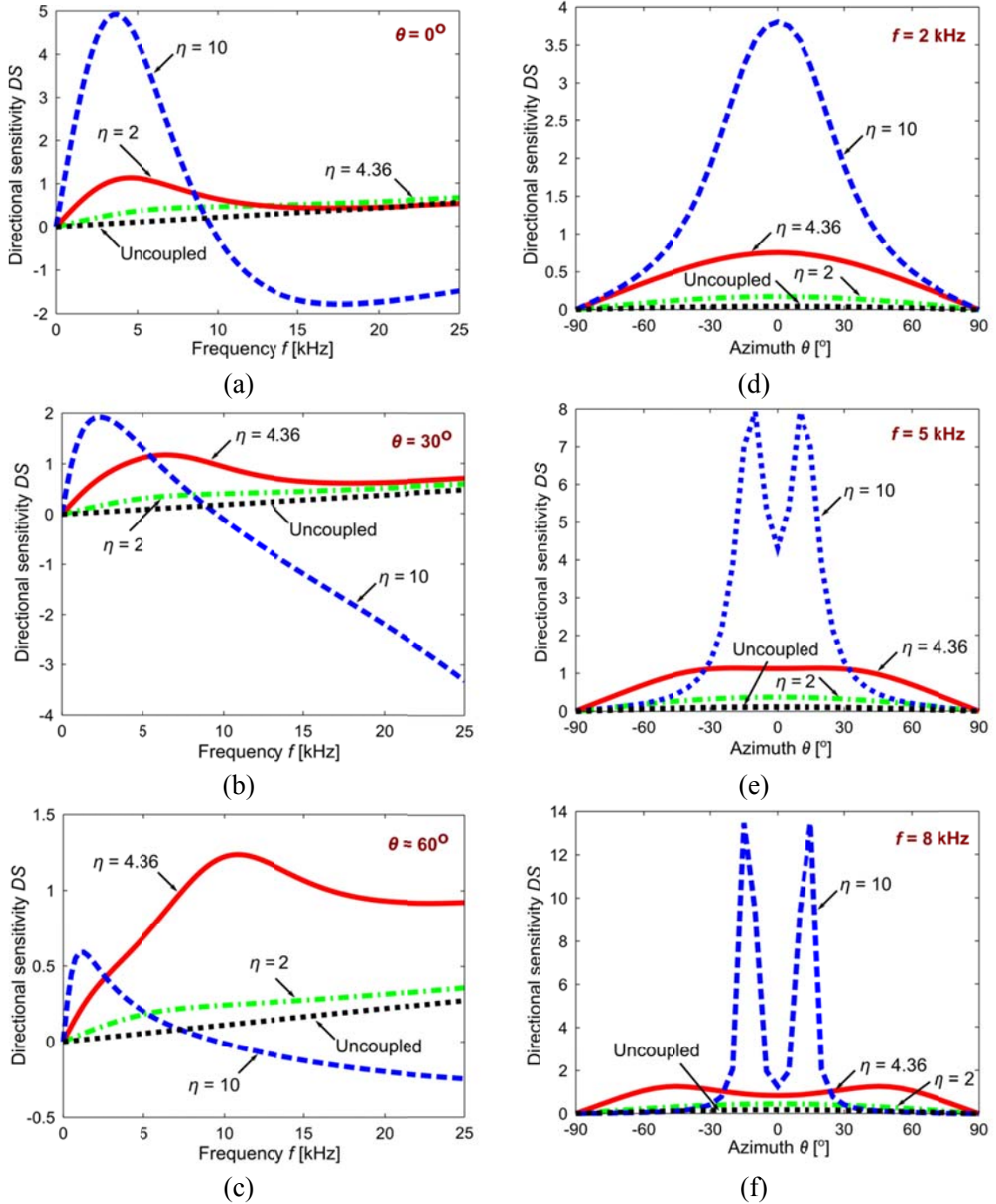


Figure 2-5: Effects of the stiffness ratio  $k_3/k_1$  on directional sensitivity  $DS$ . All the parameters used in the simulations are the fly ear's structural parameters listed in Table 2-1, with  $k_3$  modified for three scenarios  $\eta = 2$ ,  $\eta = 4.36$  (fly ear's case), and  $\eta = 10$ .  $k_3/k_1$  is related to the natural frequency ratio  $k_3/k_1 = (\eta^2 - 1)/2$ . (a)-(c): Spectra of  $DS$  for azimuths of  $10^\circ$ ,  $30^\circ$ , and  $90^\circ$ . (d)-(f): Spatial distributions of  $DS$  for frequencies of 2 kHz, 5 kHz, and 8 kHz.

### 2.2.2 Damping

In Figure 2-6 and Figure 2-7, *mIPD* and *DS* for three damping scenarios are obtained and compared, which are the following: i)  $\xi_1 = 0.10$  and  $\xi_2 = 0.14$ , ii)  $\xi_1 = 0.50$  and  $\xi_2 = 0.69$ , and iii)  $\xi_1 = 0.89$  and  $\xi_2 = 1.23$  (fly ear's case). As the damping decreases, the phase difference is generally more amplified, as shown in Figure 2-6(a)-(c). For a small damping, *mIPD* as a function of frequency experiences a sign change near the rocking mode. The effects of damping on *mIPD* are more pronounced in the frequency range near the rocking mode. For example, as shown in Figure 2-6(d)-(e) and Figure 2-7(d)-(e), the change of *mIPD* is much less for 2 kHz than the change for 8 kHz (rocking mode natural frequency is 7.12 kHz). It can be explained by the fact that damping has much less effects on the transfer function of either diaphragm for frequencies much less than the rocking mode natural frequency.

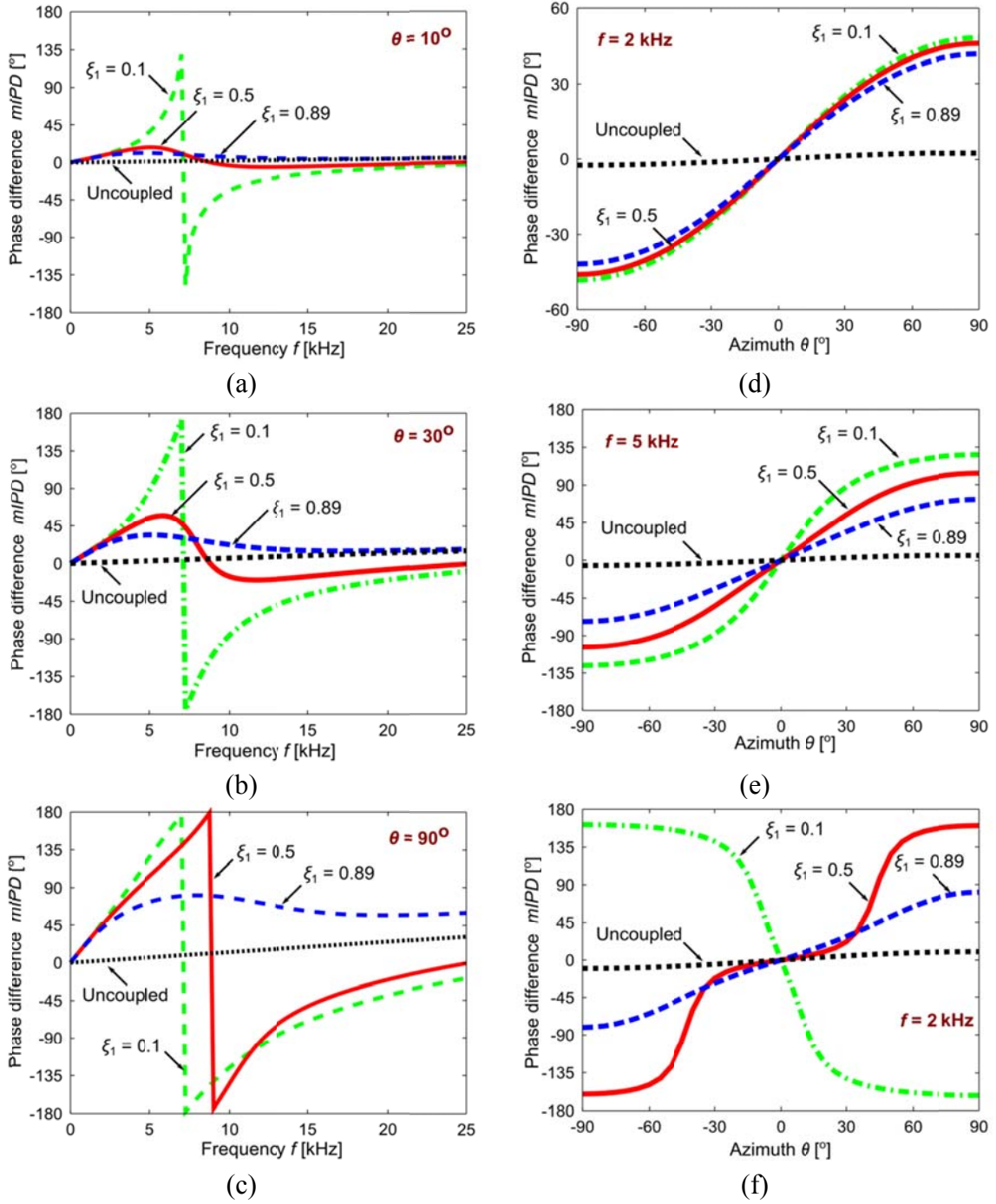


Figure 2-6: Effects of the damping ratios on the phase difference  $mIPD$ . All the parameters used in the simulations are the fly ear's structural parameters listed in Table 2-1, with the two damping ratios  $\zeta_1$  and  $\zeta_2$  modified for three scenarios,  $\zeta_1 = 0.10$  and  $\zeta_2 = 0.14$ ,  $\zeta_1 = 0.50$  and  $\zeta_2 = 0.69$ , and  $\zeta_1 = 0.89$  and  $\zeta_2 = 1.23$  (fly ear's case). (a)-(c): Spectrums of  $mIPD$  for azimuth  $10^\circ$ ,  $30^\circ$ , and  $90^\circ$ . (d)-(f): Spatial distributions of  $mIPD$  for frequencies 2 kHz, 5 kHz, and 8 kHz.

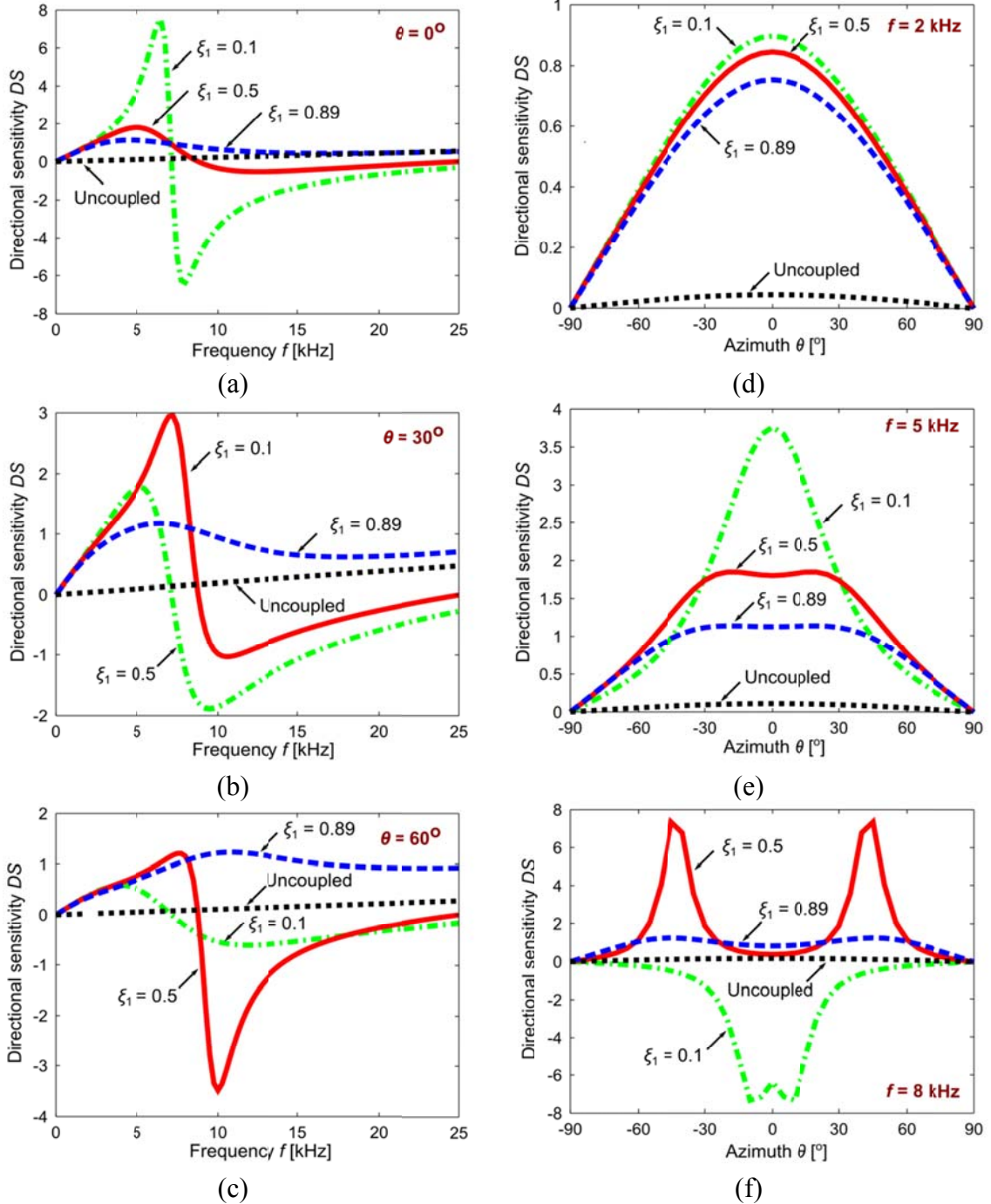


Figure 2-7: Effects of the damping ratios on the directional sensitivity  $DS$ . All the parameters used in the simulations are the fly ear's structural parameters listed in Table 2-1, with the two damping ratios  $\zeta_1$  and  $\zeta_2$  modified for three scenarios:  $\zeta_1 = 0.10$  and  $\zeta_2 = 0.14$ ,  $\zeta_1 = 0.50$  and  $\zeta_2 = 0.69$ , and  $\zeta_1 = 0.89$  and  $\zeta_2 = 1.23$  (fly ear's case). (a)-(c): Spectra of  $DS$  for azimuths  $10^\circ$ ,  $30^\circ$ , and  $90^\circ$ . (d)-(f): Spatial distribution of  $DS$  for frequencies 2 kHz, 5 kHz, and 8 kHz.



### 2.2.3 Separation-to-wavelength ratio

As can be seen from the analytical solution of the lumped model (Equation (2-20)),  $mIPD$  and  $DS$  are determined by two parameters, the modal response ratio  $\Gamma$  and the modal force ratio  $j\tan(\phi/2)$ . The former relates to the coupled system's design parameters, including the previously discussed stiffness ratio and damping ratio; the latter relates to the separation-to-wavelength ratio  $\chi = d/\lambda$ .

In Figure 2-8 and Figure 2-9,  $mIPD$  and  $DS$  are obtained for three different diaphragm separations:  $d = 0.4$  mm,  $d = 1.2$  mm, and  $d = 3.6$  mm. Overall, increasing the separation will increase the contribution from the rocking mode, rendering a higher  $mIPD$  and  $DS$ . However, if the separation is too big, it has a similar effect as a stiff bridge; that is,  $mIPD$  saturates easily as the sound source moves away from the midline. Other disadvantages for big separations include the increased size and the disturbance to the sound field due to the increased size.

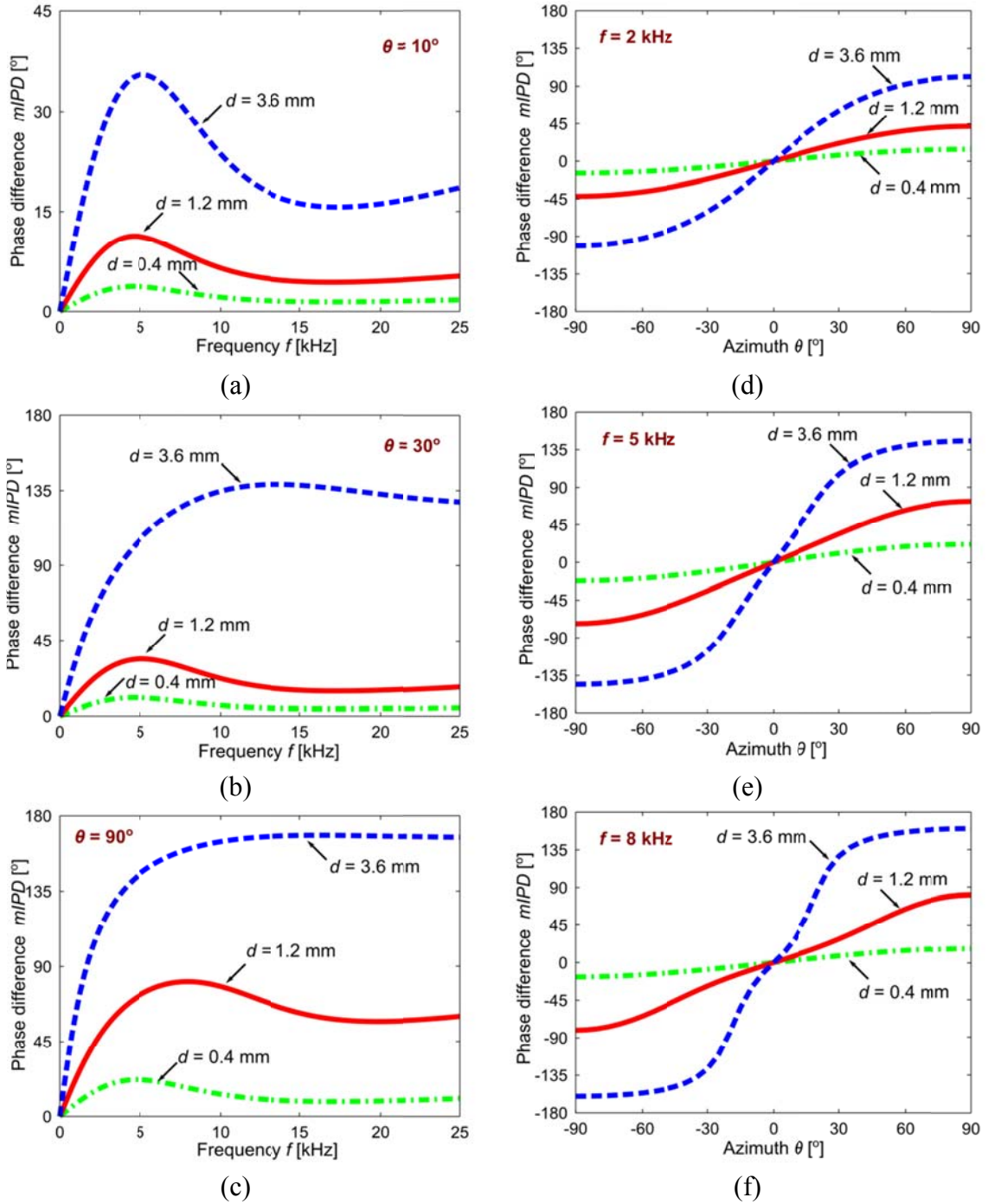


Figure 2-8: Effects of the interaural separation  $d$  on the phase difference  $mIPD$ . All the parameters used in the simulations are the fly ear's structural parameters listed in Table 2-1, with  $d$  modified for three scenarios,  $d = 0.4$  mm,  $d = 1.2$  mm (fly ear's case), and  $d = 3.6$  mm. (a)-(c): Spectra of  $mIPD$  for azimuths of  $10^\circ$ ,  $30^\circ$ , and  $90^\circ$ . (d)-(f): Spatial distributions of  $mIPD$  for frequencies of 2 kHz, 5 kHz, and 8 kHz.

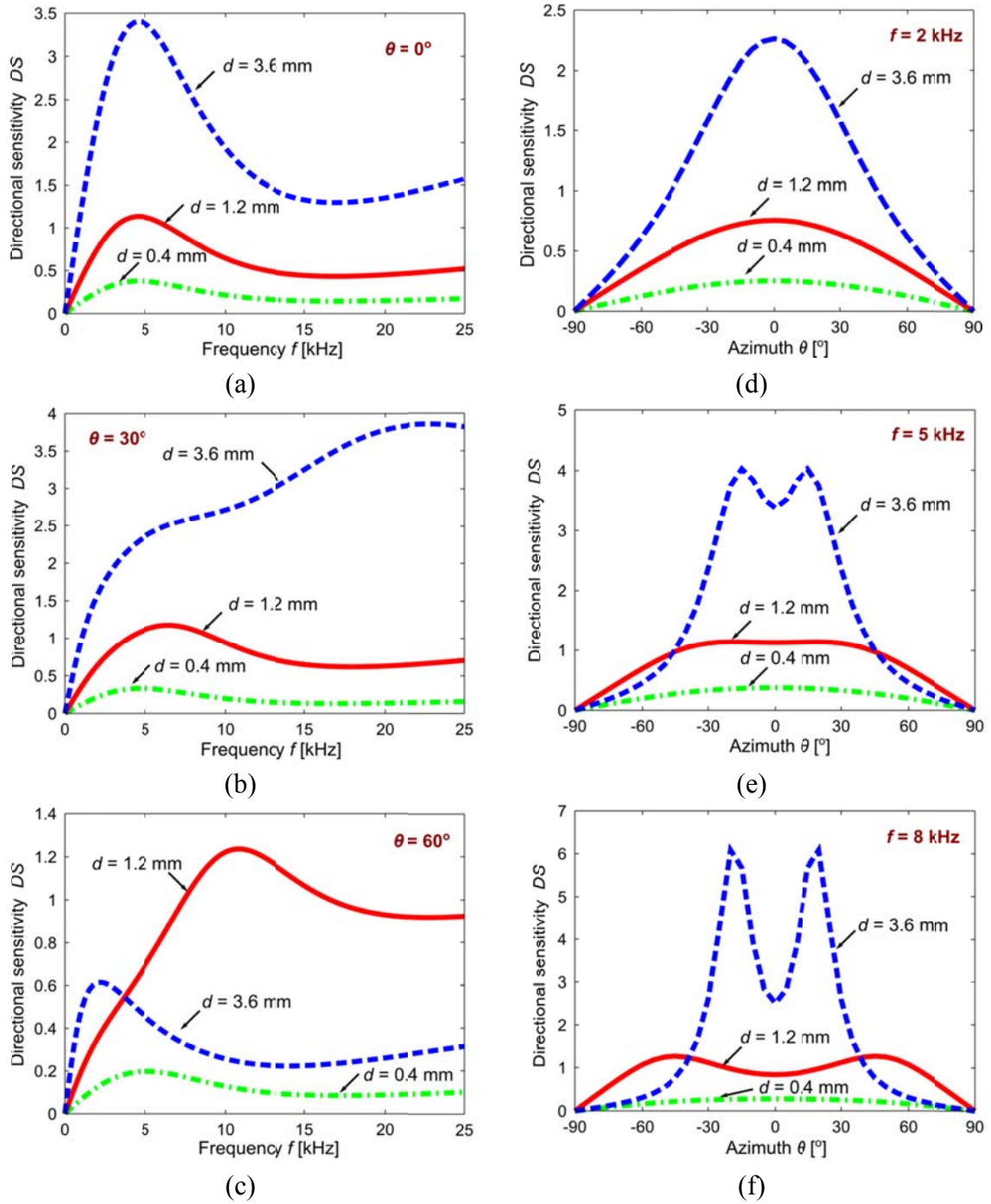


Figure 2-9: Effects of the interaural separation  $d$  on the directional sensitivity  $DS$ . All the parameters used in the simulations are the fly ear's structural parameters listed in Table 2-1, with  $d$  modified for three scenarios,  $d = 0.4$  mm,  $d = 1.2$  mm (fly ear's case), and  $d = 3.6$  mm. (a)-(c): Spectra of  $DS$  for azimuth  $10^\circ$ ,  $30^\circ$ , and  $90^\circ$ . (d)-(f): Spatial distributions of  $DS$  for frequencies 2 kHz, 5 kHz, and 8 kHz.

### 2.3 Dual-optimality in the fly ear

With the analytical solutions of the directional cues and directional sensitivity that were obtained previously, here, an answer is sought for the following question: is the fly ear a nature designed optimal structure that is tailored to localize the cricket's 5 kHz calling song?  $mIPD$  is chosen as the directional cue for further investigation due to the following considerations. First, equivalent to  $mITD$ ,  $mIPD$  is a normalized measure that is independent of the sound wavelength and sound speed. Second,  $mIPD/mITD$  is usually more reliable and accurate for sound source localization than intensity based measurement (Harris & Sergeant, 1971). Third,  $mIPD/mITD$  is widely used in sound source localization using microphone arrays, which means the results to be obtained here will be consistent with existing algorithms and have a much broader impact. Lastly, based on the analytical solutions,  $mIPD/mITD$  is a monotonic function of azimuth in all scenarios whereas this one-to-one correspondence is not guaranteed for  $mIID$ .

From the perspective of sensor design, the ideal relationship between the  $mIPD$  and the azimuth  $\theta$  for sound source localization is a straight line with a maximal slope, as the ideal line shown in Figure 2-10. Because  $mIPD$  is confined between  $-180^\circ$  and  $180^\circ$  as  $\theta$  varies from  $-90^\circ$  to  $90^\circ$ , the maximal slope is  $\pm 2$ . However, as the relationship between  $mIPD$  and  $\theta$  is determined by the governing equations for the mechanically coupled system,  $mIPD$  cannot be an arbitrary function of  $\theta$ . For example, the slope at the two extreme positions ( $\theta = \pm 90^\circ$ ) is equal to zero regardless of the structural parameters, which implies that  $mIPD(\theta)$  cannot be a straight line. As such, appropriate design objectives need to be sought that are constrained by the governing equations.

Next, the effects of mechanical coupling on *mIPD* are investigated. The fly ear parameters listed in Table 2-1 are used to calculate *mIPD* at 5 kHz for various coupling scenarios by changing the stiffness of the coupling bridge  $k_3$ . Note that the natural frequency ratio  $\eta$  is related to the stiffness ratio  $k_3/k_1$  by  $\eta^2 = 1+2k_3/k_1$ . First, for the size of the fly ear (i.e., the separation between eardrum centers is 1.2 mm), the phase difference at the acoustic inputs (i.e, *IPD*) is equal to  $6.3^\circ \times \sin(\theta)$ , which is the phase difference obtained for the uncoupled case ( $\eta = 1$ ) in Figure 2-10. If the coupling is soft ( $\eta = 2$ ), *mIPD* is amplified to  $20.9^\circ$  at an azimuth of  $90^\circ$ , which is far less than  $180^\circ$ . On the other hand, if the coupling is stiff ( $\eta = 20$ ), although *mIPD* is amplified to  $176.8^\circ$  at  $90^\circ$  azimuth, it cannot be differentiated for most of the azimuth range. As can be clearly seen from Figure 2-10, for the stiff coupling case, *mIPD* increases very rapidly to  $\sim \pm 180^\circ$  when  $\theta$  is slightly off  $0^\circ$ . The fly ear ( $\eta = 4.36$ ) represents a case between the soft coupling and the stiff coupling, in which a proper contribution from both rocking and bending modes is utilized.

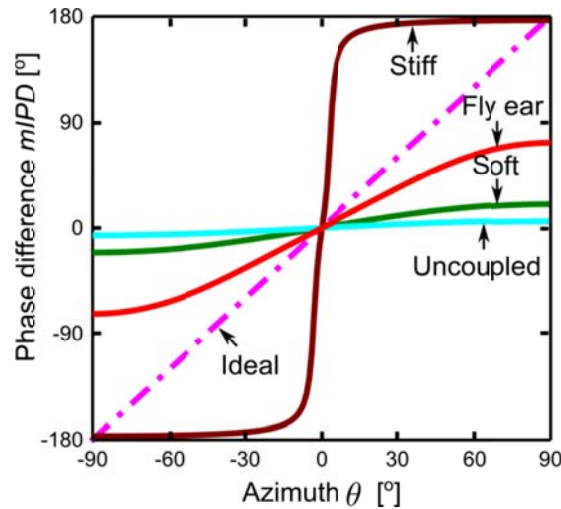


Figure 2-10: Phase difference  $mIPD$  at 5 kHz as a function of azimuth for different coupling strength scenarios: stiff (natural frequency ratio  $\eta = 20$ ), fly ear ( $\eta = 4.36$ ), soft ( $\eta = 2$ ), and uncoupled ( $\eta = 1$ ). The results are obtained by using the fly ear’s structural parameters with varying bridge stiffness  $k_3$ .

Note that the localization performance does not rely on the absolute value of  $mIPD$ . Rather, the variation of  $mIPD$  with respect to  $\theta$  (i.e.,  $DS$ ) is the key to determine the localization performance. The simulation results shown in Figure 2-11 can be used to confirm the previous observation: the mechanical coupling needs to be “medium” in order to render sufficient amplification of the phase difference without compromising the ability of differentiating azimuths.

Another important finding from Figure 2-11 is that the  $DS$  for the fly ear is flat in the azimuth range of  $-30^\circ$  to  $30^\circ$ . This is consistent with the localization/lateralization scheme that was observed in the experiments about the fly’s localization of its host crickets (Mason et al., 2001). Recall that as shown in Figure 1-7, the fly is able to estimate the true azimuth location when the source is in the range of  $-30^\circ$  to  $30^\circ$ . When the source is out of this range, the fly can only make a left or right turn decision.

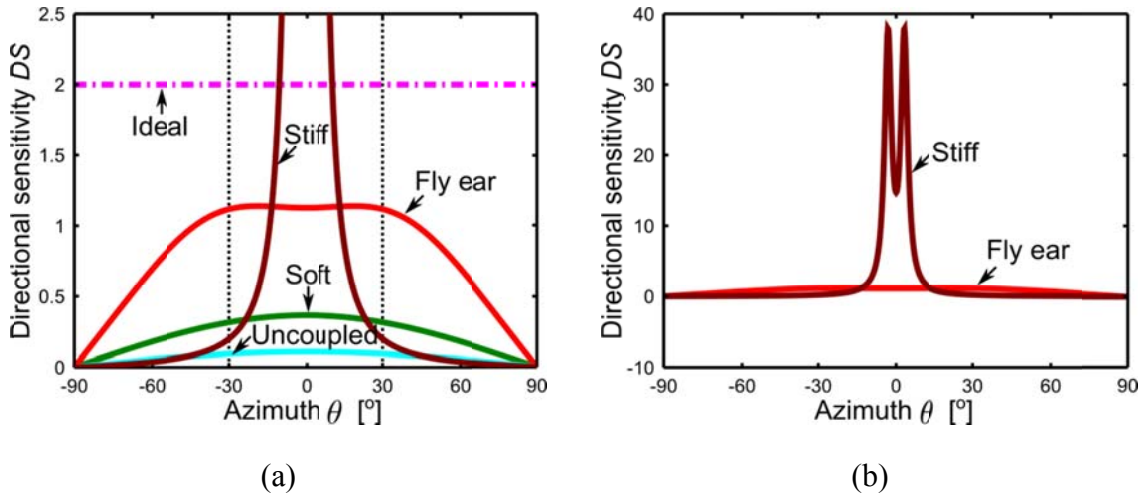


Figure 2-11: Directional sensitivity  $DS$  at 5 kHz as a function of azimuth for different coupling strength scenarios: stiff (natural frequency ratio  $\eta = 20$ ), fly ear ( $\eta = 4.36$ ), soft ( $\eta = 2$ ), and uncoupled ( $\eta = 1$ ). The results are obtained by using the fly ear's structural parameters with varying bridge stiffness  $k_3$ . (a) and (b) are shown in different scales for clarity.

When  $DS$  as a function of azimuth angle is plotted at different sound frequencies, as shown in Figure 2-12(a), it is found that at 5 kHz, the calling song frequency of the fly's host cricket, the fly ear can not only achieve a constant  $DS$  for azimuth angles between  $-30^\circ$  to  $30^\circ$ , but can also obtain a higher  $DS$  than those obtained at other frequencies (e.g., 2 kHz and 8 kHz). To further investigate this result, two performance metrics, the average  $DS$  ( $ADS$ ) and the nonlinearity ( $NL$ ) of  $mIPD$  over the azimuth range of  $-30^\circ$  to  $30^\circ$  are defined as follows.

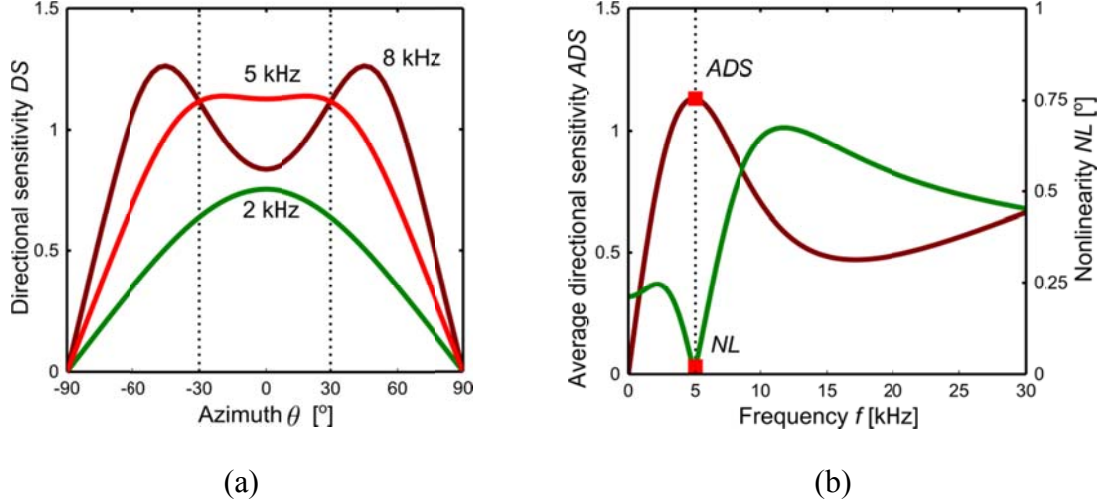


Figure 2-12: Dual-optimality of the fly-ear and fly-ear inspired sensor. (a)  $DS$  at three different frequencies. (b) Spectra of average directional sensitivity ( $ADS$ ) and nonlinearity ( $NL$ ).

In the vicinity of midline (i.e.,  $-\Theta \leq \theta \leq \Theta$  ( $\Theta = 30^\circ$ )),  $mIPD(\theta)$  can be approximated by a linear function of  $\theta$  based on linear least squares; that is,

$$\widehat{mIPD}(\theta) = mIPD_0 + ADS \cdot \theta. \quad (2-29)$$

The error of this linear approximation is used as a measure of nonlinearity ( $NL$ ), which takes the form of

$$NL = \frac{1}{|ADS|} \sqrt{\frac{1}{2\Theta} \int_{-\Theta}^{\Theta} [mIPD(\theta) - \widehat{mIPD}(\theta)]^2 d\theta}. \quad (2-30)$$

$NL$  has a unit of degrees and it is normalized by the absolute value of  $ADS$ . It should be noted that this normalization has two important implications. One is to make  $NL$  independent of the scaling of  $mIPD$  so that  $NL$  only depends on the overall shape of  $mIPD$ ; the other is the physical meaning of  $NL$ , as the normalized nonlinearity indicates the average error of azimuth estimation using the linear approximation.



When these two metrics of the fly ear are plotted in the frequency domain, an interesting result can be observed: the minimum  $NL$  and the maximum  $ADS$  are achieved simultaneously at 5 kHz, as shown in Figure 2-12(b). This result suggests that the fly ear is endowed with a dual optimality characteristic at its working frequency.

As discussed previously, it should be stressed that the fly ear does not work like a rigid seesaw; that is, a structure with a purely rocking mode. Rather, it utilizes a proper combination of both rocking mode and bending mode. To further illustrate the characteristics of such a rigid system, the maps of  $mIPD$  and the absolute  $DS$  in the space of azimuth and frequency are shown in Figure 2-13. Since the rocking mode dominates the bending mode for the structure with a rigid coupling, the phase difference increases quickly to  $\pm 180^\circ$  and saturates when the incident azimuth deviates slightly from the midline ( $\theta = 0^\circ$ ), as shown in Figure 2-13(a). As a result, such a rigid system cannot perform well when using  $mIPD$  or  $mITD$  is used as the directional cue due to the small directional sensitivity shown in Figure 2-13(b). Theoretically, it can only work in a very confined spatial range in the close vicinity of midline. It should also be noted that the detection system may not be able to differentiate the azimuths of  $180^\circ$  and  $-180^\circ$  due to issues of noise and asynchronous data acquisition. In other words, the seesaw system may not even make a correct left/right estimation based on  $mIPD/mITD$  readings.

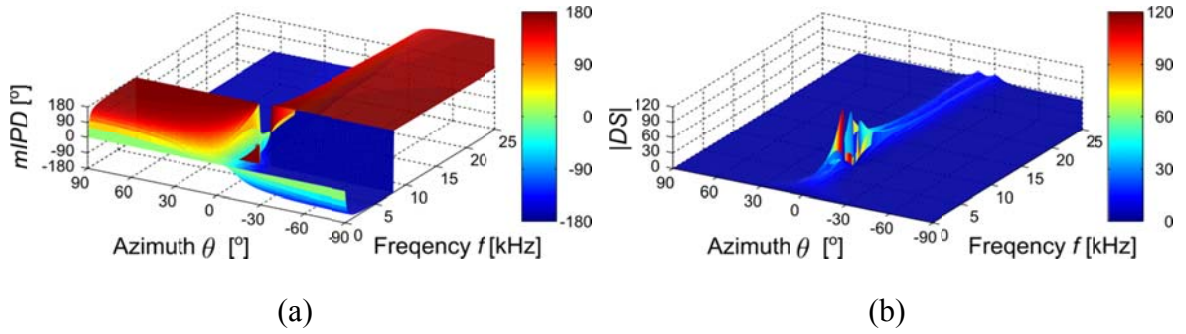


Figure 2-13: Contour of (a)  $mIPD$  and (b)  $DS$  in the space of azimuth and frequency for the rigid system in Figure 2-11.

## 2.4 Mimicking the fly ear's dual-optimality

Here, further investigation is carried out to find out whether a synthetic device endowed with the fly ear's dual optimality characteristic can be developed. An optimization problem is formulated to seek solutions in the entire design space which will meet the objective of achieving dual optimality (i.e., minimal  $NL$  and maximal  $ADS$ ) over the azimuth of  $-30^\circ$  to  $30^\circ$  at the same sound frequency (i.e., the optimal working frequency). For simplicity, the problem is constrained in one dimension (azimuth). Note that there are several key parameters, the natural frequency ratio  $\eta$ , the separation-to-wavelength ratio  $\chi$ , and the damping ratios that can influence the  $NL$  and  $ADS$ .

In Figure 2-14(a), the rocking and bending mode natural frequencies that ensure the dual optimality characteristic are plotted as a function of separation-to-wavelength ratio  $\chi$ , given the fly ear's damping scenario (i.e.,  $\xi_1 = 0.89$ ,  $\xi_2 = 1.23$ ). Based on the fly-ear's geometry and its working frequency of 5 kHz, following the two curves in Figure 2-14(a), the natural frequencies required to achieve the dual optimality can be obtained (rocking mode: 6.99 kHz, bending mode: 30.1 kHz); these predictions are in excellent agreement

with the experimental data reported in the literature (7.12 kHz and 31.0 kHz) (Miles et al., 1995). This finding confirms that the fly ear represents a nature-designed optimal structure that can simultaneously achieve the maximum  $DS$  and the minimum  $NL$  at its working frequency of 5 kHz. Similar design curves can be obtained for different damping scenarios, e.g.  $\xi_1 = 0.09$ ,  $\xi_2 = 0.12$  as shown in Figure 2-14(b).

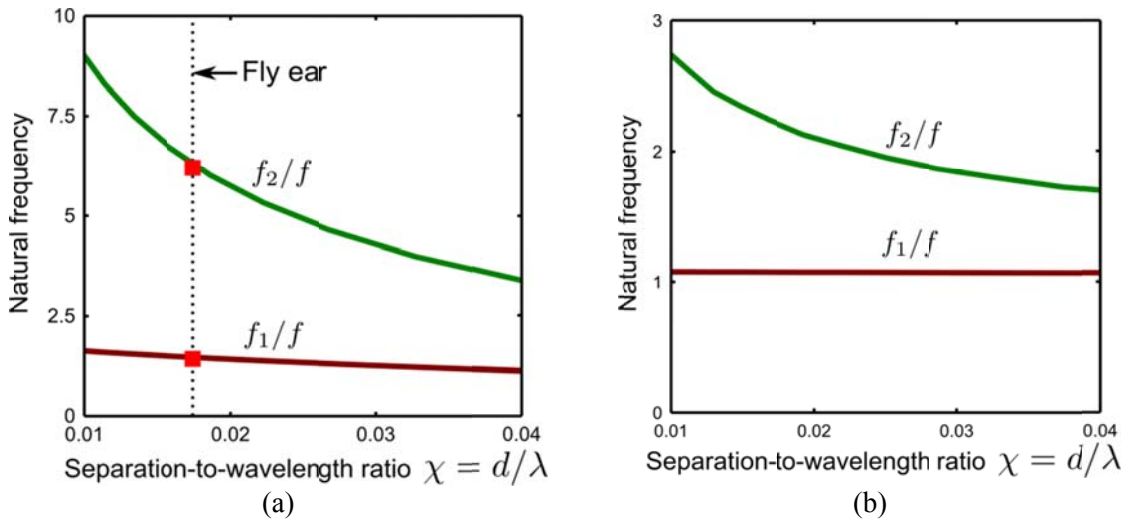


Figure 2-14: Natural frequencies (normalized by the optimal working frequency) obtained in optimization analysis to ensure dual-optimality characteristic as a function of the wavelength-to-separation ratio  $\chi$ . (a) High damping case ( $\xi_1 = 0.89$ ,  $\xi_2 = 1.23$ ). (b) Low damping case ( $\xi_1 = 0.09$ ,  $\xi_2 = 0.12$ ).

Clearly, based on Figure 2-14, the fly-ear structure is not the only optimal structure that has the dual optimality characteristic at its designated working frequency. For any given separation-to-wavelength ratio  $\chi$ , the required natural frequencies for achieving the dual optimality characteristic can be obtained. Note that the dual optimality is only obtained here for  $\chi$  in the range of 1:100 to 1:25. For  $\chi$  larger than  $\sim 1:25$ , while the maximum  $ADS$  and the minimum  $NL$  may not be achieved at the same frequency, conventional directional microphone without mechanical coupling usually suffice for the localization

task; at the other end of the spectrum, although an optimal structure can be found, the amplified phase difference may still be too low for accurate sound localization. Therefore, the results in Figure 2-14 provide a framework that enables one to create synthetic devices that mimic the fly ear's dual optimality characteristic, which can be tailored to work at any frequency and/or with a desirable size.

For example, given the same interaural separation as the fly ear (1.2 mm), one can design fly-ear inspired structures that are tailored to work at the optimal frequencies of 2 kHz and 8 kHz, for which  $\chi$  is calculated as 0.0070 and 0.0279, respectively. According to the design curves in Figure 2-14(a), the two natural frequencies to achieve dual-optimality are 3.41 kHz and 22.31 kHz for the device with the working frequency of 2 kHz, and 10.29 kHz and 36.03 kHz for the 8 kHz working frequency. The spectra of *ADS* and *NL* in Figure 2-15(a) indicate that the designed systems possess the dual-optimality characteristic of the fly ear. For the three optimal systems in Figure 2-15(a), the resulting *DS* at the corresponding optimal frequencies have similar flat plateaus in the linear region of  $-30^\circ \leq \theta \leq 30^\circ$ , as shown in Figure 2-15(b).

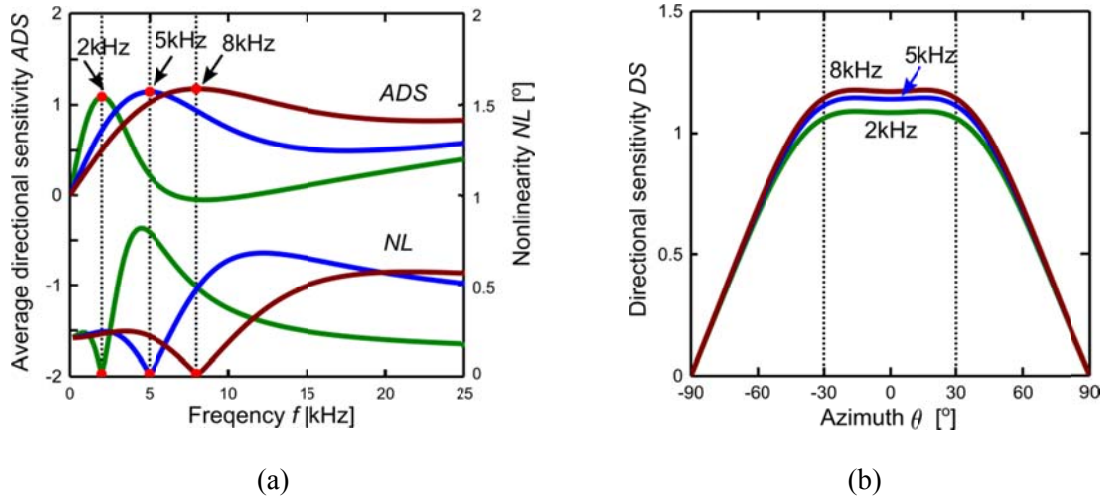
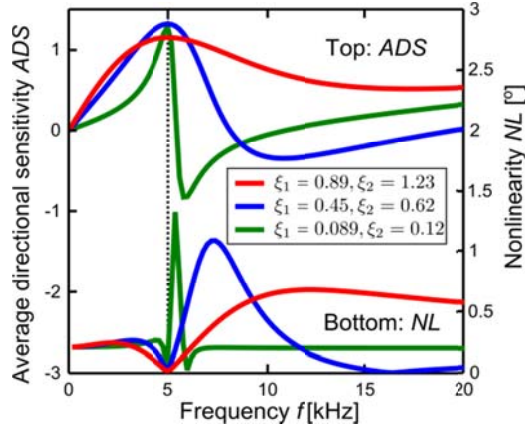
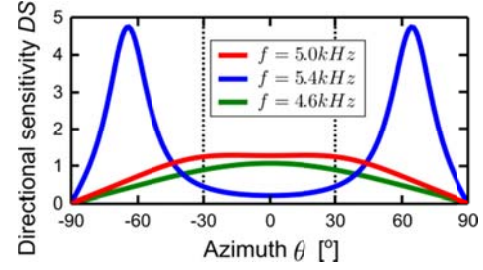


Figure 2-15: Dual optimality of three designs, which have the same damping and center-to-center separation as the fly ear, to work at 2 kHz, 5 kHz, and 8 kHz, respectively. (a) Average directional sensitivity (*ADS*) and nonlinearity (*NL*) in the frequency domain. (b) Directional sensitivity in the spatial domain at the corresponding optimal working frequencies.

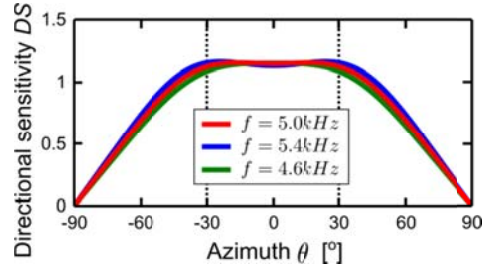
Further, the dual-optimality characteristic is not limited to the damping scenario of the fly ear. For a center-to-center separation of 1.2 mm and working frequency of 5 kHz, three systems, as shown in Figure 2-16(a), are designed to achieve dual-optimality for different damping scenarios. As the damping decreases, the peak of *ADS* spectrum and the dip of *NL* spectrum become sharper. As a result, when the working frequency is slightly off the optimal working frequency, the characteristics of the low damping system will change drastically, as shown in Figure 2-16(b). On the other hand, the system with a high damping is more robust to the variation of sound source frequency (Figure 2-16(c)), which is important for the fly *Ormia* as the calling song of its host crickets varies in the frequency range of 4.6 to 5 kHz (Robert et al., 1998).



(a)



(b)



(c)

Figure 2-16: Three design examples with different damping scenarios, given the same center-to-center separation (1.2mm) and working frequency of 5 kHz as the fly ear. (a) *ADS* and *NL* in the frequency domain. (b) Variation of *DS* at frequencies slightly off the optimal frequency for the low damping system ( $\xi_1 = 0.09$ ,  $\xi_2 = 0.12$ ). (c) Variation of *DS* at frequencies slightly off the optimal frequency for the high damping system ( $\xi_1 = 0.89$ ,  $\xi_2 = 1.23$ ).

## 2.5 Summary

The superacute directional hearing of the parasitic fly *Ormia ochracea* has been attributed to the mechanical coupling between its eardrums. The results obtained in this dissertation provide a new insight into the fly ear's directional hearing abilities. By defining the two performance metrics, *ADS* and *NL*, the fly ear is shown to possess a unique characteristic of dual optimality, which may indicate that the structural parameters of the fly ear are optimized for its localization ability at the specific frequency of 5 kHz, the calling song frequency of its host crickets.

The dual optimality characteristic can provide a basis for understanding the fly's superior directional hearing capability as well as its unique localization-lateralization scheme. First, although the absolute value of the *mIPD* is maximal at the two extreme positions ( $\theta = \pm 90^\circ$ ), the corresponding *DS* is close to zero at these positions and the maximal *DS* is actually achieved in the vicinity of the midline. Therefore, the fly naturally turns the head front (midline of the ear) towards the source so that the maximum *DS* (i.e., maximal slope) can be achieved to ensure the best localization precision. This is similar to a related finding reported for an Egyptian fruit bat, which uses not the maximal sonar beam intensity but its maximal slope for target localization (Yovel, Falk, Moss, & Ulanovsky, 2010). Second, *mIPD* is a linear function of azimuth in the range from  $-30^\circ$  to  $30^\circ$ , which is coincident with the sigmoid relationship of fly's turning speed with respect to the azimuth, obtained in the phonotactic experiments with the fly (Mason et al., 2001). Given the limited neural processing ability, a constant and maximal *DS* can certainly help the fly perform the localization task more accurately and more efficiently for the azimuths from  $-30^\circ$  to  $30^\circ$ . Therefore, in this sense, it is not only the mechanical coupling mechanism that helps the fly ear obtain significantly amplified directional cues, but more importantly, the structural parameters of the fly ear have been tailored to achieve the dual optimality characteristic at 5 kHz, facilitating a unique localization-lateralization scheme for accurately pinpointing its host.

To achieve the dual-optimality characteristic, this dissertation work also shows that the structural parameters need to be tuned to have a proper contribution from both the rocking mode and the bending mode. As an example, the stiffness of the coupling bridge

cannot be too soft or too stiff, otherwise the directional cue *mIPD* is not sufficiently amplified or it is overly amplified so that the directional sensitivity is greatly reduced.

Furthermore, this dissertation work provides a framework to design a fly-ear inspired acoustic sensor that can mimic not only the mechanical coupling mechanism but more importantly the dual-optimality characteristic. For any desired working frequency and/or interaural separation, the natural frequencies of the two vibration modes of the mechanically coupled system can be obtained according to the optimal design curves shown in Figure 2-14. To design a fly-ear inspired sensor, the structural parameters of the sensor can be obtained through analytical or numerical modeling. It is also demonstrated in this chapter that different systems can be designed for different damping scenarios. In general, a high damping results in a much smoother peak in the *ADS* spectrum, which is beneficial to accommodating the variation of structural parameters or sound stimulus frequencies. On the other hand, although a low damping system with a much sharper *ADS* peak is less robust to stimulus frequency variations, a low damping level renders a higher amplification ratio, a much higher *ADS*, and better frequency selectivity, which can be advantageous in certain applications.



## **Chapter 3 Fly-Ear Inspired Directional Microphones: Design and Model Development**

### **3.1 Fly-ear inspired directional microphone design**

Based on the framework developed in the previous chapter, bio-inspired directional microphone that consists of two circular diaphragms coupled by a medially supported bridge is designed, as shown in Figure 3-1. The two diaphragms are clamped on its periphery boundary to a substrate. The two ends of the bridge are connected to the diaphragm centers. To detect the sound induced vibrations of the diaphragms, a Fabry-Perot interferometer is formed between each diaphragm and an optical fiber tip, which is part of a low coherence fiber optic interferometric detection system. The details of the detection system will be provided in the next Chapter along with the development of the directional microphones.

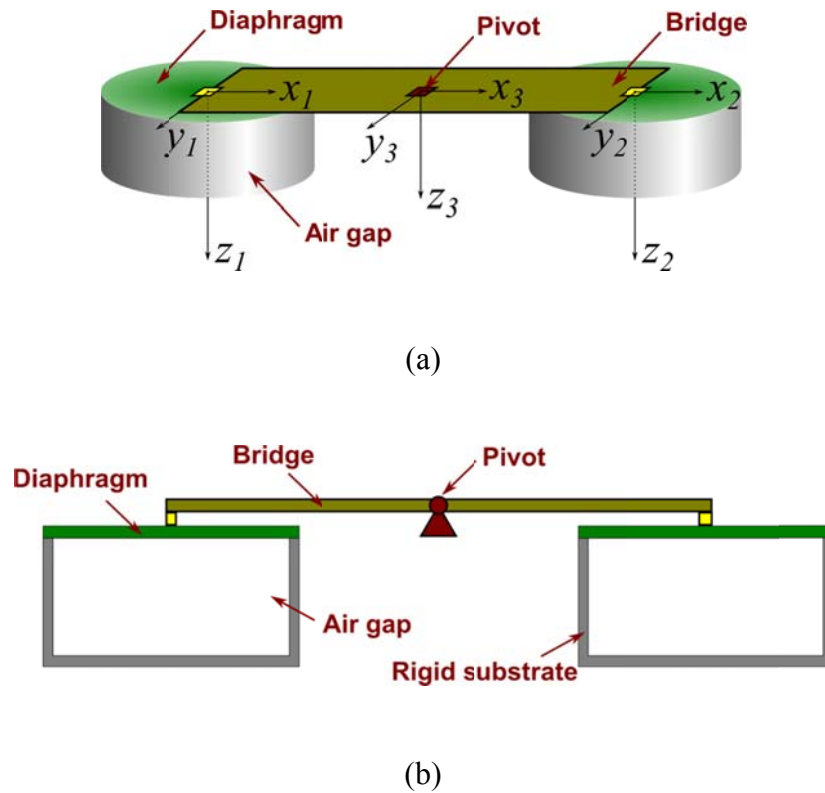


Figure 3-1: A fly-ear inspired directional microphone. (a) Schematic. (b) Cross-section view.

### 3.2 Overview of model development

In the hearing organ of the fly *Ormia ochracea*, there is an undivided air space backing the two eardrums, as shown in Figure 3-2(a). Theoretically, the coupling between the eardrums can be through the cuticular intertympanal bridge (stiffness  $K_3$ ), or the air space (stiffness  $K'_3$ ). The latter represents a pressure difference receiver mechanism, as introduced in Chapter 1. To study the relative contributions of both mechanisms, one experiment was designed to stimulate one eardrum mechanically with a vibrating pin, and the responses before and after opening the air space were compared, as illustrated in Figure 3-2(b) (Robert et al., 1998). It is concluded that the coupling is solely due to the

intertympanal mechanical coupling, and the amplitude of the eardrums is not greatly affected by surgically opening the air space.

In comparison to the fly's hearing organ configuration, the proposed design of the fly-ear inspired directional microphone shown in Figure 3-1 has several unique features. First, the two air gaps backing each diaphragm are not interconnected, which completely excludes the possibility of pressure difference receiver mechanism. Second, both air gaps are closed by the diaphragm and rigid walls. This ensures that the sound wave cannot propagate to the back surface of the diaphragm, as in the case of conventional pressure gradient microphones. Third, the diaphragms are connected to the bridge at the diaphragm centers. In this way, the coupling force applied to the diaphragm does not excite the un-axisymmetric modes of the diaphragms, and the diaphragm has maximal deflection at its center. These features will ensure that the coupling is solely through the center pivoted bridge and the coupling force is well transmitted.

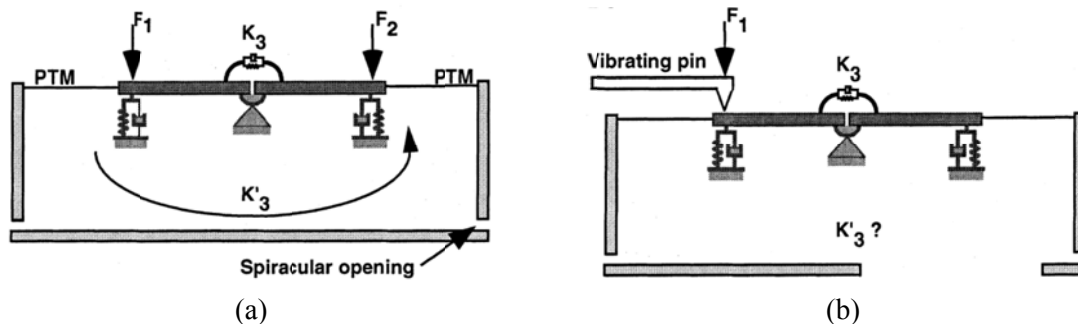


Figure 3-2: Mechanical analog of the fly's hearing organ. (a) The two prosternal tympanal membranes (PTM) are connected by a cuticular intertympanal bridge ( $K_3$ ).  $K_3'$  is the stiffness due to the air space of the tracheal sac. (b) A mechanical stimulation is applied to one end of the bridge by a vibrating pin. One side of the air space is opened to study the relative contribution of  $K_3$  and  $K_3'$ . (Robert et al., 1998)

Although the air gap does not contribute directly to the mechanical coupling between the diaphragms, it does affect the diaphragm's response to external stimulus, including the acoustic sound wave and the mechanical force through the coupling bridge. Therefore, a novel continuum mechanics model needs to be developed that features two coupling modules, one for the mechanical coupling of the two diaphragms through the bridge and the other for each diaphragm coupled with the backing air gaps. This model can be used to achieve a fundamental understanding of the structural dynamics of the fly-ear inspired directional microphone described in the previous section and guide the development of this microphone.

The continuum mechanics model will include three individual components: the diaphragm, the bridge, and the air gap. The diaphragm will be modeled as a thin plate with in-plane tension, which can account for any scenario between a pure plate and a pure membrane (M. Yu & Balachandran, 2005). The bridge will be modeled as an Euler-Bernoulli beam that is pinned in the middle. The air gap will be described by a sound wave equation. The models for each individual component will be described in Section 3.3. In Section 3.4, the coupling module between a single diaphragm and an air gap will be detailed by assuming a no-slip boundary condition at the interface. In Section 3.5, the coupling module through the bridge will be described by assuming a geometric compatibility condition at the joints. Furthermore, the developed model will be compared with a finite element model in ANSYS and the 2-DOF model in Section 3.6, followed by parametric studies in Section 3.7.

### 3.3 Models of individual components of the sensor structure

#### 3.3.1 Diaphragm

A cylindrical coordinate system is established at the diaphragm center, as shown in Figure 3-3. The radial coordinate  $r$  is normalized so that  $0 \leq r \leq 1$ . The clamped circular diaphragm is modeled as a plate with in-plane tension. Depending on a normalized tension parameter, the diaphragm can have a pure plate behavior with zero tension, or a pure membrane behavior with a high tensile stress (M. Yu & Balachandran, 2005). This generalized model is particularly useful for microelectromechanical system (MEMS ) pressure sensors where residual thermal stress cannot be completely relieved from the fabrication process. For the clamped circular plate with in-plane tension, the transverse displacement of the plate  $w_p(r, \theta, t)$  is described by the thin plate theory

$$\rho_p h_p \frac{\partial^2 w_p}{\partial t^2} + \mu \frac{\partial w_p}{\partial t} + \frac{D}{a^4} \nabla^4 w_p - \frac{N_0}{a^2} \nabla^2 w_p = f_p(r, \theta, t) , \quad (3-1)$$

where  $\rho_p$ ,  $h_p$ ,  $\mu$ ,  $D$ ,  $a$ ,  $N_0$ ,  $f_p$  are respectively the density, thickness, damping coefficient, flexural rigidity, radius, in-plane force, and external pressure. Subscript  $p$  denotes the plate.  $D$  is related to the Young's modulus  $E_p$  and Poisson's ratio  $\nu$  by

$$D = \frac{E_p h_p^3}{12(1-\nu^2)} . \quad (3-2)$$

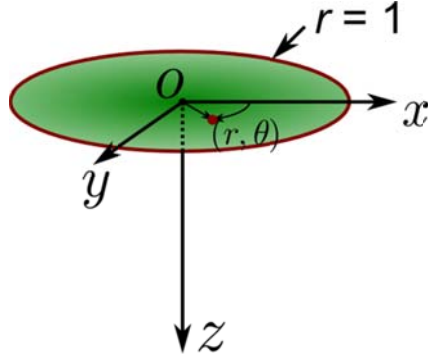


Figure 3-3: Coordinate system for the circular clamped diaphragm.

Because the plate is clamped on its circular edge, the following boundary conditions can be obtained:

$$\begin{cases} w_p(r, \theta, t)|_{r=1} = 0 \\ \frac{\partial w_p(r, \theta, t)}{\partial r}|_{r=1} = 0 \end{cases} \quad (3-3)$$

The mode shapes of free vibration  $U_{p,mn}(r) \cdot \Theta_m(\theta)$  of the diaphragm can be obtained as ( $m$  and  $n$  denotes the mode orders in the azimuthal and radial directions)

$$\Theta_m(\theta) = \begin{cases} 1/\sqrt{2\pi} & m = 0 \\ \cos(m\theta + \phi_m)/\sqrt{\pi} & m = 1, 2, 3 \dots \end{cases}, \quad (3-4)$$

$$U_{p,mn}(r) = A_{mn} [I_m(\alpha_{1mn})J_m(\alpha_{2mn}r) - J_m(\alpha_{2mn})I_m(\alpha_{1mn}r)] \quad n = 1, 2, \dots, \quad (3-5)$$

where  $\phi_m$  is the constant phase determined by initial conditions,  $\alpha_{1mn}$  and  $\alpha_{2mn}$  are solved from the characteristic equations

$$\alpha_1^2 = \alpha_2^2 + \chi_{ip}, \quad (3-6)$$

$$\alpha_2 I_m(\alpha_1) J_m'(\alpha_2) - \alpha_1 J_m(\alpha_2) I_m'(\alpha_1) = 0, \quad (3-7)$$

$\chi_{tp} = N_0 a^2 / D$  is the normalized surface tension parameter,  $J_m$  and  $J_m'$  are Bessel function of first kind and its first derivative, and  $I_m$  and  $I_m'$  are modified Bessel function of first kind and its first derivative.  $A_{mn}$  is the coefficient used to normalize the mode shapes to ensure the orthogonality of the mode shapes; that is

$$\int_{r=0}^1 U_{p,mn}(r) U_{p,mk}(r) r dr = \delta_{nk}, \quad \int_{r=0}^1 \Theta_m(r) \Theta_n(r) dr = \delta_{mn}, \quad (3-8)$$

where  $\delta_{mn}$  is the kronecker delta.

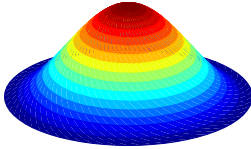
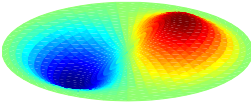
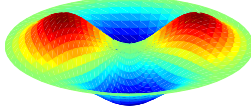
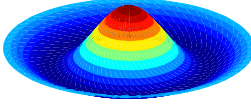
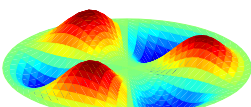
The natural frequencies can be calculated from  $\alpha_{1mn}$  and  $\alpha_{2mn}$  by

$$\omega_{mn} = \frac{c_p}{a} \frac{h_p}{a} \Lambda_{mn}, \quad (3-9)$$

where  $\Lambda_{mn} = \alpha_{1mn} \alpha_{2mn} / \sqrt{12}$ , and  $c_p = \sqrt{E_p / \rho_p (1 - \nu^2)}$  is the speed of longitudinal wave.

The first five modes and their natural frequencies of a circular clamped plate without in-plane tension are shown in Table 3-1.

Table 3-1: Natural frequency and mode shapes of circular clamped plate without in-plane tension

Order ( $m,n$ )	Natural frequency $\Lambda_{mn}$	Mode shape
(0,1)	2.9490	
(1,1)	6.1373	
(2,1)	10.0681	
(0,2)	11.4809	
(3,1)	14.7311	

The transfer function relating the modal coordinates of the pressure and transverse displacement response ( $F_{p,mn}$  and  $W_{p,mn}$ ) is obtained as follows

$$\frac{W_{p,mn}}{a} = H_{p,mn} \frac{F_{p,mn}}{E_p}, \quad (3-10)$$

where

$$H_{p,mn} = (1-\nu^2) \left( \frac{a}{h_p} \right)^3 \frac{1}{\Lambda_{mn}^2 - \Omega_p^2 + \tilde{\mu} j \Omega_p}, \quad (3-11)$$



$\tilde{\mu} = \mu(1-\nu^2)(a/h_p)^2 / \sqrt{E_p \rho_p}$ , and  $\Omega_p = \omega a^2 / (c_p h_p)$  is the normalized frequency.

### 3.3.2 Air gap

The air gap is modeled as a cylindrical air chamber with a flexible top (the diaphragm). A cylindrical coordinate system is established at the center of the top surface, as shown in Figure 3-4. The coordinates are normalized so that  $z = 0$  at the top, and  $z = 1$  at the bottom. The air gap can be described by the wave equation in terms of velocity potential  $\Psi(r, \theta, z, t)$  as

$$\frac{1}{a^2} \left( \frac{\partial^2 \Psi}{\partial r^2} + \frac{1}{r} \frac{\partial \Psi}{\partial r} + \frac{1}{r^2} \frac{\partial^2 \Psi}{\partial \theta^2} \right) + \frac{1}{g^2} \frac{\partial^2 \Psi}{\partial z^2} = \frac{1}{c_0^2} \frac{\partial^2 \Psi}{\partial t^2}, \quad (3-12)$$

where  $c_0$  and  $g$  are the sound speed and air gap height, respectively.  $c_0$  is related to the static pressure  $p_0$  of the air gap and density  $\rho_0$  by  $c_0 = \sqrt{\gamma p_0 / \rho_0}$ , where  $\gamma$  is the adiabatic index. A no-slip boundary condition is assumed at the interface between the plate and the air; i.e.

$$\left. \frac{1}{g} \frac{\partial \Psi}{\partial z} \right|_{z=0} = \frac{\partial w}{\partial t}. \quad (3-13)$$

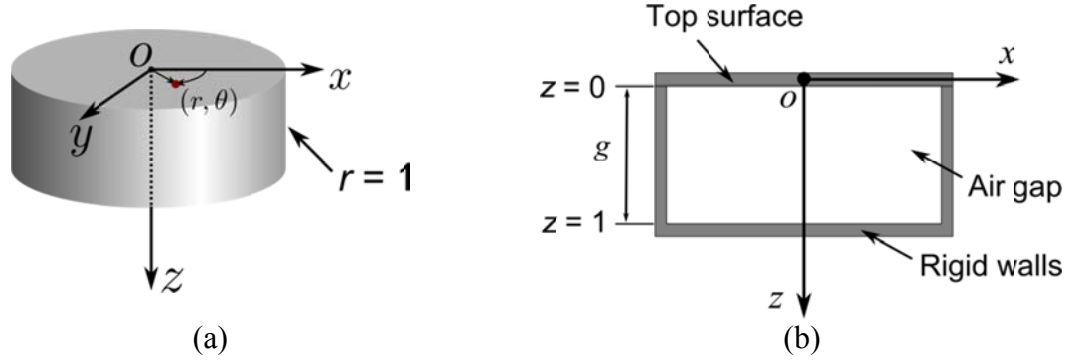


Figure 3-4: Cylindrical air gap with rigid walls and a top surface. (a) Coordinate system. (b) Cross-section view.

Through separation of variables, the solution to a harmonic excitation at the top surface can be assumed as

$$\Psi(r, \theta, z, t) = U_a(r) \Theta(\theta) Z(z) e^{j\omega t} . \quad (3-14)$$

Here, the subscript  $a$  denotes the air gap. The radial part of the mode shape function can be obtained as (the azimuthal part  $\Theta_m(\theta)$  is same as that in Equation (3-4) for the plate)

$$U_{a,mn}(r) = B_{mn} J_m(\beta_{mn} r) \quad n = 1, 2, \dots , \quad (3-15)$$

where  $\beta_{mn}$  is solved from the characteristic equation

$$J_m'(\beta) = 0 . \quad (3-16)$$

$m$  and  $n$  denote the mode order number in the azimuthal and radial directions.  $B_{mn}$  is the coefficient used to normalize the mode shapes to ensure the following orthogonal property

$$\int_{r=0}^1 U_{a,mn}(r) U_{a,mk}(r) r dr = \delta_{nk}, \int_{r=0}^1 \Theta_m(r) \Theta_n(r) dr = \delta_{mn} . \quad (3-17)$$

Note that for the axisymmetric mode when  $m = 0$ , Equation (3-16) has a zero root (labeled as  $\beta_{00} = 0$ ), which corresponds to the commonly known air spring mode.

In the case of a close-ended air gap (the top surface is also rigid), the natural frequencies are obtained as

$$\omega_{mnl} = \frac{c_0}{a} \sqrt{\beta_{mn}^2 + \pi^2 l^2 (a/g)^2} \quad l = 0, 1, 2, \dots \quad (3-18)$$

In order to establish a relationship between the displacement excitation of the flexible top  $w_a(r, \theta, t)$ , the velocity potential solution to the wave equation  $\Psi(r, \theta, z, t)$ , and the reaction pressure at the interface  $p_r(r, \theta, t) = p(r, \theta, z=0, t)$ , they are decomposed to the following forms

$$w_a(r, \theta, t) = \sum_{m,n} W_{a,mn} U_{a,mn}(r) \Theta_m(\theta) e^{j\omega t}, \quad (3-19)$$

$$\Psi(r, \theta, z, t) = \sum_{m,n} \Psi_{mn} U_{a,mn}(r) \Theta_m(\theta) Z_{mn}(\omega, z) e^{j\omega t}, \quad (3-20)$$

$$p_r(r, \theta, t) = \sum_{m,n} P_{r,mn} U_{a,mn}(r) \Theta_m(\theta) e^{j\omega t}, \quad (3-21)$$

where  $W_{a,mn}$ ,  $\Psi_{mn}$ , and  $P_{r,mn}$  are the modal coefficients, and  $Z_{mn}(\omega, z)$  is the z-component of the velocity potential solution that is dependent on the excitation frequency. Substitute (3-19) and (3-20) into the no-slip boundary condition and use the orthogonality in (3-17) to obtain

$$\left( j\omega W_{a,mn} - \Psi_{mn} \frac{1}{g} \frac{\partial Z_{mn}}{\partial z} \right) \Big|_{z=0} = 0. \quad (3-22)$$

The reaction pressure is related to the velocity potential by

$$p_r(r, \theta, t) = (-\rho_a \partial \Psi / \partial t) \Big|_{z=0}, \quad (3-23)$$

where  $\rho_a$  is the air density. Then, the transfer function between the modal coordinates of the displacement excitation and the reaction pressure can be obtained as follows

$$\frac{P_{r,mn}}{p_0} = H_{a,mn} \frac{W_{a,mn}}{a}, \quad (3-24)$$

where

$$H_{a,mn}(\Omega_a) = -\gamma \frac{g}{a} \Omega_a^2 \frac{\coth(\zeta)}{\zeta}, \quad (3-25)$$

$$\zeta = \frac{g}{a} \sqrt{\beta_{mn}^2 - \Omega_a^2}, \quad (3-26)$$

and  $\Omega_a = \omega a / c_0$  is the normalized frequency.

### 3.3.3 Bridge

The bridge is modeled as an Euler-Bernoulli beam with an axial load. A coordinate system is established at the center. The range of the normalized axial coordinate is  $-1 \leq x \leq 1$ . The governing equation in terms of the transverse displacement  $w_b(x,t)$  is given by (subscript  $b$  denotes the beam/bridge)

$$\rho_b h_b b \frac{\partial^2 w_b}{\partial t^2} + \mu_b \frac{\partial w_b}{\partial t} + \frac{P_b}{L^2} \frac{\partial^2 w_b}{\partial x^2} + \frac{E_b I_b}{L^4} \frac{\partial^4 w_b}{\partial x^4} = f_b, \quad (3-27)$$

where  $h_b$ ,  $b$ ,  $2L$  are the beam's thickness, width, and length, respectively,  $\rho_b$ ,  $E_b$ ,  $I_b$  are the beam's density, Young's modulus, and area moment of inertia, respectively, and  $\mu_b$ ,  $P_b$ , and  $f_b$  are the damping coefficient, axial load, and external distributed force, respectively. The boundary conditions are zero bending moment and zero shearing force on both ends ( $x = \pm 1$ ), zero displacement and continuity of moment at the center point ( $x = 0$ ); i.e.

$$\left\{ \begin{array}{l} w_b \Big|_{x=0^+, 0^-} = 0 \\ \frac{\partial w_b}{\partial x} \Big|_{x=0^+} = \frac{\partial w_b}{\partial x} \Big|_{x=0^-} \\ \frac{\partial^2 w_b}{\partial x^2} \Big|_{x=0^+} = \frac{\partial^2 w_b}{\partial x^2} \Big|_{x=0^-} \\ \frac{\partial^2 w_b}{\partial x^2} \Big|_{x=\pm 1} = 0 \\ \frac{\partial^3 w_b}{\partial x^3} \Big|_{x=\pm 1} = 0 \end{array} \right. \quad (3-28)$$

### Free vibration

The center-pinned beam has three kinds of mode shapes. The first kind of mode is a rigid rotational mode

$$U_{b,0} = \sqrt{3/2}x, \quad (3-29)$$

for which the natural frequency is

$$\omega_{b,0} = 0. \quad (3-30)$$

The second kind of mode is non-rigid and symmetric. The mode shapes functions are described by

$$U_{b,i}(x) = G_i \left[ \begin{array}{l} \eta_{t,i}^2 \eta_{h,i}^2 (\eta_{t,i} \cos \eta_{t,i} \sinh \eta_{h,i} - \eta_{h,i} \sin \eta_{t,i} \cosh \eta_{h,i}) (\cos \eta_{t,i} x - \cosh \eta_{h,i} x) \\ + (\eta_{h,i}^5 + \eta_{h,i}^2 \eta_{t,i}^3 \sin \eta_{t,i} \sinh \eta_{h,i} + \eta_{h,i}^3 \eta_{t,i}^2 \cos \eta_{t,i} \cosh \eta_{h,i}) |\sin \eta_{t,i} x| \\ + (\eta_{t,i}^5 - \eta_{h,i}^3 \eta_{t,i}^2 \sin \eta_{t,i} \sinh \eta_{h,i} + \eta_{h,i}^2 \eta_{t,i}^3 \cos \eta_{t,i} \cosh \eta_{h,i}) |\sinh \eta_{h,i} x| \end{array} \right]. \quad (3-31)$$

$\eta_h$  and  $\eta_t$  are solved from the characteristic equations

$$\eta_h^4 + \eta_t^4 + \eta_h \eta_t (\eta_t^2 - \eta_h^2) \sin \eta_t \sinh \eta_h + 2\eta_h^2 \eta_t^2 \cos \eta_t \cosh \eta_h = 0, \quad (3-32)$$

$$\eta_t^2 - \eta_h^2 = 2\chi_{tb}, \quad (3-33)$$

where  $\chi_{tb}$  is the normalized axial load parameter

$$\chi_{tb} = \frac{PL_b^2}{2E_b I_b}. \quad (3-34)$$

The third kind of modes is non-rigid and anti-symmetric, for which the mode shapes are described by

$$U_{b,i}(x) = G_i (\eta_{h,i}^2 \sinh \eta_{h,i} \sin \eta_t x + \eta_{t,i}^2 \sin \eta_{t,i} \sinh \eta_{h,i} x). \quad (3-35)$$

$\eta_h$  and  $\eta_t$  are solved from (3-33) and

$$\eta_t \cos \eta_t \sinh \eta_h - \eta_h \sin \eta_t \cosh \eta_h = 0. \quad (3-36)$$

The natural frequency is calculated by

$$\omega_{b,i} = \frac{c_b}{L} \frac{h_b}{L} \Xi_i, \quad (3-37)$$

where

$$\Xi_i = \frac{\eta_{h,i} \eta_{t,i}}{\sqrt{12}}, \quad (3-38)$$

and  $c_b$  is the longitudinal wave speed in the beam

$$c_b = \sqrt{\frac{E_b}{\rho_b}}. \quad (3-39)$$

The coefficients in the mode shapes function are chosen to ensure the orthogonal property

$$\int_{-1}^1 U_{b,i}(x) U_{b,j}(x) dx = \delta_{ij}. \quad (3-40)$$

The normalized natural frequencies for the first seven modes for a center-pinned beam with zero axial load are listed in Table 3-2. The modes shapes for the first three modes are shown in Figure 3-5.

Table 3-2: Natural frequencies (normalized) of center-pinned beams (zero axial load).

Mode $i$	Natural frequency $\Xi_i$	Comment on symmetry
1	0	Anti-symmetric
2	1.0150	Symmetric
3	4.4509	Anti-symmetric
4	6.3608	Symmetric
5	14.4236	Anti-symmetric
6	17.8105	Symmetric
7	30.0937	Anti-symmetric

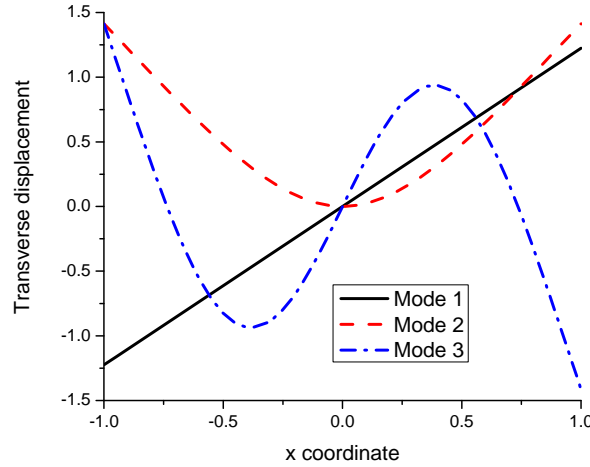


Figure 3-5: First three mode shapes of the beam (zero axial load).

### Transfer function

Assuming the forcing term  $f_b$  and the corresponding displacement  $w_b$  are

$$f_b = \sum_i f_{b,i} U_{b,i}(x) e^{j\omega t}, \quad (3-41)$$

$$w_b = \sum_i w_{b,i} U_{b,i}(x) e^{j\omega t}, \quad (3-42)$$

and substituting them into the governing equation, it can be obtained that

$$\left(-\rho_b h_b b \omega^2 + \rho_b h_b b \omega_{b,i}^2 + \mu_b j \omega\right) w_{b,i} = f_{b,i}, \quad (3-43)$$



where the orthogonal properties have been applied.

Therefore, the transfer function is obtained as

$$\frac{w_{b,i}}{L} = H_{b,i} \frac{f_{b,i}}{E_b b} \quad (3-44)$$

where

$$H_{b,i} = \left( \frac{L}{h_b} \right)^3 \frac{1}{\Xi_i^2 - \Omega_b^2 + \tilde{\mu}_b j \Omega_b}, \quad (3-45)$$

$$\Omega_b = \frac{\omega L^2}{c_b h_b}, \quad (3-46)$$

$$\tilde{\mu}_b = \mu_b \frac{L^2}{b h_b^2 \sqrt{E_b \rho_b}}. \quad (3-47)$$

### 3.4 Diaphragm coupled with an air gap

In this section, a continuum mechanics model is developed to describe a single diaphragm backed by an air gap, which can serve as a platform for studying any pressure sensors that have an air gap underneath the diaphragm for dynamic measurements.

A common complication arises when a pressure sensor contains an air gap backing the vibrating diaphragm. To understand the dynamics of such a sensor structure, one technique is to employ a dynamical analogy converting the involved mechanics to a conventional electric circuitry form (Beranek, 1954; Olson, 1958). In this approach,

usually only the fundamental mode of the diaphragm is considered, and the air gap is replaced by an equivalent elastic spring (i.e. the air spring model). However, this much simplified approach has several limitations. It does not take the full structural-acoustic interaction into account, and thus, it cannot be used to predict the sound field in the air gap. More importantly for sensor design, the estimation of the fundamental frequency is inaccurate in some scenarios, for example, when the height of air gap is very small in micro-electro-mechanical systems (MEMS) pressure sensors.

A more sophisticated approach is to use continuum mechanics governing equations to fully describe the structural-acoustic coupling (Dowell, Gorman Iii, & Smith, 1977; Gladwell & Zimmermann, 1966; Gorman, Reese, Horáček, & Dedouch, 2001; Guy, 1979; Pan, 1992; Pretlove, 1965, 1966; Pretlove & Craggs, 1970; Qaisi, 1988; Rajalingham, Bhat, & Xistris, 1995; Rajalingham, Bhat, & Xistris, 1998). The diaphragm is usually modeled as a thin-plate or a membrane, while the air gap is governed by a wave equation in terms of the pressure field or velocity potential. A geometric compatibility condition is assumed between the diaphragm and the air gap (i.e., equal displacement/velocity at the interface). For example, a multimodal analysis has been used to study the response of a cavity backed panel to external airborne excitation (Guy, 1979). In another work, a receptor-rejector system model has been used to study the vibration of rectangular and circular membranes backed by air cavity. It has been found that the natural frequencies of the coupled system are different from those obtained for an isolated membrane, an open-end cavity, or an closed-end cavity (Rajalingham et al., 1995; Rajalingham et al., 1998). More recently, a similar modal analysis has been employed to study a circular disc

backed by a cylindrical cavity (Gorman et al., 2001). The coupling effects are studied using an analytical-numerical method and a finite element analysis in ANSYS. The numerical results are verified experimentally for a thin steel disc (radius of 38 mm and thickness of 0.38 mm) with a short cavity (81 mm) and a long one (255 mm).

Although the structural-acoustic coupling of the air-backed diaphragm has been extensively studied, few have studied this problem from the perspective of pressure sensor development. Moreover, a fundamental but comprehensive understanding of the effects of the air gap on the diaphragm dynamics is needed. In the literature, free vibrations of a rectangular plate-cavity system have been studied by formulating the mass and stiffness matrices of the plate and the cavity numerically (Qaisi, 1988). A simplified equation is provided to calculate the fundamental natural frequency and it is shown that it increases with decreasing cavity depth. However, this study has several limitations. First, the coefficients of the mass and stiffness matrices for the whole system are frequency-dependent, eliminating the possibility of using linear algebra to solve the eigenvalue problem. Second, the formula for the fundamental frequency only considers the fundamental mode of the plate and the air spring mode of the cavity. As a result, it will become invalid for much shorter cavity depth when the fundamental frequency of the whole system is comparable to the second axisymmetric mode of the plate.

In the following subsections, a normalized solution for the plate-cavity problem will first be derived by using the multimodal analysis approach (continuum model). Then, a distinction is made between the stiffness effect and the mass effect of the air gap, and the solution is recast in a linear matrix form (simplified model). Next, through a

representative example, the variation of the fundamental frequency of the coupled system with respect to the air gap depth is divided into three stages and an approximate formula is provided for each stage.

### 3.4.1 Continuum mechanics model

As depicted in Figure 3-1, a cylindrical coordinate system with normalized coordinates  $(r, \theta, z)$  is established at the center of the diaphragm. The range of the coordinates is  $0 \leq r \leq 1$ ,  $0 \leq \theta \leq 2\pi$ , and  $0 \leq z \leq 1$ . Modal analysis will be employed to derive the transfer function between the external pressure stimulus and the diaphragm response.

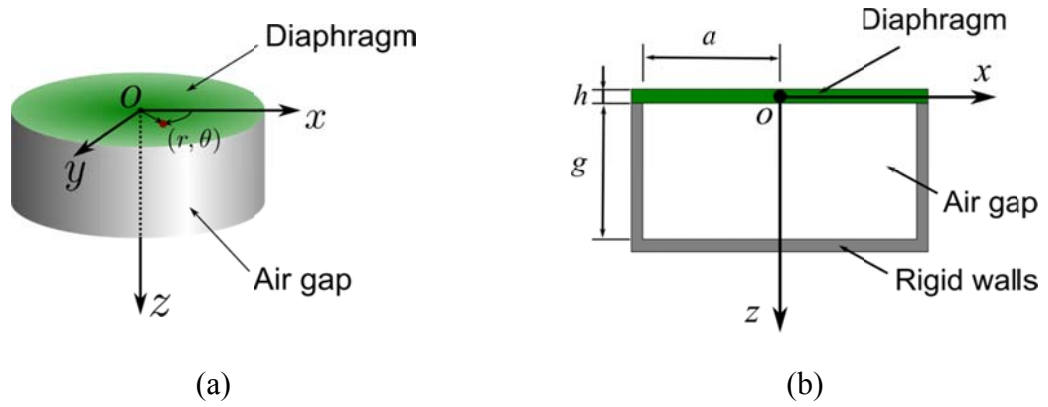


Figure 3-6: A pressure sensor diaphragm backed by an air gap. (a) Schematic of the coordinate system. (b) Cross-section view.

Assume the external pressure applied on the top surface of the plate is

$$p_e(r, \theta, t) = \sum_{m,n} P_{pe,mn} U_{p,mn}(r) \Theta_m(\theta) e^{j\omega t}. \quad (3-48)$$

In response to the external pressure, the reaction pressure at the interface is assumed as

$$p_r(r, \theta, t) = \sum_{m,n} P_{pr,mn} U_{p,mn}(r) \Theta_m(\theta) e^{j\omega t}, \quad (3-49)$$

and the transverse displacement of the diaphragm as

$$w_p(r, \theta, t) = \sum_{m,n} W_{p,mn} U_{p,mn}(r) \Theta_m(\theta) e^{j\omega t}. \quad (3-50)$$

First, the transfer function of the air gap in equation (3-24) is transformed in terms of the diaphragm's modes, that is

$$\frac{P_{pr,mn}}{P_0} = \sum_{k,l} \sum_{s,t} T_{klmn} H_{a,kl} T_{klst} \frac{W_{p,st}}{a}, \quad (3-51)$$

where

$$T_{klmn} = \int_{r=0}^1 U_{a,kl}(r) U_{p,mn}(r) r dr \int_{\theta=0}^{2\pi} \Theta_k(\theta) \Theta_m(\theta) d\theta. \quad (3-52)$$

Combing (3-51) with the transfer function of the diaphragm (Equation (3-10)), it can be obtained for the coupled system that

$$\frac{P_{pe,mn}}{E_p} = \sum_{s,t} H_{ap,mnst} \frac{W_{p,st}}{a}, \quad (3-53)$$

where

$$H_{ap,mnst} = \left[ \frac{P_0}{E_p} \sum_{k,l} (T_{klmn} H_{a,kl} T_{klst}) + H_{p,mn}^{-1} \delta_{ms} \delta_{nt} \right]. \quad (3-54)$$

The natural frequencies and mode shapes of the coupled system can be obtained by finding the roots when the determinant of the matrix  $\{H_{ap}\}$  is equal to zero. In the absence of the air gap, i.e. the chamber underneath the diaphragm is sealed in vacuum,

one can obtain that  $H_{a,kl} = 0$ , and (3-53) reduces to the conventional form for the diaphragm (i.e., Equation (3-10)).

### 3.4.2 Simplified model

Due to the nature of the transfer function of the air gap, the transfer function for the coupled system derived in previous section is different from the conventional form of a constant mass matrix and stiffness matrix, as the coefficient in (3-25) is frequency-dependent. In this section, the continuum model will be simplified according to the different effects of the various modes of the air gap. Assuming the sensor size is much less than the sound wavelength of interest ( $\omega \ll 2\pi c_0/a$ ), which is typically true in most applications, only the axisymmetric modes ( $m = 0$ ) need to be considered.

#### Spring mode of the air gap

For the first mode of the air gap ( $m = 0, n = 0$ ), it can be obtained that  $\beta_{00} = 0$ . The transfer function described in (3-25) reduces to

$$H_{a,00} = -\gamma \frac{g}{a} \Omega_a^2 \cdot \frac{\coth\left(\frac{g}{a} \Omega_a i\right)}{\frac{g}{a} \Omega_a i} = \gamma \frac{\Omega_a}{\tan\left(\frac{g}{a} \Omega_a\right)}. \quad (3-55)$$

Further, if it is assumed that  $\Omega_a g/a \ll 1$ , i.e.  $\omega \ll c_0/g$ , one can obtain  $\tan(\Omega_a g/a) \approx \Omega_a g/a$  and

$$H_{a,00} \approx \gamma \frac{a}{g}. \quad (3-56)$$

The assumption is valid when the excitation frequency is much smaller than the acoustic resonance in the  $z$  direction.

The above equation can be written in terms of the pressure change  $\Delta p$  and the change of gap height  $\Delta g$  as

$$\frac{\Delta p}{\Delta g} = \frac{p_0}{a} H_{a,00} = \gamma \frac{p_0}{g}, \quad (3-57)$$

which is consistent with the commonly known air spring approximation.

### Mass modes of the air gap

For the second and higher modes of the air gap ( $m = 0, n \geq 1$ ), if we assume  $\Omega_a \ll \beta_{01} = 3.8317$  (or  $\omega \ll \beta_{01}c_0/a$ ), it can be obtained that  $\zeta \approx \beta_{0n}g/a$ , and  $H_a$  reduces to

$$H_{a,0n} = -\widetilde{M}_{a,0n}\Omega_a^2 = -M_{a,0n}\Omega_p^2, \quad (3-58)$$

where

$$\widetilde{M}_{a,0n} = \gamma \coth(\beta_{0n}g/a) / \beta_{0n}, \quad (3-59)$$

$$M_{a,0n} = \gamma \frac{\coth(\beta_{0n}g/a)}{\beta_{0n}} \left(\frac{c_p}{c_0}\right)^2 \left(\frac{h_p}{a}\right)^2. \quad (3-60)$$

The assumption  $\omega \ll \beta_{01}c_0/a$  is valid for the case when the excitation frequency is much smaller than the acoustic resonance in the horizontal plane.

Because there is a negative sign in Equation (3-58) and the reaction pressure is applied to the bottom surface of the diaphragm, the effect of these modes is equivalent to increasing the mass of the diaphragm. This effect is more pronounced for a shorter air gap. This phenomenon can be explained by the fact that the air moves together with the diaphragm at the top of the air gap and has zero velocity at the bottom. As the air gap becomes shorter, the velocity gradient increases, rendering a bigger reaction pressure at the interface, which has an opposite sign to the velocity excitation at the interface. As a result, the effect is equivalent to that resulted from increasing the mass of the diaphragm.

The assumptions made in the two scenarios can be combined as

$$\omega \ll \min \left\{ \frac{c_0}{g}, \beta_{01} \frac{c_0}{a} \right\}, \quad (3-61)$$

which means that the excitation frequency is much smaller than any acoustic resonance of the air gap.

### **Simplified model in matrix form**

By assuming the first N modes of the diaphragm and the first M modes of the air gap are used, the forcing  $\mathbf{F}_p$  and response  $\mathbf{W}_p$  term ( $N \times 1$  vectors) can be written as

$$\mathbf{F}_p = \frac{1}{E_p} \begin{bmatrix} F_{p,01} & F_{p,02} & \cdots & F_{p,0N} \end{bmatrix}^T, \quad (3-62)$$

$$\mathbf{W}_p = \frac{1}{a} \begin{bmatrix} W_{p,01} & W_{p,02} & \cdots & W_{p,0N} \end{bmatrix}^T. \quad (3-63)$$



Define the stiffness and mass matrices (M×M) of the air gap as

$$\mathbf{K}_a = \frac{p_0}{E_p} \begin{bmatrix} \gamma \frac{a}{g} & & & \\ & 0 & & \\ & & \ddots & \\ & & & 0 \end{bmatrix}, \quad (3-64)$$

$$\mathbf{M}_a = \frac{p_0}{E_p} \begin{bmatrix} 0 & & & \\ & M_{a,01} & & \\ & & \ddots & \\ & & & M_{a,0(M-1)} \end{bmatrix}. \quad (3-65)$$

Define the stiffness, damping, and mass matrices (N×N) of the diaphragm as

$$\mathbf{K}_p = \frac{1}{1-\nu^2} \left( \frac{h_p}{a} \right)^3 \begin{bmatrix} \Lambda_{01}^2 & & & \\ & \Lambda_{02}^2 & & \\ & & \ddots & \\ & & & \Lambda_{0N}^2 \end{bmatrix}, \quad (3-66)$$

$$\mathbf{C}_p = \frac{1}{1-\nu^2} \left( \frac{h_p}{a} \right)^3 \tilde{\mu} \mathbf{I}_N, \quad (3-67)$$

$$\mathbf{M}_p = \frac{1}{1-\nu^2} \left( \frac{h_p}{a} \right)^3 \mathbf{I}_N, \quad (3-68)$$

where  $\mathbf{I}_N$  is a N×N identity matrix.

The transformation matrix (M×N) takes the following form

$$\mathbf{T} = \begin{bmatrix} T_{0001} & T_{0002} & \cdots & T_{000N} \\ T_{0101} & T_{0102} & \cdots & T_{010N} \\ \vdots & \vdots & \ddots & \vdots \\ T_{0(M-1)01} & T_{0(M-1)02} & \cdots & T_{0(M-1)0N} \end{bmatrix}. \quad (3-69)$$

Then, the transfer function of the air-backed diaphragm can be written in the following compact matrix form as

$$\mathbf{H}_{ap} \mathbf{W}_p = \mathbf{F}_p, \quad (3-70)$$

where

$$\mathbf{H}_{ap} = \mathbf{K}_{ap} + j\Omega_p \mathbf{C}_p - \mathbf{M}_{ap} \Omega_p^2, \quad (3-71)$$

$$\mathbf{K}_{ap} = \mathbf{T}^T \mathbf{K}_a \mathbf{T} + \mathbf{K}_p, \quad (3-72)$$

$$\mathbf{M}_{ap} = \mathbf{T}^T \mathbf{M}_a \mathbf{T} + \mathbf{M}_p. \quad (3-73)$$

Since the diaphragm radius is assumed to be much smaller than the sound wavelength, the sound field impinging on the diaphragm will be uniformly distributed, which can be described as  $\tilde{p}e^{j\alpha}$ . As a result, the  $n$ th component of the forcing vector  $\mathbf{F}_p$  can be obtained as

$$F_{p,on} = \sqrt{2\pi} \frac{\tilde{p}}{E} \int_{r=0}^1 U_{p,0n}(r) r dr. \quad (3-74)$$

Once the displacement vector  $\mathbf{W}_p$  is solved, the center displacement  $w_c$  can be obtained as

$$w_c = \mathbf{B}_p^T \mathbf{W}_p, \quad (3-75)$$

where  $\mathbf{B}_p$  is an  $N \times 1$  vector and its  $n$ th component  $B_{p,0n}$  is

$$B_{p,0n} = U_{p,0n}(r=0) \Theta_0 = U_{p,0n}(r=0) / \sqrt{2\pi}. \quad (3-76)$$

## Results and discussion

To investigate the effects of the air gap on the performance of pressure sensors, a representative pressure sensor is used. The dimensions of the sensor is  $a = 500 \mu\text{m}$ , and  $h_p = 0.5 \mu\text{m}$ . It is made of silicon ( $E = 169 \text{ GPa}$ ,  $\nu = 0.25$ ,  $\rho = 2.3 \times 10^3 \text{ kg/m}^3$ ). The air in the gap is at room temperature conditions ( $p_0 = 1.01 \times 10^5 \text{ Pa}$ ,  $c_0 = 343 \text{ m/s}$ ).

First, the effects of air gap on the static sensitivity of the air-backed diaphragm are studied. As shown in Figure 3-7, the static sensitivity decreases as the air gap becomes shorter. In addition, the difference in the results obtained from the continuum mechanics model, the simplified model, and even the air spring model ( $N = 1$ ,  $M = 1$ ) is negligible.

Next, the effects of air gap on the fundamental frequency of the air-backed diaphragm are investigated. In the continuum mechanics model, as shown in Figure 3-8, when the air gap is long, the fundamental frequency is close to that of the closed-ended cavity. This can be explained by the fact that the diaphragm has a much higher stiffness than the air gap so that the diaphragm can be regarded as a rigid wall for the air gap. As the air gap becomes shorter, the fundamental frequency increases and saturates before dropping in the much shorter air gap range. The air gap has two functions, one as an spring to increase the equivalent stiffness of the diaphragm, and the other as an added mass to

increase the equivalent mass of the diaphragm. Therefore, for longer air gaps, the spring effect dominates, while for shorter air gaps, the mass effect is more pronounced.

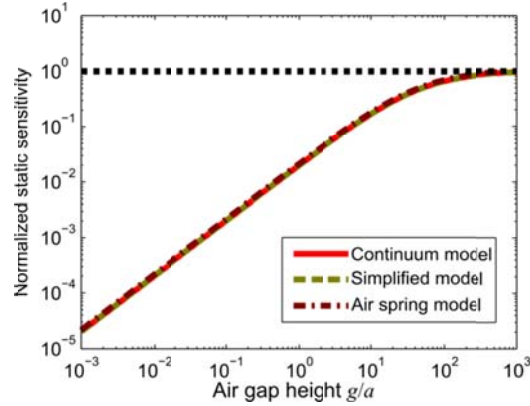


Figure 3-7: Static sensitivity of the center displacement of a diaphragm backed by air gaps with respect to air gap height. The static sensitivity is normalized by that for the same diaphragm without the air gap (*in vacuo*).

The results obtained with the simplified model ( $N = 5$ ,  $M = 5$ ) (see Figure 3-8) exhibit similar behavior as the continuum mechanics model for short air gaps. However, for longer air gaps, the simplified model cannot capture those acoustic modes obtained by using the continuum mechanics model. For the simplified model,  $\Omega_1$  is close to the fundamental frequency of the diaphragm *in vacuo* for long air gaps. However, since the emphasis here is to study the effects of the structural characteristics of the diaphragm on sensory performance, there is no need to distinguish the structural modes from the acoustic modes. The simplified model will therefore be used in the following analysis.

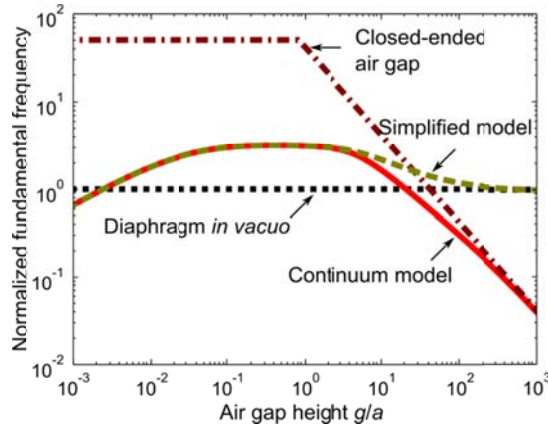


Figure 3-8: The fundamental frequency of an air-backed diaphragm (normalized by that of the same diaphragm *in vacuo*) for various air gap heights. The diaphragm is made of silicon, and its dimensions are  $500 \mu\text{m} \times 0.5 \mu\text{m}$  (radius  $\times$  thickness). In this plot, the continuum model and simplified model are compared to the close-ended cavity and the diaphragm *in vacuo*.

Here, in order to well quantify the spring and mass effects, the minimum numbers of modes for the diaphragm and the air gap are determined. Clearly, the change of the air-backed diaphragm's fundamental frequency  $\Omega_1$  with respect to the air gap height can be characterized in three stages, as shown in Figure 3-9. In the up-slope stage, the increase of  $\Omega_1$  can be simply captured by the air spring model ( $N = 1, M = 1$ ), until it reaches the plateau stage where it can be modeled by including one more diaphragm's mode ( $N = 2, M = 1$ ). To describe the down-slope stage, the mass effect mode of the air gap has to be included. The overall characteristics of the variation of  $\Omega_1$  can be well captured by using two modes for both the diaphragm and the air gap ( $N = 2, M = 2$ ).

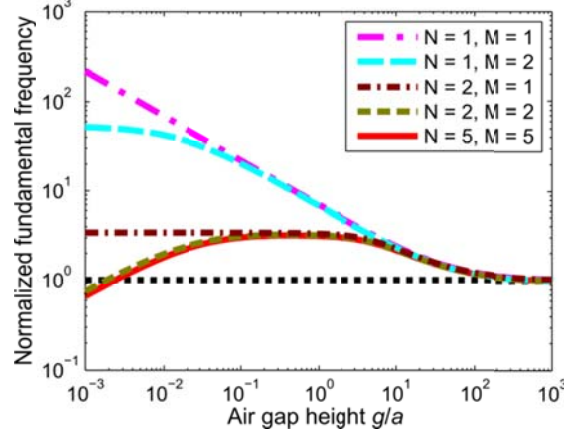


Figure 3-9: Effects of number of modes used in the simplified model on the calculated fundamental frequency (normalized by that of the same diaphragm *in vacuo*). The diaphragm is made of silicon, and its dimensions are  $500 \mu\text{m} \times 0.5 \mu\text{m}$  (radius  $\times$  thickness).

### Closed-forms of the 3-stage approximation

While the developed simplified model can be used to study the effects of the air gap, a more straightforward method to estimate the fundamental frequency can be developed to facilitate the design of pressure sensors, which will be described next to provide closed-form estimations for the three stages.

In the up-slope stage,  $\Omega_1$  can be estimated by the air spring model ( $N = 1, M = 1$ ), where the stiffness matrix  $\mathbf{K}_{ap}$  reduces to a scalar form as

$$K_{ap} = \frac{1}{1-\nu^2} \left( \frac{h_p}{a} \right)^3 \Lambda_{01}^2 + T_{11} \frac{p_0}{E} \gamma \frac{a}{g}. \quad (3-77)$$

The fundamental frequency of the air spring model  $\Omega_{1,up}$  can thus be calculated as

$$\Omega_{1,up} = \sqrt{\Lambda_{01}^2 + T_{11} / \mathcal{G}}, \quad (3-78)$$

where

$$\mathcal{G} = \frac{1}{\gamma(1-\nu^2)} \frac{E_p}{p_0} \left( \frac{h_p}{a} \right)^3 \frac{\mathcal{G}}{a}. \quad (3-79)$$

If the diaphragm is a pure plate (without in-plane force), it can be obtained that  $\Lambda_{01} = 2.9490$ , and  $T_{11} = 0.7287$ .

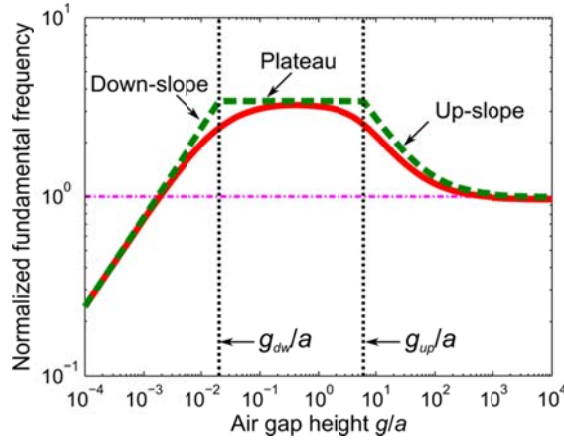


Figure 3-10: A 3-stage approximation of the fundamental frequency of an air-backed diaphragm (normalized by that of the same diaphragm in *vacuo*) as air gap height changes. The diaphragm is made of silicon, and its dimensions are  $500 \mu\text{m} \times 0.5 \mu\text{m}$  (radius  $\times$  thickness). In this plot, the fundamental frequency (red solid line) is obtained by using the simplified model ( $N = 2, M = 2$ ).

To estimate  $\Omega_1$  at the plateau stage, the first two modes of the diaphragm and the air spring mode of the air gap ( $N = 2, M = 1$ ) are used. In this case, the transfer function of the air-backed diaphragm  $\mathbf{H}_{ap}$  reduces to

$$\mathbf{H}_{ap} = \frac{1}{1-\nu^2} \left( \frac{h_p}{a} \right)^3 \begin{bmatrix} \Lambda_{01}^2 + T_{11}^2 / \mathcal{G} - \Omega^2 & T_{11}T_{12} / \mathcal{G} \\ T_{11}T_{12} / \mathcal{G} & \Lambda_{02}^2 + T_{12}^2 / \mathcal{G} - \Omega^2 \end{bmatrix}, \quad (3-80)$$

$\Omega_1$  can be obtained by finding the root of the determinant of  $\mathbf{H}_{ap}$ , i.e.

$$\lambda_1 = \Omega_1^2 = \frac{\Lambda_{01}^2 + \Lambda_{02}^2 + (T_{11}^2 + T_{12}^2) / \mathcal{G}}{2} - \frac{1}{2} \sqrt{\left( (T_{11}^2 + T_{12}^2) / \mathcal{G}^2 + 2(\Lambda_{01}^2 - \Lambda_{02}^2)(T_{11}^2 - T_{12}^2) / \mathcal{G} + (\Lambda_{01}^2 - \Lambda_{02}^2)^2 \right)}. \quad (3-81)$$

As  $g \rightarrow 0$ ,  $\mathcal{G} \rightarrow 0$ , and  $\Omega_1$  approaches the plateau value  $\Omega_{1,plt}$

$$\Omega_{1,plt} = \sqrt{\frac{\Lambda_{02}^2 + \Lambda_{01}^2}{2} + \frac{\Lambda_{02}^2 - \Lambda_{01}^2}{2} \frac{T_{11}^2 - T_{12}^2}{T_{11}^2 + T_{12}^2}}. \quad (3-82)$$

If the diaphragm is a pure plate (without in-plane force),  $\Omega_{1,plt}$  is equal to 10.1034, as compared to 2.9490 and 11.4809 for  $\Lambda_{01}$  and  $\Lambda_{02}$ , respectively.

To estimate  $\Omega_1$  in the down-slope stage, the simplified model ( $N = 2$ ,  $M = 2$ ) is used, for which the transfer function is (assuming  $\coth(\beta_{01}g/a) \approx a/(\beta_{01}g)$  for short air gaps)

$$\mathbf{H}_{ap} = \gamma \frac{p_0}{E_p} \frac{a}{g} \begin{bmatrix} T_{11}^2 + \mathcal{G}\Lambda_{01}^2 - (\sigma T_{21}^2 + \mathcal{G})\Omega^2 & T_{11}T_{12} - \sigma T_{21}T_{22}\Omega^2 \\ T_{11}T_{12} - \sigma T_{21}T_{22}\Omega^2 & T_{12}^2 + \mathcal{G}\Lambda_{02}^2 - (\sigma T_{22}^2 + \mathcal{G})\Omega^2 \end{bmatrix}, \quad (3-83)$$

where

$$\sigma = \frac{1}{\beta_{01}^2} \left( \frac{c_p}{c_0} \right)^2 \left( \frac{h_p}{a} \right)^2. \quad (3-84)$$

From the determinant of  $\mathbf{H}_{ap}$ ,  $\Omega_1$  can be obtained as follows



$$\Omega_1^2 = \frac{(\Lambda_{01}^2 + \Lambda_{02}^2)\mathcal{G}^2 + Q_2\mathcal{G} + Q_1}{2\mathcal{G}^2 + 2Q_3\mathcal{G}}, \quad (3-85)$$

$$- \frac{\sqrt{[(\Lambda_{01}^2 + \Lambda_{02}^2)\mathcal{G}^2 + Q_2\mathcal{G} + Q_1]^2 - 4(\mathcal{G}^2 + Q_3\mathcal{G})(\Lambda_{01}^2\Lambda_{02}^2\mathcal{G}^2 + Q_4\mathcal{G})}}{2\mathcal{G}^2 + 2Q_3\mathcal{G}},$$

where

$$Q_1 = \sigma(T_{12}T_{21} - T_{11}T_{22})^2, \quad (3-86)$$

$$Q_2 = \sigma(T_{21}^2\Lambda_{02}^2 + T_{22}^2\Lambda_{01}^2) + (T_{11}^2 + T_{12}^2), \quad (3-87)$$

$$Q_3 = \sigma(T_{21}^2 + T_{22}^2), \quad (3-88)$$

$$Q_4 = (T_{11}^2\Lambda_{02}^2 + T_{12}^2\Lambda_{01}^2). \quad (3-89)$$

Note that Equation (3-85) is the closed-form equation to calculate the fundamental frequency of the coupled system in all three stages. However, as  $g/a \rightarrow 0$ ,  $\mathcal{G} \rightarrow 0$ , and  $\Omega_1 \rightarrow 0$ . Therefore,  $\Omega_1$  can be approximated by

$$\Omega_{1,dw} = \sqrt{\frac{Q_4}{Q_1}}\mathcal{G} = k_{dw}\sqrt{\frac{\rho_p}{\rho_0}\frac{h_p}{a}\frac{g}{a}}, \quad (3-90)$$

where

$$k_{dw} = \frac{\sqrt{T_{11}^2\Lambda_{02}^2 + T_{12}^2\Lambda_{01}^2}}{|T_{12}T_{21} - T_{11}T_{22}|}\beta_{01}. \quad (3-91)$$

If the diaphragm is a pure plate (without in-plane force),  $k_{dw} = 51.5651$ .

The two critical air gaps, marked in Figure 3-10, can be calculated from Equations (3-78), (3-82), and (3-90) as

$$\frac{g_{up}}{a} = \gamma (1 - \nu^2) \frac{p_0}{E_p} \left( \frac{a}{h_p} \right)^3 \frac{T_{11}}{\Omega_{1,plt}^2 - \Lambda_{01}^2}, \quad (3-92)$$

$$\frac{g_{dw}}{a} = \frac{\rho_0}{\rho_p} \frac{a}{h_p} \left( \frac{\Omega_{1,plt}}{k_{dw}} \right)^2. \quad (3-93)$$

For the representative example, these critical values are calculated as  $g_{up} = 3.0705$  mm and  $g_{dw} = 10.0491$   $\mu$ m.

### 3.4.3 Parametric studies

Equations (3-92) and (3-93), which can be used to calculate the two critical gaps, are used here to study how the structural parameters affect the variation of  $\Omega_1$  with respect to the air gap height.

The first parameter to study is the Young's modulus of the diaphragm  $E_p$ . Equations (3-92) and (3-93) indicate that  $g_{up}$  is inversely proportional to  $E_p$ , while  $g_{dw}$  is independent of  $E_p$ . As  $E_p$  increases (other parameters are kept constant), as shown in Figure 3-11(a), the up-slope region shifts to the left, but the down-slope region does not move. In the up-slope region, for the same air gap height, increasing  $E_p$  leads to a smaller  $\Omega_1$ , which can be seen from equation Equation (3-78). An increase in  $E_p$  can also results in a narrower plateau, which disappears if  $E_p$  is larger than a critical value.

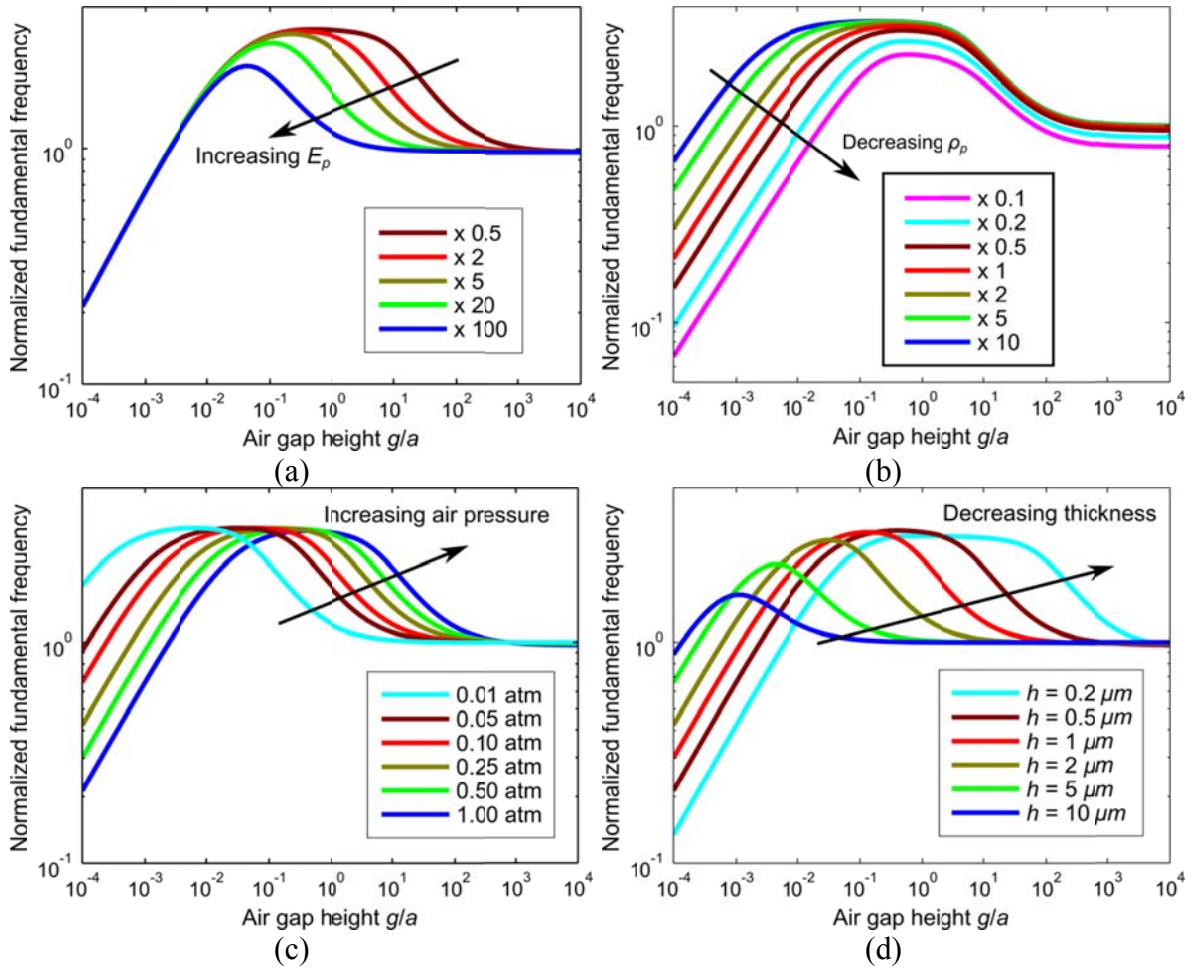


Figure 3-11: The variation of the fundamental frequency of an air-backed diaphragm (normalized by that of the same diaphragm in *vacuo*) as a function of air gap height. (a) The Young's modulus of the diaphragm changing from 0.5 to 100 times Silicon's. (b) The diaphragm's density changing from 0.1 to 10 times Silicon's. (c) Pressure level of the air gap changing from 0.01 atm to 1 atm (assuming the temperature does not change). (d) The diaphragm thickness changing from  $0.2 \mu\text{m}$  to  $10 \mu\text{m}$ .

The second parameter to study is the diaphragm's density  $\rho_p$ . Equations (3-92) and (3-93) indicate that  $g_{dw}$  is inversely proportional to  $\rho_p$ , while  $g_{up}$  is independent of  $\rho_p$ . When  $\rho_p$  is decreased (other parameters are kept constant), as shown in Figure 3-11(b), the down-slope region moves to the right, but the up-slope region does not change. In the down-slope region, for the same air gap height, decreasing  $\rho_p$  leads to a smaller  $\Omega_1$ , which can

be seen from Equation (3-78). Also based on Equation (3-90), the slope of the down-slope region in a log-log plot is not affected by the change of  $\rho_p$ . Decreasing  $\rho_p$  also results in a narrower plateau, which disappears if  $\rho_p$  is smaller than a critical value.

In the third case, the influence of the static pressure in the air gap  $p_0$  is investigated. Assuming the temperature is kept constant at room temperature, the air density  $\rho_0$  changes proportionally with  $p_0$ . Since  $g_{up}/g_{dw}$  is proportional to  $p_0/\rho_0$ , decreasing the air pressure will result in a shift of the entire curve to the left in the log-log plot, as shown in Figure 3-11(c). It is intuitive that as the air density becomes smaller, the air gap needs to be shorter to have the same spring and mass effects.

In the last scenario, the effect of the diaphragm thickness  $h$  is studied. From Equations (3-92) and (3-93), it can be seen that  $g_{up}/g_{dw}$  is proportional to  $(a/h)^2$ . Therefore, as  $h$  increases, the plateau region becomes smaller in the log-log plot, as shown in Figure 3-11(d), although both the up-slope region and the down-slope region move to the left. In the up-slope region, as  $h$  increases,  $\Omega_1$  decreases for a fixed air gap height  $g$ , and its slope with respect to  $g$  becomes smaller due to the increased stiffness of the diaphragm. In the down-slope region, a thinner diaphragm leads to a smaller  $\Omega_1$ .

### **3.5 Modeling of diaphragms coupled through a bridge**

In this section, the previous derived transfer functions for the air-backed diaphragm and the bridge will be combined to model the fly-ear inspired directional microphones. Assume the pressure load on the left and right diaphragms are

$$\begin{cases} p_{pL}(r, \theta, t) = \sum_{m,n} P_{pL,mn} U_{p,mn}(r) \Theta_m(\theta) e^{j\omega t} \\ p_{pR}(r, \theta, t) = \sum_{m,n} P_{pR,mn} U_{p,mn}(r) \Theta_m(\theta) e^{j\omega t} \end{cases} \quad (3-94)$$

The pressure load consists of the external pressure load  $p_{eL}, p_{eR}$ , and the reaction pressure from the bridge  $p_{rL}, p_{rR}$  (i.e., coupling force). The reaction pressure is due to a concentrated force described by

$$\begin{cases} p_{rL}(r \neq 0) = 0, p_{rL}(r = 0) = \infty, 2\pi a^2 \int_{r=0}^1 p_{rL}(r) r dr = F_{rL} \\ p_{rR}(r \neq 0) = 0, p_{rR}(r = 0) = \infty, 2\pi a^2 \int_{r=0}^1 p_{rR}(r) r dr = F_{rR} \end{cases} \quad (3-95)$$

The external pressure can be written as

$$\begin{cases} p_{eL}(r, \theta, t) = \sum_{m,n} P_{eL,mn} U_{p,mn}(r) \Theta_m(\theta) e^{j\omega t} \\ p_{eR}(r, \theta, t) = \sum_{m,n} P_{eR,mn} U_{p,mn}(r) \Theta_m(\theta) e^{j\omega t} \end{cases} \quad (3-96)$$

Combining Equations (3-94)-(3-96), it can be obtained that

$$\begin{cases} P_{pL,mn} = -\frac{U_{p,mn}(r=0) \delta_{m0} \Theta_0}{a^2} F_{rL} + P_{eL,mn} \\ P_{pR,mn} = -\frac{U_{p,mn}(r=0) \delta_{m0} \Theta_0}{a^2} F_{rR} + P_{eR,mn} \end{cases} \quad (3-97)$$

The load (force per unit length) on the bridge is assumed to be solely caused by the reaction force; that is

$$f_b = \frac{1}{L_b} [F_{rL} \delta(x+1) + F_{rR} \delta(x-1)] e^{j\omega t} = \sum_i F_{b,i} U_{b,i}(x) e^{j\omega t}, \quad (3-98)$$

where

$$F_{b,i} = \frac{1}{L_b} \left( F_{rL} U_{b,i} \Big|_{x=-1} + F_{rR} U_{b,i} \Big|_{x=1} \right). \quad (3-99)$$

In response to the pressure load, assume the displacement of the two plates and the bridge are

$$\begin{cases} w_{pL}(r, \theta, t) = \sum_{m,n} W_{pL,mn} U_{p,mn}(r) \Theta_m(\theta) e^{j\omega t} \\ w_{pR}(r, \theta, t) = \sum_{m,n} W_{pR,mn} U_{p,mn}(r) \Theta_m(\theta) e^{j\omega t} \\ w_b(x, t) = \sum_i W_{b,i} U_{b,i}(x) e^{j\omega t} \end{cases}. \quad (3-100)$$

Based on Equations (3-53) and (3-44), one can obtain

$$\begin{cases} \frac{W_{pL,mn}}{a} = \sum_{s,t} H_{ap,mnst}^{-1} \frac{P_{pL,st}}{E_p} \\ \frac{W_{pR,mn}}{a} = \sum_{s,t} H_{ap,mnst}^{-1} \frac{P_{pR,st}}{E_p} \\ \frac{W_{b,i}}{L} = H_{b,i} \frac{F_{b,i}}{E_b b} \end{cases}. \quad (3-101)$$

The geometric compatibility at the diaphragm center can be described as

$$\begin{cases} w_{pL}(r=0) = w_b(x=-1) \\ w_{pR}(r=0) = w_b(x=1) \end{cases}, \quad (3-102)$$

or

$$\begin{cases} \sum_n W_{pL,0n} U_{p,0n} \Big|_{r=0} \Theta_0 = \sum_i W_{b,i} U_{b,i} \Big|_{x=-1} \\ \sum_n W_{pR,0n} U_{p,0n} \Big|_{r=0} \Theta_0 = \sum_i W_{b,i} U_{b,i} \Big|_{x=1} \end{cases} . \quad (3-103)$$

Because  $U_{p,mn}(r=0) = 0$  for  $m \neq 0$  and the center displacement will be measured by a detection system, only the axisymmetric modes ( $m = 0$ ) will be considered. For simplicity, these equations will be recast in matrix forms next.

The forcing terms for the two plates in Equation (3-97) are written as

$$\mathbf{P}_{pL} = \mathbf{P}_{eL} - \frac{1}{a^2} \mathbf{B}_p F_{rL} , \quad (3-104)$$

$$\mathbf{P}_{pR} = \mathbf{P}_{eR} - \frac{1}{a^2} \mathbf{B}_p F_{rR} , \quad (3-105)$$

where

$$\mathbf{P}_{pL} = \{P_{pL,0n}\} , \mathbf{P}_{pR} = \{P_{pR,0n}\} , \quad (3-106)$$

$$\mathbf{P}_{eL} = \{P_{eL,0n}\} , \mathbf{P}_{eR} = \{P_{eR,0n}\} , \quad (3-107)$$

$$\mathbf{B}_p = \{U_{p,0n}(r=0)\Theta_0\} . \quad (3-108)$$

The forcing term on the bridge (beam) in Equation (3-99) is written as

$$\mathbf{F}_b = \frac{1}{L} \mathbf{B}_{bL} F_{rL} + \frac{1}{L} \mathbf{B}_{bR} F_{rR} , \quad (3-109)$$

where

$$\mathbf{F}_b = \{F_{b,i}\}, \quad (3-110)$$

$$\mathbf{B}_{bL} = \{U_{b,i}|_{x=-1}\}, \mathbf{B}_{bR} = \{U_{b,i}|_{x=1}\}. \quad (3-111)$$

The transfer functions in Equation (3-101) are written as

$$\frac{\mathbf{W}_{pL}}{a} = \mathbf{H}_{ap}^{-1} \frac{\mathbf{P}_{pL}}{E_p}, \quad (3-112)$$

$$\frac{\mathbf{W}_{pR}}{a} = \mathbf{H}_{ap}^{-1} \frac{\mathbf{P}_{pR}}{E_p}, \quad (3-113)$$

$$\frac{\mathbf{W}_b}{L} = \mathbf{H}_b \frac{\mathbf{F}_b}{E_b b}, \quad (3-114)$$

where

$$\mathbf{W}_{pL} = \{W_{pL,0n}\}, \mathbf{W}_{pR} = \{W_{pR,0n}\}, \mathbf{W}_b = \{W_{b,i}\}, \quad (3-115)$$

$$\mathbf{H}_{ap} = [H_{ap,0n0t}], \mathbf{H}_b = \text{diag}\{H_{b,i}\}. \quad (3-116)$$

The geometric compatibility described in Equation (3-103) can be written as

$$\mathbf{B}_p^T \mathbf{W}_{pL} = \mathbf{B}_{bL}^T \mathbf{W}_b, \quad (3-117)$$

$$\mathbf{B}_p^T \mathbf{W}_{pR} = \mathbf{B}_{bR}^T \mathbf{W}_b. \quad (3-118)$$

Combining all the above matrix form equations, the following equations in terms of the reaction forces can be obtained



$$\left\{ \mathbf{B}_p^T \mathbf{H}_{ap}^{-1} \mathbf{B}_p + \frac{E_p}{E_b} \frac{a}{b} \mathbf{B}_{bL}^T \mathbf{H}_b \mathbf{B}_{bL} \right\} F_{rL} + \frac{E_p}{E_b} \frac{a}{b} \mathbf{B}_{bL}^T \mathbf{H}_b \mathbf{B}_{bR} F_{rR} = \mathbf{B}_p^T \mathbf{H}_{ap}^{-1} \mathbf{P}_{eL} a^2, \quad (3-119)$$

$$\frac{E_p}{E_b} \frac{a}{b} \mathbf{B}_{bR}^T \mathbf{H}_b \mathbf{B}_{bL} F_{rL} + \left\{ \mathbf{B}_p^T \mathbf{H}_{ap}^{-1} \mathbf{B}_p + \frac{E_p}{E_b} \frac{a}{b} \mathbf{B}_{bR}^T \mathbf{H}_b \mathbf{B}_{bR} \right\} F_{rR} = \mathbf{B}_p^T \mathbf{H}_{ap}^{-1} \mathbf{P}_{eR} a^2. \quad (3-120)$$

The above two equations can be rewritten in a more compact matrix form as

$$\mathbf{H}_R \mathbf{F}_R = \mathbf{N} \mathbf{P}_e a^2, \quad (3-121)$$

where

$$\mathbf{H}_R = \frac{E_p}{E_b} \frac{a}{b} \mathbf{B}_b^T \mathbf{H}_b \mathbf{B}_b + \mathbf{B}_p^T \mathbf{H}_{ap}^{-1} \mathbf{B}_p \mathbf{I}_2, \quad (3-122)$$

$$\mathbf{N} = \begin{bmatrix} \mathbf{B}_p^T \mathbf{H}_{ap}^{-1} & \\ & \mathbf{B}_p^T \mathbf{H}_{ap}^{-1} \end{bmatrix}, \quad (3-123)$$

$$\mathbf{B}_b = [\mathbf{B}_{bL} \quad \mathbf{B}_{bR}], \quad (3-124)$$

$$\mathbf{P}_e = \begin{Bmatrix} \mathbf{P}_{eL} \\ \mathbf{P}_{eR} \end{Bmatrix}. \quad (3-125)$$

From Equation (3-121), the reaction force can be solved as

$$\mathbf{F}_R = \mathbf{H}_R^{-1} \mathbf{N} \mathbf{P}_e a^2. \quad (3-126)$$

Once the reaction forces at the connecting joints are known, the displacement solutions for the diaphragms and the bridge can be obtained as follows

$$\frac{\mathbf{W}_p}{a} = \mathbf{H}_{sp} \frac{\mathbf{P}_e}{E_p}, \quad (3-127)$$

$$\frac{\mathbf{W}_b}{a} = \mathbf{H}_{sb} \frac{\mathbf{P}_e}{E_p}, \quad (3-128)$$

where

$$\mathbf{W}_p = \begin{Bmatrix} \mathbf{W}_{pL} \\ \mathbf{W}_{pR} \end{Bmatrix}, \quad (3-129)$$

$$\mathbf{H}_{sp} = \begin{bmatrix} \mathbf{H}_{ap}^{-1} & \\ & \mathbf{H}_{ap}^{-1} \end{bmatrix} \left\{ \mathbf{I}_{2N} - \begin{bmatrix} \mathbf{B}_p & \\ & \mathbf{B}_p \end{bmatrix} \mathbf{H}_R^{-1} \mathbf{N} \right\}, \quad (3-130)$$

$$\mathbf{H}_{sb} = \frac{a}{b} \frac{E_p}{E_b} \mathbf{H}_b \mathbf{B}_b \mathbf{H}_R^{-1} \mathbf{N}. \quad (3-131)$$

When a sinusoidal plane sound wave impinges on the directional microphone, the forcing terms can be calculated as

$$P_{eL,0n} = p_m \sqrt{2\pi} \exp\left(-j2\pi \frac{L}{\lambda} \sin \theta\right) \int_{r=0}^1 U_{p,0n}(r) r dr, \quad (3-132)$$

$$P_{eR,0n} = p_m \sqrt{2\pi} \exp\left(j2\pi \frac{L}{\lambda} \sin \theta\right) \int_{r=0}^1 U_{p,0n}(r) r dr, \quad (3-133)$$

where  $p_m$  is the pressure field at the pivot, and  $\theta$  is the incident azimuth. The phase term  $2\pi L/\lambda$  can also be written as

$$2\pi \frac{L}{\lambda} = \frac{\omega L}{c_0} = \Omega_p \frac{c_p}{c_0} \frac{h_p}{a} \frac{L}{a}. \quad (3-134)$$

### 3.6 Validation of the continuum mechanics model

#### 3.6.1 Validation of the model with a finite element model

In this section, the developed continuum mechanics model will be validated by a finite element model in ANSYS. To facilitate the comparison, a representative design is chosen with the parameters listed in Table 3-3.

A finite element model is created by using a commercial finite element method (FEM) software ANSYS (Version 13.0), as shown in Figure 3-12. Shell elements (SHELL181, 2950 elements) are chosen to model both the diaphragms and the coupling bridge, and 3-D acoustic fluid elements (FLUID30, 53000 elements) are used to model the air gap. Fluid-structure interaction (FSI) flag is created at the interface between the diaphragms and the air to ensure the coupling of displacement and pressure field.

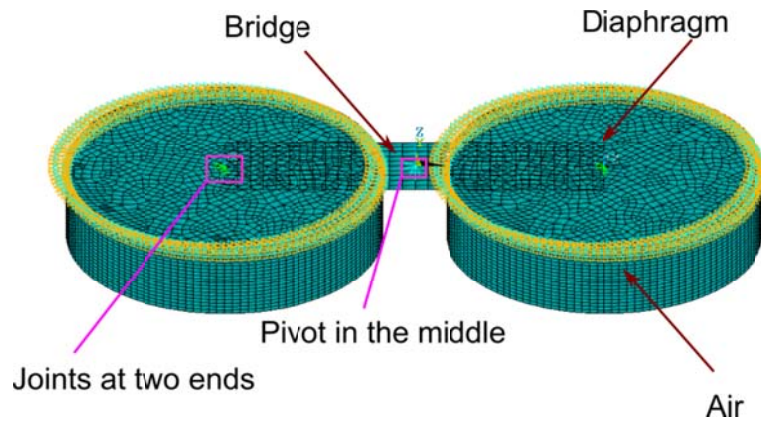


Figure 3-12: Finite element modeling (ANSYS) of fly-ear inspired directional microphones

Table 3-3: Parameters of a representative fly-ear inspired directional microphone

Parameters	Values	Parameters	Values
Diaphragm (silicon)		Bridge (silicon nitride)	
<i>Young's modulus <math>E_p</math></i>	169 GPa	<i>Young's modulus <math>E_b</math></i>	290 GPa
<i>Poisson's ratio <math>\nu</math></i>	0.25	<i>Density <math>\rho_p</math></i>	3100 kg/m <sup>3</sup>
<i>Density <math>\rho_p</math></i>	2300 kg/m <sup>3</sup>	<i>Length <math>2L</math></i>	1.2 mm
<i>Radius <math>a</math></i>	500 $\mu\text{m}$	<i>Width <math>b</math></i>	300 $\mu\text{m}$
<i>Thickness <math>h_p</math></i>	0.5 $\mu\text{m}$	<i>Thickness <math>h_b</math></i>	2.5 $\mu\text{m}$
<i>In-plane tension <math>N_0</math></i>	0	<i>Axial load</i>	0
<i>Damping <math>\mu_p</math></i>	0	<i>Damping <math>\mu_b</math></i>	0
Air gap			
<i>Static pressure</i>	101325 Pa	<i>Air gap height <math>g</math></i>	250 $\mu\text{m}$
<i>Sound speed</i>	343 m/s		

For the boundary conditions, except for the top surface, the air gap is constrained by surrounding rigid walls (this is the default boundary condition). The translational degrees of freedom (DOFs) of the diaphragm and the bridge are coupled at the joints (equal translational displacements), and the bridge is pinned in the middle (zero translational displacements).

The mode shapes and natural frequencies for the mechanically coupled microphone with and without considering the effects of the air gap are compared in Table 3-4 and Table 3-5. Overall, the results obtained from the analytical model agree well with those obtained with ANSYS. In addition to the discretization in the FEM and the numerical calculation error, the slight discrepancy is largely due to the fact that the bridge is described by an Euler-Bernoulli beam in the analytical model, while it is modeled using shell elements in ANSYS.

Table 3-4: Mode shapes and natural frequencies of mechanically coupled microphone without air gap (comparison between analytical model and finite element model)

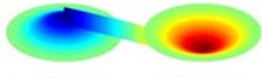



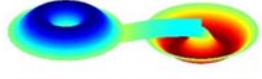
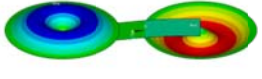
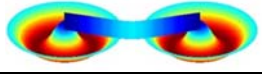
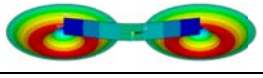
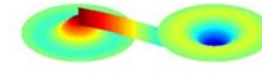
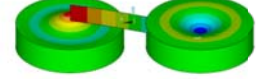
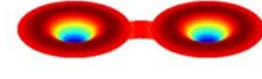
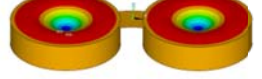
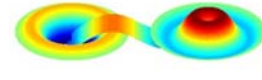
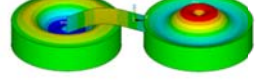


	Analytical model (Matlab)		Finite element model (ANSYS)	
	Mode shape	Natural frequency (kHz)	Mode shape	Natural frequency (kHz)
1 <sup>st</sup> Rocking		4.04		4.03
1 <sup>st</sup> Bending		10.05		10.13
2 <sup>nd</sup> Rocking		19.95		19.67
2 <sup>nd</sup> Bending		21.26		21.02

Table 3-5: Mode shapes and natural frequencies of mechanically coupled microphone with air gap (comparison between analytical model and finite element model)

	Analytical model (Matlab)		Finite element model (ANSYS)	
	Mode shape	Natural frequency (kHz)	Mode shape	Natural frequency (kHz)
1 <sup>st</sup> Rocking		8.56		8.39
1 <sup>st</sup> Bending		14.18		14.18
2 <sup>nd</sup> Rocking		42.47		42.29
2 <sup>nd</sup> Bending		47.82		46.79

It should be noted that the air gap has a significant effect on the natural frequencies and mode shapes. For example, with an air gap, the natural frequencies for the first rocking and bending modes increase from 4.04 kHz and 10.05 kHz to 8.56 kHz and 14.18 kHz,

respectively (using the analytical model). There are also noticeable differences in the mode shapes. For example, with an air gap, the displacement in the mode shapes is more concentrated around the diaphragm center.

### **3.6.2 Comparison of the continuum mechanics model with the lumped model**

Here, the frequency response of the diaphragm obtained with the continuum mechanics model will be compared with that obtained from the equivalent two degrees-of-freedom model described in Chapter 2. To do this, the static stiffness of the diaphragm, the two natural frequencies, and the two damping ratios should be obtained and used in the 2-DOF model. To simplify the problem for the validation purpose, the damping ratios are assumed to be zero. The other three parameters are equal to those obtained from the analytical model.

The spectra of the diaphragm's center displacement are shown in Figure 3-13 for two scenarios: with and without the air gap. The incident azimuth is chosen as  $90^\circ$  so that the rocking mode can be excited. Note that if the system's damping is zero, the displacements of the two diaphragm centers have same absolute magnitudes. As can be seen from Figure 3-13(a), the continuum model can capture multiple rocking and bending modes, while the lumped model can only capture the first rocking and the first bending modes. Furthermore, the results in Figure 3-13(b) confirm that including an air gap will shift the natural frequencies. In both scenarios, the results obtained with the lumped model agree well with those obtained with the continuum mechanics model.

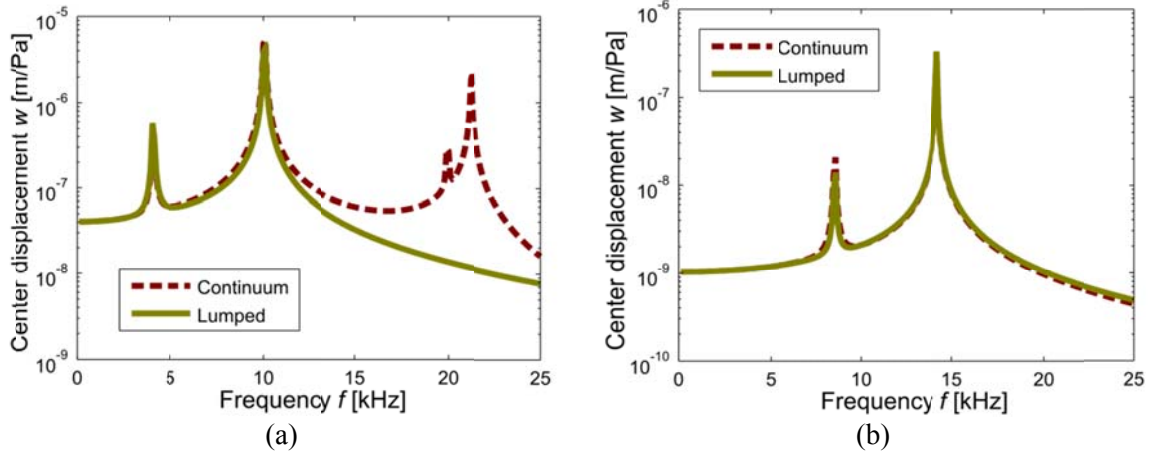


Figure 3-13: Comparison of center displacement spectra of a fly-ear inspired directional microphone using the continuum mechanics model and the lumped model. (a) Without considering the effects of air gap. (b) Effects of air gap included. Incident azimuth is  $90^\circ$ . The two diaphragms have the same responses.

Figure 3-14 compares one of the directional cues  $mIPD$  for the same two scenarios. As noted previously, since the two diaphragms have same absolute displacements, the other directional cue  $mIID$  is equal to zero. The results shows the results from both lumped model and continuum model are consistent.

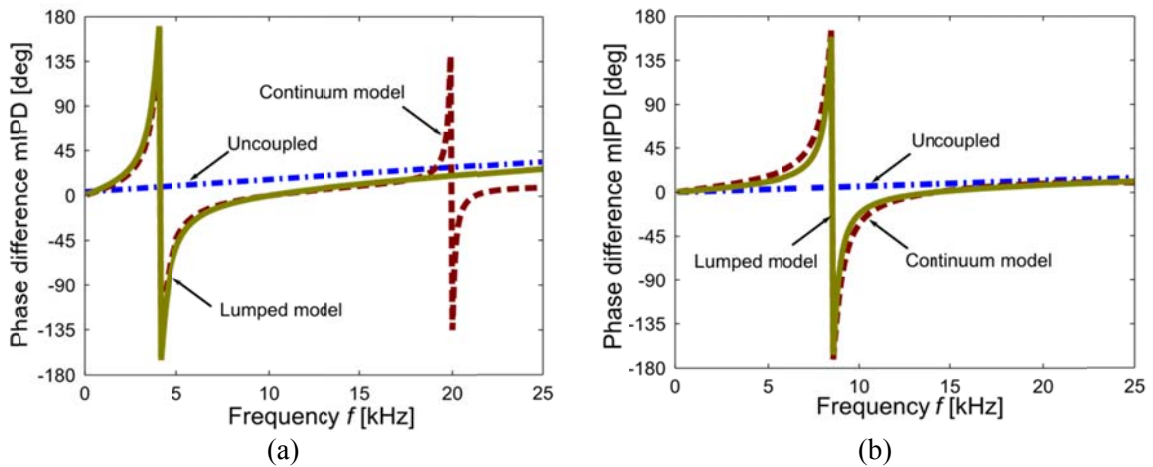


Figure 3-14: Comparison of phase difference  $mIPD$  of a fly-ear inspired directional microphone obtained by using the continuum mechanics model and the lumped model. (a) Without air gap. (b) With the air gap included.

The slight discrepancy between the continuum model and the lumped model can be attributed to several factors. The main cause is that in the lumped model, the bridge is assumed to be massless. The mass of the bridge should be added to the diaphragm based on the equivalence of kinetic energy. The equivalent added mass can be calculated by

$$\int_0^1 \frac{1}{2} \cdot \rho b h_b L dx \cdot U_b^2(x) = \frac{1}{2} M_e U_b^2(x=1). \quad (3-135)$$

From the above equation, one can obtain the equivalent mass  $M_e$

$$M_e = \varepsilon M_b, \quad (3-136)$$

where

$$\varepsilon = \frac{\int_0^1 U_b^2(x) dx}{U_b^2(x=1)}, \quad (3-137)$$

and  $M_b = \rho b h_b L$ . Apparently, the equivalent mass varies for different modes of the bridge. For example, if there is no axial loading on the beam,  $\varepsilon$  is equal to 33% for the first mode, and 25% for the second mode. This is different from the continuum mechanics model where no such equivalence is needed. The results show that the lumped 2DOF model, as simplified as it is, captures the essential dynamics of the coupled system.

### 3.7 Parametric studies

To understand how the structural parameters of the fly-ear inspired directional microphone affect its performance, the following parameters should be investigated:



- 1) **Separation-to-wavelength ratio.** This ratio is predetermined by the working frequency and desired size.
- 2) **Damping ratios.** The damping characteristics can be tuned by adding a plate with perforated holes in the back chamber.
- 3) **Natural frequencies.** The frequencies for the rocking and bending modes are important in determining the performance characteristics of the coupled system.

However, since the overall effects of these parameters are similar to what has been studied using the 2-DOF model in Chapter 2, the parametric studies about these parameters are omitted here to avoid being repetitive. In the following subsections, parametric studies will be carried out to study the effects of the several other key structural parameters on the natural frequencies of the mechanically coupled system. One parameter is the air gap height, which affects the diaphragm's effective stiffness. The structural parameters of the bridge that can change the effective stiffness and mass of the bridge relative to the diaphragm also need to be investigated.

Given all the parameters for the circular plate and air gap, the effects of the coupling bridge can be studied by varying its material parameters and geometric dimensions. For the material parameters, changing the Young's modulus  $E_b$  and the density  $\rho_b$  will simply change the stiffness and the mass of the bridge, respectively. On the other hand, the effects of geometric parameters are more complicated, since they change the stiffness and mass simultaneously. For example, the mass of the beam is linearly proportional to the bridge's width  $b$  and thickness  $h_b$ . The stiffness of the beam, as described by Equation

(3-45), is proportional to  $h_b^3$ , but independent of  $b$ . Also, the beam width does affect the coupling force between the plate and the bridge, as indicated in Equation (3-122).

For simplicity, a hypothetical material will be created with modified  $E_b$  and  $\rho_b$ , which is used to study the effects of changing the bridge's stiffness and mass separately.

### **3.7.1 Air gap height**

As previously discussed in the study on a single circular clamped diaphragm, the air gap needs to be considered to obtain accurate natural frequencies and frequency response of the system. The same conclusion can be drawn here for the directional microphone with mechanically coupled diaphragms. In the air gap range as shown in Figure 3-15(a), a shorter air gap increases the stiffness of the diaphragm, rendering a higher rocking and bending mode frequencies. However, the ratio of between the two frequencies decreases with reduced air gap height, as shown in Figure 3-15(b).

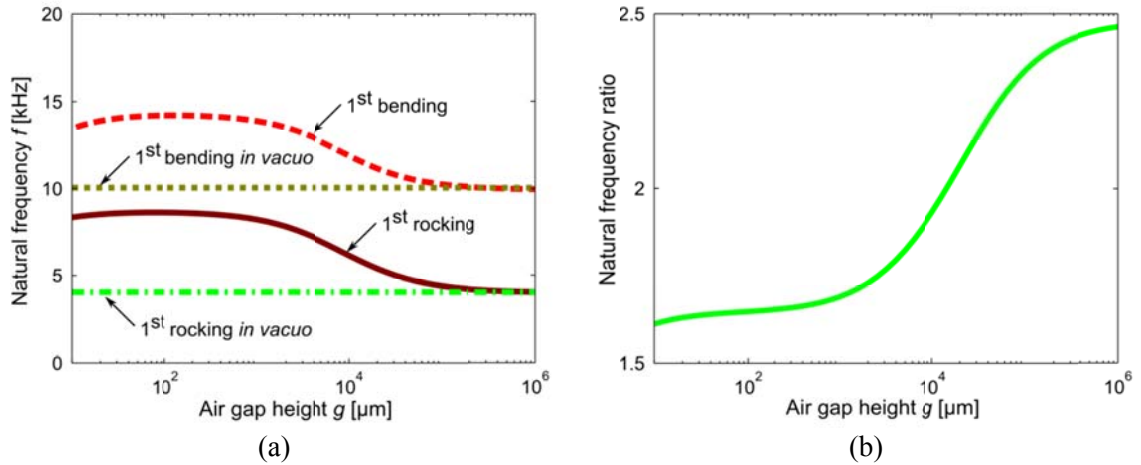


Figure 3-15: The effects of air gap on the natural frequencies of the fly-ear inspired directional microphone. (a) The natural frequencies of the first rocking mode and first bending mode as a function of the air gap height. (b) The ratio of the two natural frequencies.

### 3.7.2 Young's modulus of the coupling bridge

A hypothetical material is created with a modified Young's modulus  $E_b'$ , ranging from 0.1 times to 100 times of the original value  $E_b$ . As shown in Figure 3-16(a), increasing the bridge stiffness will increase the natural frequencies of the rocking and bending modes. However, they cannot be increased to any arbitrary number. Rather, the natural frequencies saturate when  $E_b'$  is larger than a critical value. Another relevant conclusion can be drawn from Figure 3-16(b) is that the natural frequency ratio of the first bending mode to the first rocking mode cannot be increased to an arbitrary high value as indicated by the lumped model.

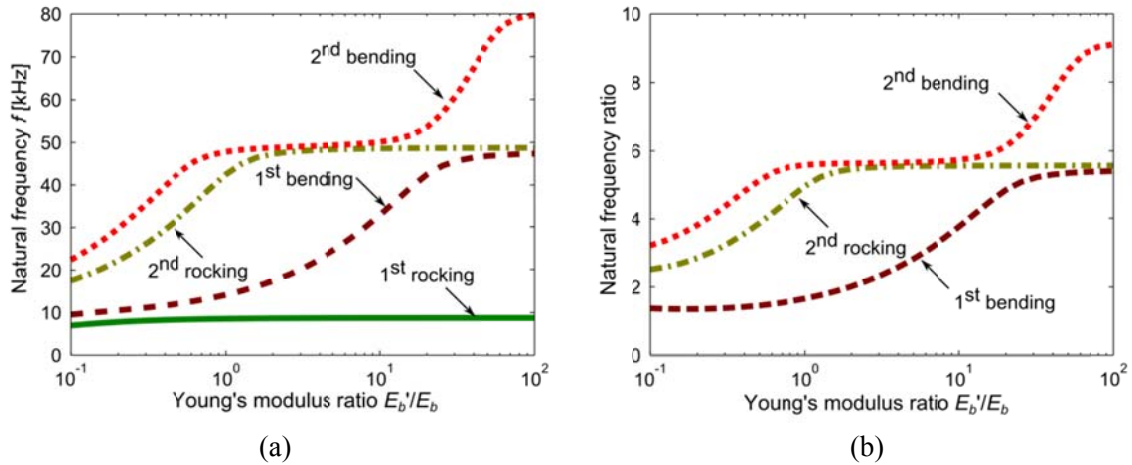


Figure 3-16: The effects of the Young's modulus of the diaphragm on the natural frequencies of the fly-ear inspired directional microphone. (a) The natural frequencies of the first and second rocking modes and bending modes as a function of Young's modulus ratio. (b) The ratio of natural frequencies to the first rocking mode natural frequency.

### 3.7.3 Density of the coupling bridge

A hypothetical material is created with modified density  $\rho_b'$ , ranging from 0.1 times to 100 times of the original value  $\rho_b$ . As shown in Figure 3-17(a), increasing the bridge density will decrease the natural frequencies of the rocking and bending modes. Although following a similar downward trend, the variations of the natural frequencies have different shapes. In the range chosen in Figure 3-17(b), the natural frequency ratio of the first bending mode to the first rocking mode stays almost constant same as the density changes.

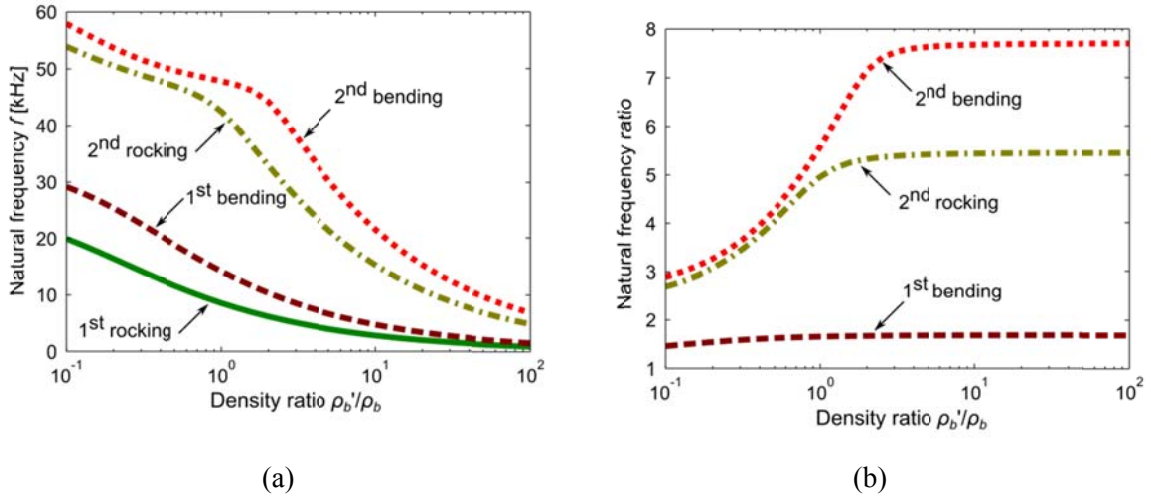


Figure 3-17: The effects of the diaphragm's density on the natural frequencies of the fly-ear inspired directional microphone. (a) The natural frequencies of the first and second rocking modes and bending modes as a function of the density ratio. (b) The ratio of natural frequencies to the first rocking mode frequency.

### 3.8 Summary

Based on the mechanically coupling mechanism found in the fly, a bio-inspired directional microphone design is proposed, which consists of two circular clamped diaphragms connected by a coupling bridge. A continuum mechanics model is developed to achieve a fundamental understanding of the structural dynamics and the performance of the coupled system. This model can capture two types of essential coupling of the system: one for the mechanical coupling of the two diaphragms through a beam and the other for each diaphragm coupled through an air gap. The developed model is validated with a finite element mode in ANSYS, and the equivalence between the continuum mechanics model and the lumped two degrees-of-freedom model is established. Parametric studies are carried out to study the effects of key structural parameters. The developed continuum mechanics model is necessary for the sensor development to be

discussed in the next chapter, which cannot be carried out by using the lumped 2-DOF model discussed in the previous chapter.

## **Chapter 4 Fly-Ear Inspired Directional Microphones: Sensor System Development and Experimental Studies**

### **4.1 Overview of sensor system development**

As illustrated in Figure 4-1, the sensor system development consists of two parts, one for the mechanical components, and the other for the detection system. The mechanical part has a rigid substrate with two flexible diaphragms. A bridge connects the two diaphragm centers so that only the axisymmetric modes of the diaphragm transmit the coupling force via the connecting joints. The bridge is free to rotate about the pivot in the middle. To detect the minute diaphragm response, a detection system with high sensitivity and large signal-to-noise ratio (SNR) is needed. Here, a fiber optic interferometric system is used to detect the vibrations at the diaphragm centers where the deflection is maximal. For each diaphragm, an optical fiber is inserted through the back of the substrate and aligned with the diaphragm center.

In the next section (Section 4.2), the development of optical detection system will be detailed. A large-scale proof-of-concept directional microphone is developed in Section 4.3 to validate the mechanical coupling mechanism and the overall system development. Then, a fly-ear sized sensor is demonstrated to achieve the dual optimality characteristic at 8 kHz (Section 4.4). Finally, to best use this sensor for sound source localization, a

robotic platform with a control scheme inspired by the fly's localization/lateralization scheme is developed in Section 4.5, followed by a brief summary in Section 4.6.

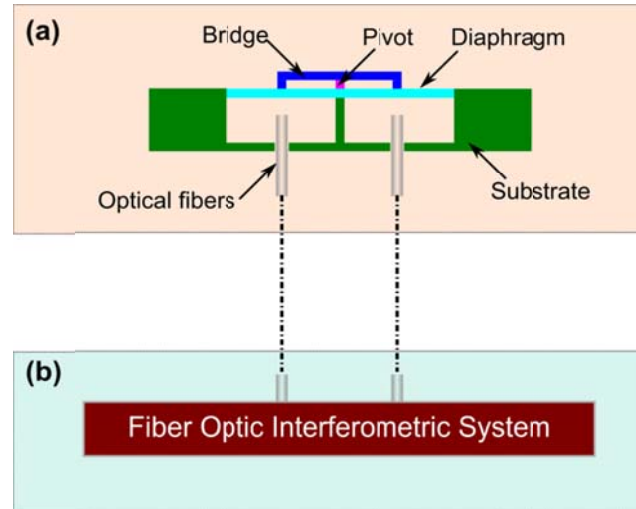


Figure 4-1: Overview of the sensor system development. (a) Mechanical part which consists of two diaphragms coupled by a bridge. (b) Detection system where a fiber optic interferometric detection system is used.

## 4.2 Development of optical detection system

Capacitive detection technique is the most widely employed sensing method for miniature microphones. It has better pressure sensitivity and less temperature sensitivity over piezo-resistive microphones. Drawbacks of capacitive microphones include the excess signal loss from parasitic capacitance and the requirement of expensive and bulky high-impedance preamps at the sensor head. In addition, when the size is reduced, capacitive microphones are very susceptible to the mechanical noise due to molecular agitation, and thus a tradeoff has to be made between the sensitivity and the noise floor.



Microphones based on optical detection techniques possess several advantages over conventional capacitive technique, which are preferred in some applications (Bilaniuk, 1997). In addition to the absence of parasitic capacitance, the advantages of optical microphones include high pressure sensitivity, high SNR, immunity to electromagnetic interference, and safety in hazardous and explosive environments. By incorporating fiber optic components into the optic detection method, a versatile and robust system can be constructed, which has further advantages of light weight, capability of remote operation, and multiplexibility.

As one of the optical detection methods in microphones, fiber optic interferometers (FOI) offer high sensitivity by measuring the change of the optical phase induced by the optical path difference (OPD) change. Other advantages of fiber optic interferometers include immunity to electromagnetic interference (EMI), robustness in hazardous environments, capability of remote operation (Grattan & Meggitt, 2000; Hariharan, 2003). The most commonly used FOI sensors are those based on two-beam interferometry, such as the Mach-Zehnder, Fabry-Perot, and Michelson interferometers, as shown in Figure 4-2.

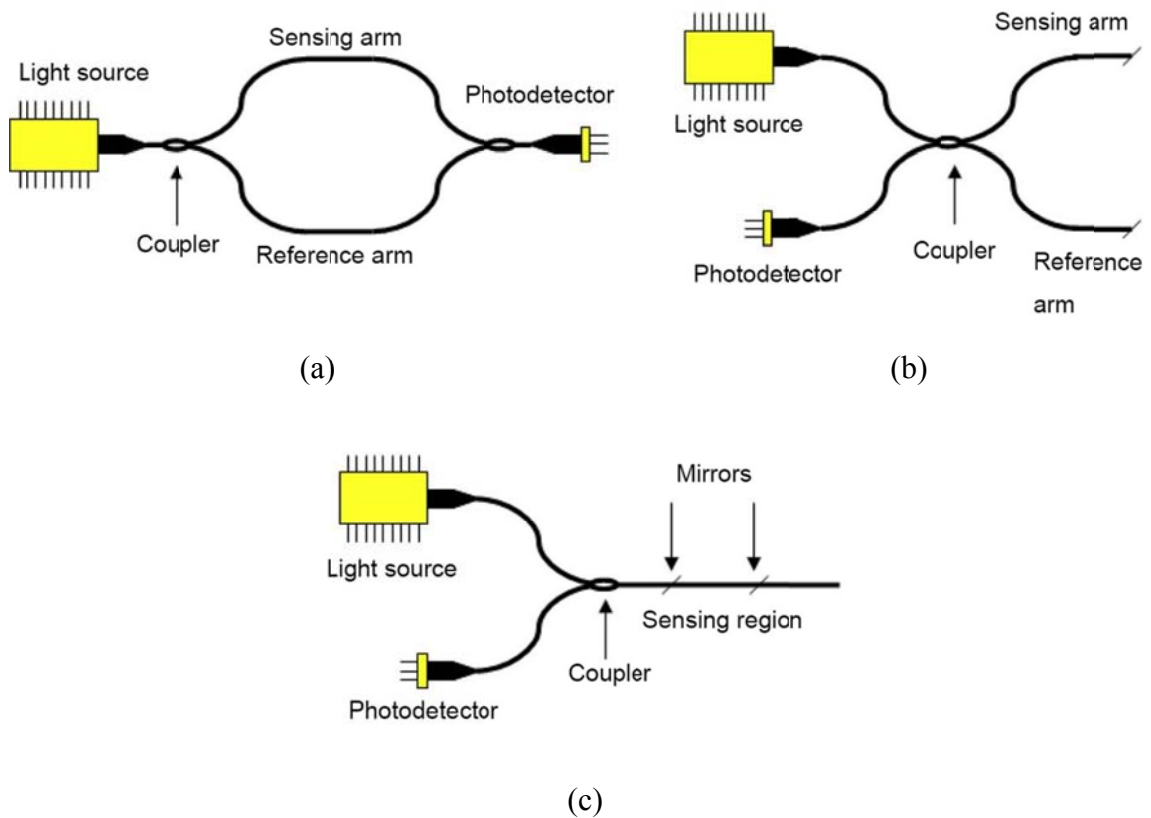


Figure 4-2: Schematics of two beam interferometers: (a) Mach-Zehnder, (b) Fabry-Perot, and (c) Michelson. (Wild & Hinckley, 2008)

The light from the light source, ideally a single frequency laser in a conventional interferometer configuration, is split to two beams on the reference arm and the sensing arm. The OPD between these two beams results in an intensity change of the interferometer output  $I$ , which has a sinusoidal form given by

$$I = I_0 (1 + V \cos(\phi_s - \phi_r)), \quad (4-1)$$

where  $I_0$  is the dc component,  $\phi_s$ ,  $\phi_r$  are the optical phase of the sensing and reference arms, and  $V$  is the visibility of the interference given by

$$V = \frac{I_{\max} - I_{\min}}{I_{\max} + I_{\min}}, \quad (4-2)$$

where  $I_{\max}$  and  $I_{\min}$  are the maximum and minimum values of  $I$ . The highest sensitivity is achieved when the interferometer is operated at the quadrature points, i.e.

$$\Delta\phi = \phi_r - \phi_s = \frac{2m-1}{4}\lambda, \quad (4-3)$$

where  $m = 0, \pm 1, \pm 2, \dots$ , and  $\lambda$  is the wavelength of light.

In a low coherence fiber-optic interferometry (LCFOI) configuration, a low coherent broadband light source is used (Grattan & Meggitt, 2000; Miao Yu, 2002). When using time domain signal processing, the system is usually arranged to have two interferometers: one sensing interferometer and one reference interferometer (also called read-out interferometer). The schematic of the LCFOI is shown in Figure 4-3. In order to obtain temporally incoherent light after the light passes the sensing interferometer, the OPD in the sensing interferometer  $L_s$  should be arranged to be greater than the coherence length  $L_c$  of the light source. When the OPDs satisfy the following conditions:

$$L_r \approx L_s \text{ and } |L_r - L_s| \ll L_c, \quad (4-4)$$

the light intensity received at the photo detector can be approximated by

$$I \approx I_{dc} + I_{ac} \cos k_0 (L_s - L_r). \quad (4-5)$$

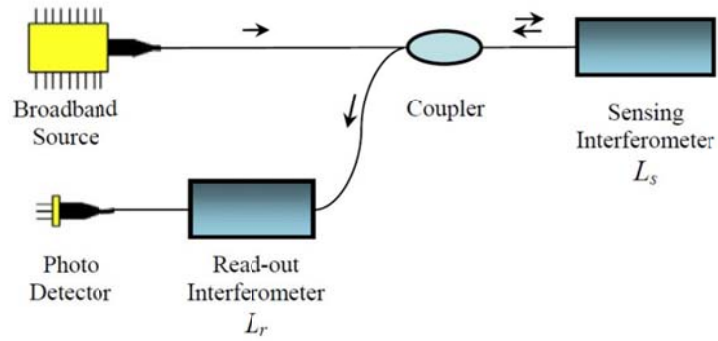


Figure 4-3: Basic configuration of low coherence fiber optic interferometric system

Different from the conventional FOI, LCFOI measures the differential optical phase change between a sensing interferometer and a readout interferometer. This technique can not only take advantage of the features of the conventional optical interferometer based sensors, but provide a much higher signal-to-noise ratio, lower drift, and more reliable sensing data, and allows for a large bandwidth, large dynamic range, and a much more simplified phase demodulation scheme.

Because of these characteristics of LCFOI, an optical detection system without phase demodulation based on LCFOI is developed to detect the vibrations of the two diaphragms for the bio-inspired directional microphone. As illustrated in Figure 4-4, each diaphragm and its corresponding fiber tip forms a Fabry-Pérot (FP) interferometer. Broadband light from a super-luminescent light emitting diode (SLD) (O/E Land Inc, OELED-100) is first sent via a 3dB optical coupler to two other couplers. At the output of each coupler, the light beam is directed to the FP sensor. The reflected light from each FP sensor is then coupled back to a tunable Fabry-Pérot filter (Micro Optics, FFP-TF2) and finally to a photo detector (New Focus, Model 2011). The outputs from the

photodetectors are then acquired through a data acquisition board (DAQ) (National Instruments, USB-6259) for post-processing.

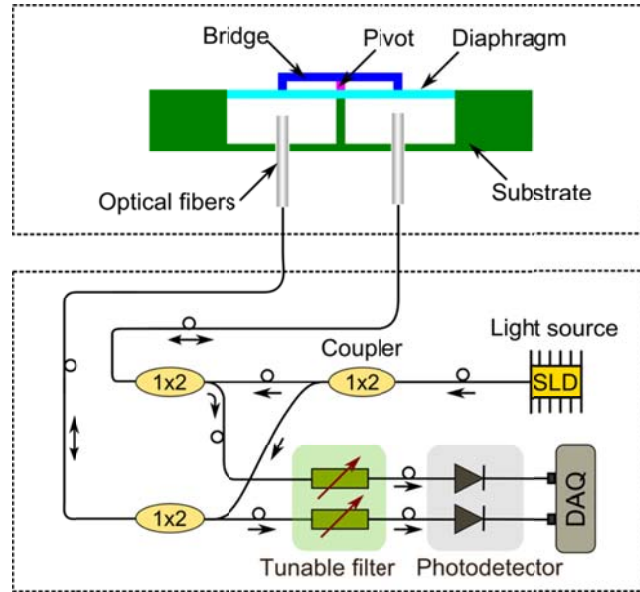


Figure 4-4: schematic of a low-coherence fiber optic interferometric system for the fly-ear inspired directional microphone.

In the experimental setup, the maximum sensitivity is achieved when the initial OPD is in the vicinity of quadrature points; that is,

$$L_{si} - L_{ri} = (2m - 1) \frac{1}{4} \lambda, \quad (4-6)$$

where  $m = 0, \pm 1, \pm 2, \dots$ . To ensure the detection system working at the quadrature points, bias voltages are applied to the tunable filters, which can compensate the cavity length deviation in the fabrication process and the post-fabrication drift.

### 4.3 Large-scale proof-of-concept directional microphone

To mimic the fly ear and provide a proof-of-concept prototype of the proposed design and model, a large-scale directional microphone is developed. The distance between diaphragms centers is 25.4 mm. The integrated microphone device is shown in Figure 4-5.

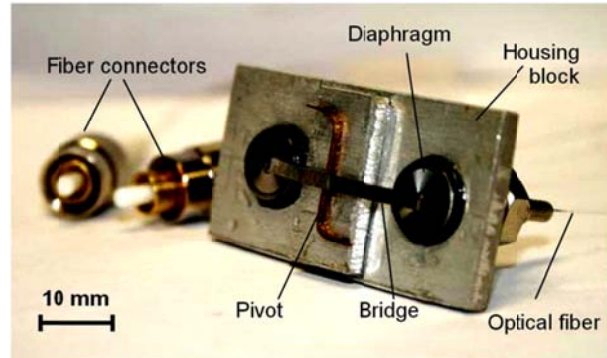


Figure 4-5: Photograph of large-scale bio-inspired directional microphone. The separation between the two diaphragm centers is 25.4 mm (one inch).

The fabrication starts with the Mylar diaphragm, disassembled from a commercially available microphone cartridge (CUI Inc, Model CMP-5247TF-K). The peripheral boundary of the diaphragms is bonded to the end face of a plastic tube by epoxy. A fiber optic connector ferrule is attached to the tube by thread connection. Then, two of these tubes and a Z-shaped pivot (metal sheet) are glued to an aluminum housing block. After that, optical fibers are inserted from the back side, and the distance of the Fabry-Perot cavities are adjusted based on the interference fringe obtained with an optical spectrum analyzer (OSA). When the cavity length of the sensor is found to match that of the tunable filter, a room cured optic connector epoxy is used to fix the cavity length. This makes a conventional microphone pair, namely a directional microphone without mechanical coupling.

Next, the uncoupled directional microphone is assembled onto a manual rotational stage. Using the low coherence fiber optic interferometer described in Section 4.1, the response of the two uncoupled diaphragms subject to a sound field can be measured, which can be used to obtain the characteristics of the diaphragm alone.

Based on the continuum mechanics model described in Chapter 3, the selection of an appropriate material and geometry for the coupling bridge is made. Here, a steel beam is used as the coupling bridge. The last step is to connect the diaphragm centers with the coupling bridge to finish the coupled microphone, which can be placed on the rotation stage to study its performance for sound source localization.

As only one tunable filter was available at the time of the experimental measurement, the detection system was different from that illustrated in Figure 4-4. In the modified LCFOI system shown in Figure 4-6, the cavity lengths of both Fabry-Perot interferometer (between fiber tip and diaphragm) need to be approximately equal to the cavity length of the tunable filter. In order for both to work at the quadrature points, the difference of cavity lengths of two Fabry-Perot interferometers needs to be an integer multiple of the light source's center wavelength. This poses great challenges to the distance control in the fabrication process. For example, the amount of epoxy needs to be similar and the curing needs to be synchronized. The difference can be slightly adjusted by manually fine-tuning the thread connecting the ferrule and the plastic tube.

The design parameters of the fabricated directional microphone are listed in Table 4-1. The separation-to-wavelength ratio is chosen to be about 1/10. This ratio will be bigger if the full width of the substrate is used instead of the distance of diaphragms in the

calculation. Since the sound field is disturbed due to diffraction, it is expected that errors will occur in the measurement of the  $mIID$ . Therefore, in the experiments,  $mIPD$  or  $mITD$  is used as the only directional cue to study the performance of the microphones.

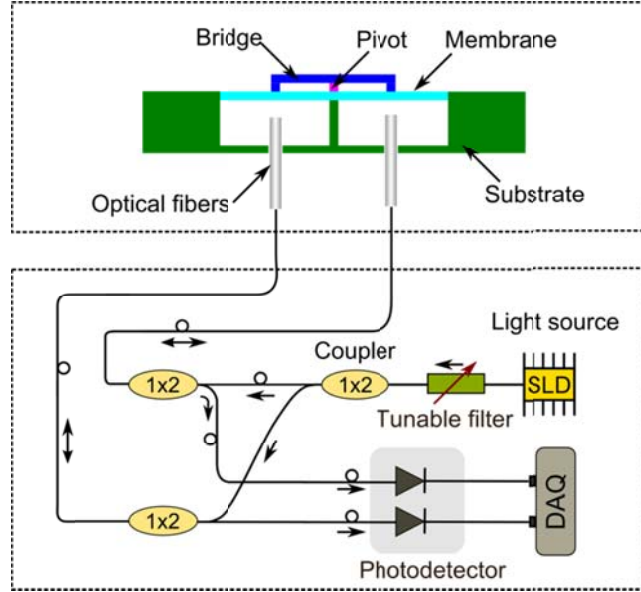


Figure 4-6: Low-coherence fiber optic interferometer system using one tunable filter for the large-scale bio-inspired directional microphone.

Table 4-1: Parameters of the large-scale directional microphone

Parameter	Value
Separation of diaphragm centers $d$	25.4 mm
Diaphragm thickness $h_d$	22 $\mu\text{m}$
Diaphragm radius $R$	3.5 mm
Bridge thickness $h_b$	0.10 mm
Bridge width $b$	1.9 mm
Mass Ratio $\chi_m$	16.4
Stiffness Ratio $\chi_k$	6.4
Damping Factors $\xi_d, \xi_b$	0.1, 0.1
First natural frequency $f_1$	1.3 kHz
Second natural frequency $f_2$	2.2 kHz
Separation-to-Wavelength Ratio $\chi_\lambda$ at $f_1$	1/10.4



First, a band-limited white noise is generated from a speaker placed 0.5 m away from the microphone. The obtained microphone response spectrum exhibits multiple peaks. The natural frequencies corresponding to the first two peaks are 1.3 kHz and 2.2 kHz, as listed in Table 4-1.

Next, a pure tone at various frequencies is used to characterize the microphone's response to different incident angles.  $mITD$  as a function of incident azimuths is shown in Figure 4-7(a) when the excitation frequency is 1100 Hz. The insets illustrate two experimentally obtained waveforms at the azimuth angles of  $20^\circ$  and  $60^\circ$ . The corresponding  $mIPD$  can be observed to change from  $47^\circ$  to  $118^\circ$ , corresponding to a  $mITD$  change from  $120 \mu\text{s}$  to  $297 \mu\text{s}$ . When compared with the uncoupled case,  $mITD$  is amplified more than 4.4 times at the  $90^\circ$  azimuth. The experimental data compare well with the simulation results obtained based on the continuum mechanics model with a plane wave assumption. According to the fitted curve of the experimental data, the directional sensitivity reaches a peak at  $6.5 \mu\text{s}/\text{deg}$  and stays almost constant within  $\pm 30^\circ$  azimuth.

The frequency response of  $mITD$  obtained at a constant azimuth of  $40^\circ$  is plotted in Figure 4-7(b). Below the first rocking natural frequency of 1.29 kHz,  $mITD$  goes up as the excitation frequency is increased. In the vicinity of the rocking mode natural frequency,  $mITD$  experiences a sudden sign change. Although the absolute value of  $mITD$  peaks at this frequency region, the directional sensitivity is extremely small at a large azimuth (e.g, when the excitation frequency is 1.3 kHz, as shown in the inset). Further increase of the frequency causes a decrease of  $mITD$ . In the vicinity of the bending mode

natural frequency of 2.2 kHz, the absolute value of  $mITD$  reaches almost 0. For comparison, ITD of the uncoupled case (75  $\mu\text{s}$ ) is also shown in Figure 4-7 (b).

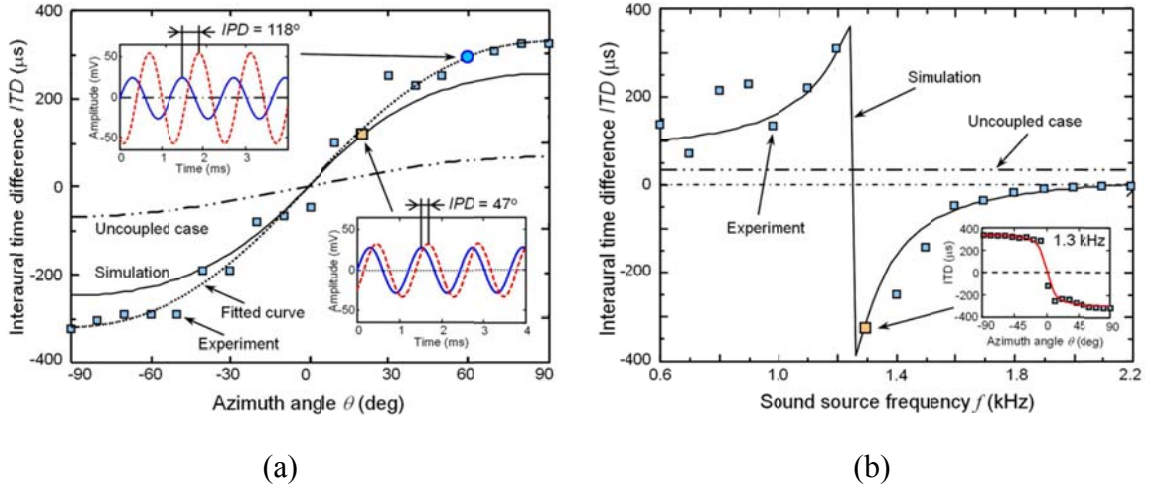


Figure 4-7: Directional cues of large-scale prototype. (a)  $mITD$  versus incident angle for 1.1 kHz; (b)  $mITD$  in the frequency domain when incident angle is fixed at  $40^\circ$ . (Liu, Yu, & Zhang, 2008)

## 4.4 Development of a micro-scaled sensor mimicking the fly-ear's dual optimality characteristic

### 4.4.1 Sensor design based on dual-optimality

Since the dual-optimality property enables the fly to accurately locate its host crickets despite of its limited signal processing capability, it is important to note that the dual-optimality characteristic is not limited to the fly ear's size or the cricket's calling song frequency. Rather, for any damping scenarios (given damping ratio  $\xi_1$  and  $\xi_2$ ), the two natural frequencies can be calculated as a function of separation-to-wavelength ratio  $\chi$  that ensure the designed system the dual-optimality characteristic at its desired working frequency  $f$ . For example, when  $\xi_1 = 0.18$ ,  $\xi_2 = 0.05$  (the damping ratios for the prototype introduced later), the optimal design curves are shown in Figure 4-9(a), from which the

two natural frequencies for the rocking and bending modes can be obtained for any given separation-to-wavelength ratio (calculated by using the working frequency and desired size). Three representative systems (marked as A, B, and C) that are optimized for working at 2 kHz, 8 kHz, and 12 kHz are shown for an interaural separation of 1.2 mm. The calculated two natural frequencies are 2.36 kHz and 9.19 kHz (system A), 9.47 kHz and 20.23 kHz (system B), and 14.23 kHz and 26.20 kHz (system C). The spectra of  $ADS$  and  $NL$  in Figure 4-9(b) confirm the dual-optimality characteristic of these three systems. As a result, the spatial distribution of  $DS$  has a flat region within the linear range (Figure 4-9(c)), which is also higher than those obtained at other frequencies, as shown in Figure 4-9(d) for system B.

As shown in Figure 4-9, the proposed miniature fly-ear inspired directional microphone consists of four layers, numbered 1 to 4 in the plot. Two clamped circular diaphragms and a coupling bridge are on the front plate layer (Layer 1). A back chamber is formed by Layer 2-4 with perforated holes in the middle layer, which are designed to tune the system's damping characteristics. Four through holes are made at the corners of all four layers to facilitate the alignment during the bonding process.

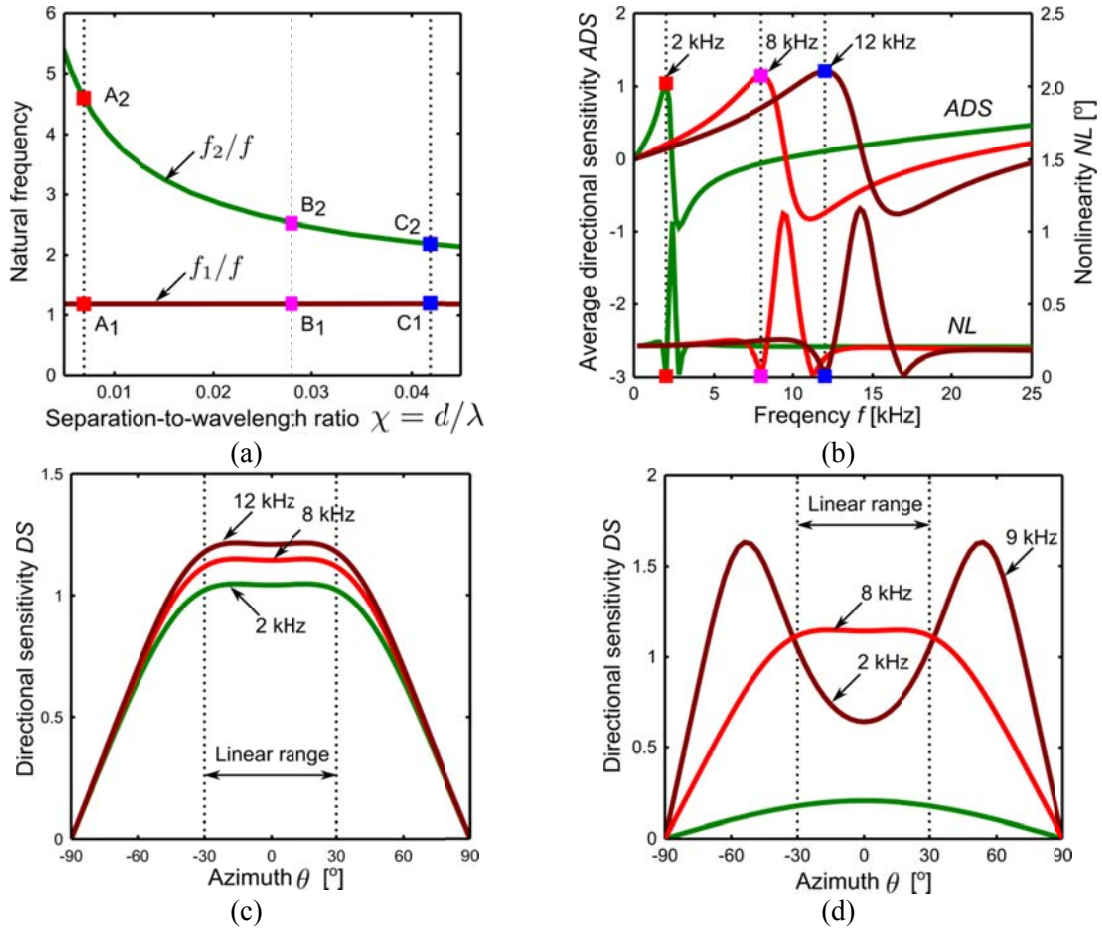


Figure 4-8: Design guideline based on the fly ear's dual-optimality. (a) Optimal natural frequencies for designing fly-ear like systems (damping ratio  $\xi_1 = 0.18$ ,  $\xi_2 = 0.05$ ). With an interaural separation of 1.2 mm, three examples are marked on this plot for working frequencies at 2 kHz, 8 kHz, and 12 kHz, respectively, (b) Spectra of average directional sensitivity (*ADS*) and nonlinearity (*NL*) for the three examples in (a). (c) Spatial distribution of directional sensitivity (*DS*) for the three examples in (a) at their respective optimal working frequencies. (d) Spatial distribution of *DS* for the representative system B in (a) at three different frequencies.

The center-to-center separation is chosen to be equal to that of the fly ear (i.e., 1.2 mm). Polysilicon is chosen as the material for the diaphragm with a diameter of 1.1 mm and thickness of 0.5  $\mu\text{m}$ . Alternating layers of silicon dioxide and silicon nitride are used for the bridge that is 300  $\mu\text{m}$  wide and 3.2  $\mu\text{m}$  thick (2.6  $\mu\text{m}$  of dioxide and 0.6  $\mu\text{m}$  of nitride). The layer with perforated holes has eight 60  $\mu\text{m}$  diameter through holes for damping

tuning and one 250  $\mu\text{m}$  diameter hole for optical fiber guiding under each diaphragm. The thickness of all four layers is 250  $\mu\text{m}$ . The above dimensions are chosen based on the mechanics model of the sensor discussed in Chapter 3.

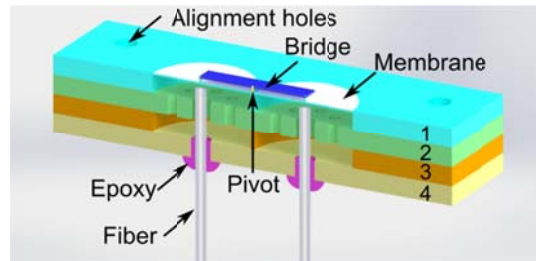


Figure 4-9: Design of a miniature MEMS directional microphone inspired by the fly ear. It consists of four layers, device layer (Layer 1), perforated holes plate (Layer 2), back chamber (Layer 3), and back plate (Layer 4).

#### 4.4.2 Sensor fabrication

The fabrication process for the front layer is illustrated in Figure 4-10. Starting from a blank double side polished silicon wafer, a 1  $\mu\text{m}$  thick silicon dioxide layer is deposited by plasma enhanced chemical vapor deposition (PECVD) to serve as an etch stop for the upcoming back-etching step. The  $\text{SiO}_2$  is annealed in nitrogen at 700°C for 60s to densify the film and drive off excess trapped hydrogen. Then, a 0.5 $\mu\text{m}$  thick layer of polysilicon is sputtered on top of the  $\text{SiO}_2$  as the diaphragm material (Figure 4-10(a)). These two deposition steps can be replaced by using a customized silicon-on-insulator (SOI) wafer. Next, four holes are etched through the top silicon layer by deep reactive ion etching (DRIE) until reaching the  $\text{SiO}_2$  etch stop layer, forming part of the alignment through holes (Figure 4-10(b)). Then, a photoresist sacrificial layer is deposited and patterned on top of the polysilicon, and hard baked at 175°C (Figure 4-10(c)), defining the shape of

the joints between the diaphragm and the bridge. This is followed by PECVD of the coupling beam, which consists of alternating layers  $\text{SiO}_2$  and  $\text{Si}_3\text{N}_4$  (Figure 4-10(d)). The sequence is 0.8  $\mu\text{m}$  of oxide followed by 0.2  $\mu\text{m}$  nitride, which is repeated three times and capped by a final 0.2  $\mu\text{m}$  of oxide on the top. The total thickness of the beam is 3.2  $\mu\text{m}$ , including 2600Å  $\text{SiO}_2$  and 600Å  $\text{Si}_3\text{N}_4$ . The temperature is controlled at 175°C to avoid burning the photoresist. The coupling beam is patterned with a second layer of photoresist and etched by reactive ion etching (RIE), shown in Figure 4-10(e). A photoresist layer is patterned on the backside of the wafer to define the diaphragm geometry. Then, the silicon wafer is etched by deep reactive ion etching (DRIE) until reaching the  $\text{SiO}_2$  etch stop layer. Using the same mask, the  $\text{SiO}_2$  layer is removed also by RIE (Figure 4-10(f)). The process is completed after removing the sacrificial photoresist with an isotropic oxygen plasma ash process (Figure 4-10(g)).

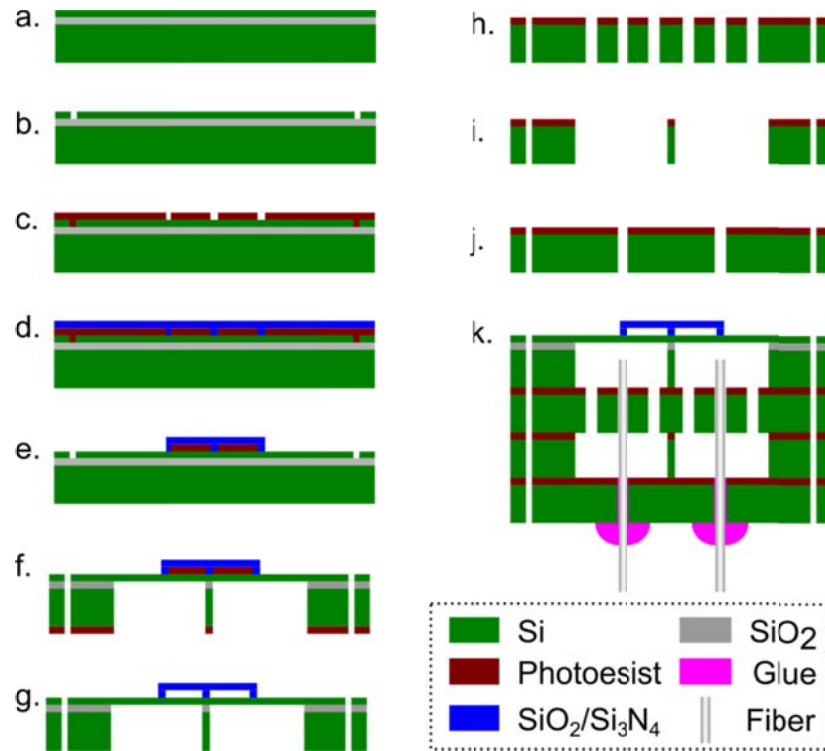


Figure 4-10: Fabrication and assembly process of the bio-inspired sensor. (a)-(g) Fabrication process for the front plate layer. (h)-(j) Fabrication process for the remaining three layers: damping layer, perforated holes layer, and back plate layer. (k) The assembled device after thermally bonding the four layers, inserting the fibers to the desired positions, and gluing them to the back plate layer using ultraviolet cured epoxy.

For the other three layers, a photo-resist layer is patterned on one surface of the wafer, followed by a DRIE step to make the through holes, shown in Figure 4-10(h-j). The residual photo-resist remains on the wafers. The four layers are stacked together using four optical fibers running through the through-holes on the four corners. The inter-layer photo-resist glues all the layers together on a 300°C oven for 3 minutes. Finally, two optical fibers are inserted into the two center holes underneath the diaphragm till the gap between the fiber tip and the diaphragm matches with the tunable filter, after which an ultraviolet-cured epoxy is used to seal the gap and fix the fiber to the wafers, as shown in

Figure 4-10(g). The completely assembled sensor device is depicted in Figure 4-11 along with a house fly.



Figure 4-11: A fabricated MEMS directional microphone placed next to a house fly

The MEMS fabrication process is carried out in the clean room of the US Army Research Lab (Adelphi, MD) by Luke Currano, Danny Gee, and Tristan Helms.

#### **4.4.3 Experiment study of the MEMS sensor**

As shown in Figure 4-12, the MEMS device is mounted on the tip of a small aluminum rod (diameter of 0.25”) of a home-made fixture on a motorized rotational stage (Newport, URS75BPP) connected to a motion controller (Newport, ESP 300). A pure tone or chirp sound of various frequencies is played through a speaker (ESS Heil air motion transformer). The movement of the source is simulated by another motorized rotational stage under the stage mounting the sensor (the speaker’s position is fixed). The responses from the two diaphragms are acquired for every 2.5 degrees in the linear range and every 5 degrees otherwise. For each frequency, this process is repeated 5 times to get the average values. Signals received from the photodetectors are sampled at a rate of 500 kHz for each channel.



Time delay is calculated by finding the maximum of the cross-correlation of two channels and converted to phase difference  $mIPD$ . For the sampling rate used in the experiment (500 kHz), the time resolution of the cross-correlation is  $2 \mu\text{s}$  (note that a center-to-center distance of 1.2 mm only renders a time difference of up to  $3.53 \mu\text{s}$ ). For a sound frequency of 8 kHz, a time delay of  $2 \mu\text{s}$  is equivalent to a phase difference of  $5.76^\circ$ . To improve the resolution, a second order polynomial is used for the curve fitting around the center peak of the cross-correlation (Benesty, Chen, & Huang, 2004).

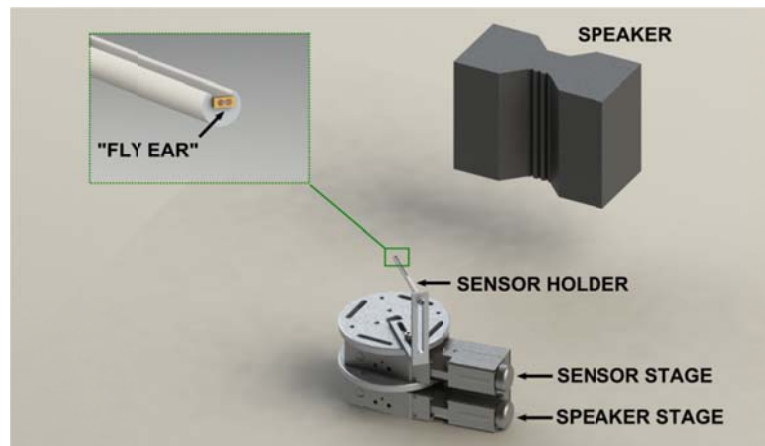


Figure 4-12: Experimental setup to characterize the fabricated miniature directional microphone inspired by the fly ear

To characterize the device performance, the directional cue  $mIPD$  is obtained for different sound frequencies and incident azimuths in an anechoic chamber, as shown in Figure 4-13(a). Least square fitting is used to obtain the natural frequencies and damping ratios in the 2-DOF model. The damping ratios are fitted to be  $\xi_1 = 0.18$  and  $\xi_2 = 0.05$ . The rocking mode and bending mode natural frequencies of the device are determined to be 9.75 kHz and 22.0 kHz, respectively, which are close to the designed optimal values of 9.47 kHz and 20.2 kHz. Overall, as illustrated in as shown in Figure 4-13(a-b), the

experimental results compare well with the results obtained on the basis of the 2-DOF model by using the two designed natural frequencies and characterized damping ratios. The mode shapes are also verified by using Doppler scanning vibrometer (Polytec MSA-500), as shown in Figure 4-14.

The natural frequencies predicted by the continuum mechanics model are 6.91 kHz for the rocking mode and 12.40 kHz for the bending mode, based on the assumption of zero in-plane force in the diaphragm and zero axial force on the bridge. The discrepancy is believed to be due to the thermal residual stress in the micro-fabricated device. By fitting the continuum model with the experimentally calibrated natural frequencies, the tension parameters for the diaphragm and the bridge can be determined as  $\chi_{tp} = 100$  and  $\chi_{tb} = 6.9$ . The corresponding residual stresses are calculated to be 1.24 MPa for the diaphragm, and 3.85 MPa for the bridge (both of them are tensile stress).

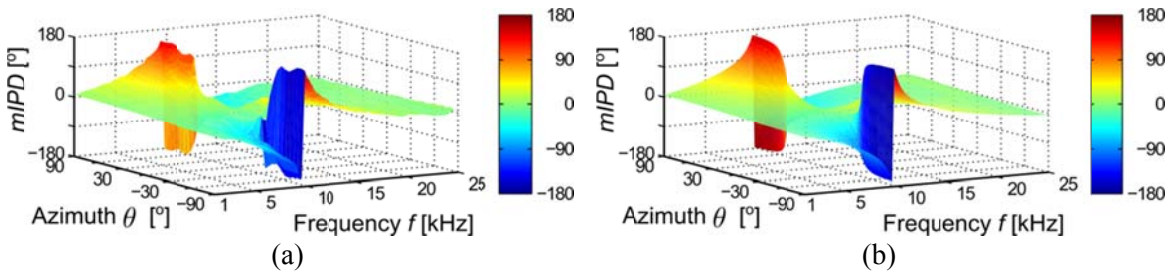


Figure 4-13: Phase difference  $mIPD$  for fabricated directional microphone inspired by the fly ear. (a) Experiment. (b) Simulation.



Figure 4-14: Mode shapes obtained by laser Doppler vibrometer measurement for the miniature directional microphone inspired by the fly ear. (a) Rocking mode (9.8 kHz). (b) Bending mode (22.0 kHz).

Further,  $ADS$  and  $NL$  as a function of frequency are obtained, by using least squares as follows. At each frequency,  $mIPD$  is related to the incident azimuth by the following form

$$mIPD = \angle \frac{\Gamma + j \tan\left(\pi \frac{d}{\lambda} \sin \theta\right)}{\Gamma - j \tan\left(\pi \frac{d}{\lambda} \sin \theta\right)} \quad (7)$$

where  $\Gamma = x + jy$  is the unknown parameter, which can be obtained by using nonlinear least squares. Once  $\Gamma$  is solved,  $ADS$  and  $NL$  can be calculated by using their definitions. This curve fitting technique can help reduce the influences of the environmental noise, disturbance of sound field by the mounting fixtures, and the randomness of the asynchronous sampling, which is particularly important for the  $NL$  characterization.

As illustrated in Figure 4-15(a), it can be clearly seen that the designed device does exhibit a similar dual optimality characteristic as the fly ear, which is, however, achieved at a different frequency of 8 kHz. At this frequency, the experimental value of  $mIPD$  is clearly a linear function of  $\theta$  in the range of  $-30^\circ \leq \theta \leq 30^\circ$ , as shown in Figure 4-15(b).  $ADS$ , the slope of  $mIPD$  in this azimuth range, is estimated to be 1.69 deg/deg, which is 10 times the  $DS$  at the midline in the acoustic stimulus (0.17 deg/deg). Such a directional sensitivity is only obtainable from a conventional microphone pair with a separation that is 10 times larger.

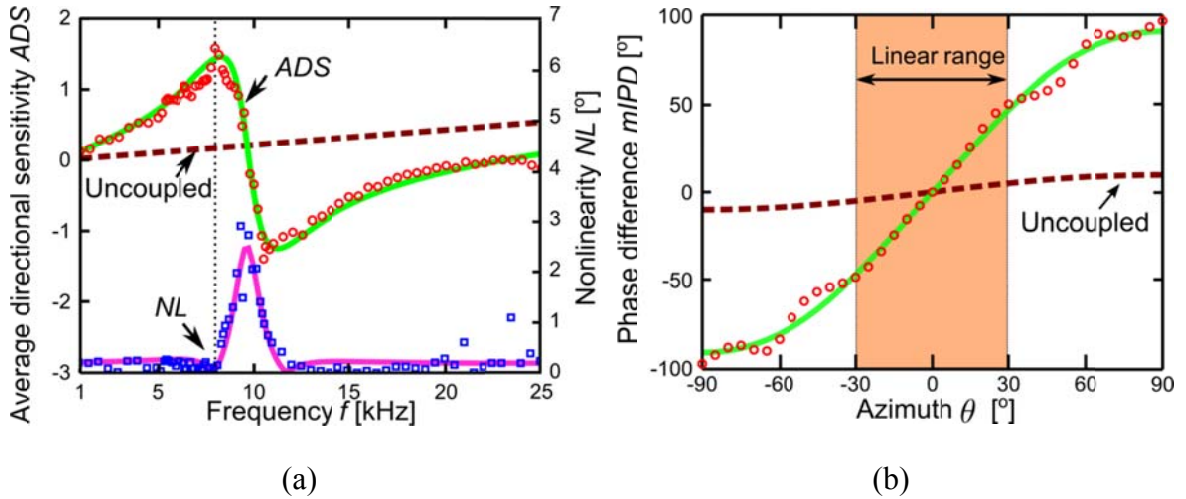


Figure 4-15: Dual-optimality of the fly-ear inspired directional microphone. (a) Spectra of averaged directional sensitivity ( $ADS$ ) and nonlinearity ( $NL$ ). It shows the device works best at 8 kHz, where it has maximal  $ADS$  and minimal  $NL$ . (b) Spatial distribution of phase difference  $mIPD$  at 8 kHz .

#### 4.5 Fly inspired localization scheme

The fly utilizes a unique localization/lateralization scheme to pinpoint the host crickets (Mason et al., 2001). When the source is out of the linear range around the midline, the fly makes a simple left/right decision (lateralization) and moves its head toward the source until the source falls in the linear range. Once the source is in the linear range, the fly can estimate the sound source position more accurately and turns by the calculated angle size.

To implement the fly's localization/lateralization scheme, a sigmoid approximation is first used to represent the relationship between the phase difference  $mIPD$  and the azimuth  $\theta$ , as shown in Figure 4-16. The slope in the linear range  $-30^\circ \leq \theta \leq 30^\circ$  is 1.69 deg/deg, which is the value of  $ADS$  at this frequency.

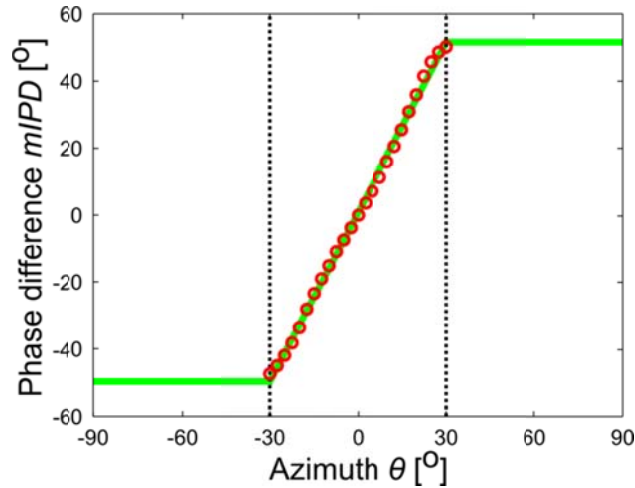


Figure 4-16: Approximation of the relationship between the phase difference  $mIPD$  and azimuth  $\theta$  by a sigmoid function (blue solid line). Red dots are experimental results.

Note that the sensor does not need to acquire signals continuously. Rather, data acquisition is carried out only at some discretized time instants. If the measured  $mIPD$  is larger than that obtainable at  $\theta = \pm 30^\circ$ , a lateralization decision (i.e., left or right) is made to rotate the sensor toward the sound source with a constant step (e.g.,  $20^\circ$ ) until the source is within the linear range. A localization decision is then performed and the actual source location is estimated by using the linear portion of the sigmoid approximation. Finally, localization is achieved when the sensor midline pinpoints the source.

One example is given in Figure 4-17, where the source's initial position is at  $80^\circ$ . In the whole process, the sensor is rotated by  $20^\circ$  for three times (three lateralization steps) till the source reaches the linear range, followed by one localization step. Combining the fly-ear inspired directional microphone and this bio-inspired localization-lateralization scheme, the developed sound source localization system can take full advantage of the

high sensitivity and low nonlinearity in this azimuth range  $-30^\circ \leq \theta \leq 30^\circ$  at its optimal working frequency 8 kHz.

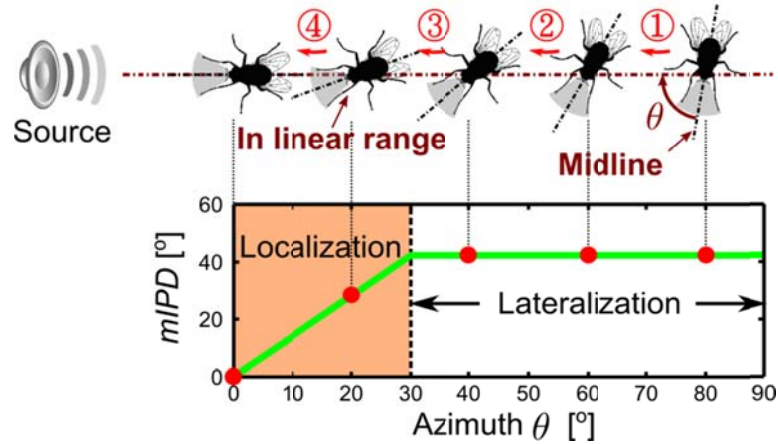


Figure 4-17: An example of applying the bio-inspired sound source localization scheme for an initial azimuth of  $80^\circ$

This localization scheme is implemented using the robotic platform shown in Figure 4-12. First, this platform is used to demonstrate its localization ability for stationary sound source (a chirp sound of 8 kHz is played through the speaker). Figure 4-18 shows the trajectories of the sound source localization for various starting azimuth positions. For any initial position in the range of  $-30^\circ \leq \theta \leq 30^\circ$ , it only requires up to four steps to locate the sound source. As shown in Figure 4-19, the errors of azimuth estimation are all within  $1.88^\circ \pm 2^\circ$ . The standard deviation is only  $0.84^\circ$ , which, divided by *ADS*, translates to a directional resolution of  $0.50^\circ$ .

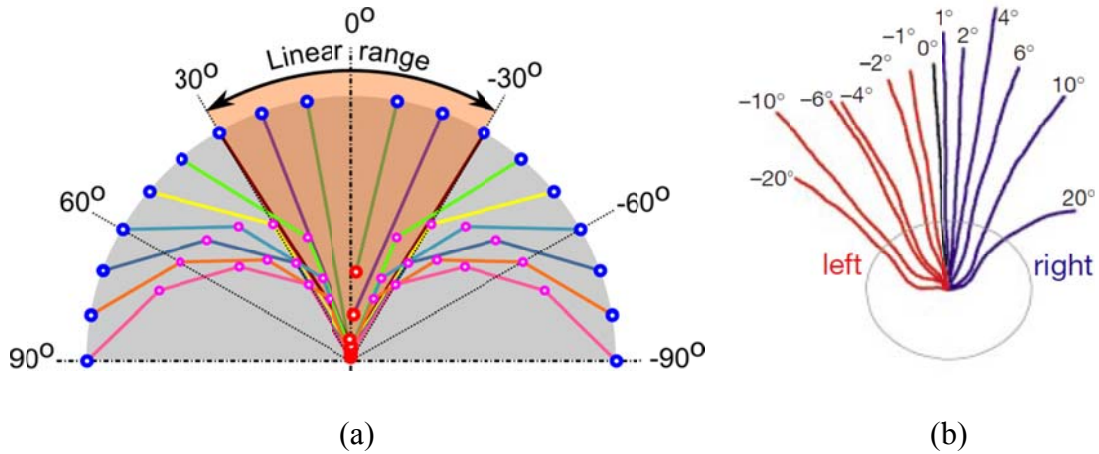


Figure 4-18: Trajectories of sound source localization using fly's localization/lateralization scheme. (a) Trajectories when the fly's localization scheme is implemented on a fly-ear inspired sensor using a motorized rotational stage. Blue dots on the periphery represent the initial azimuth position, red dots near the origin are the final position, and magenta dots are the positions in between. (b) Virtual path of the fly in the phonotactic experiment (Mason et al., 2001).

The estimation error is attributed to several reasons. First, the data acquisition is not synchronized across different analog input channels. Second, although the measurement was made in an anechoic chamber, the mounting fixture, including the tripod, rotational stage and mounting rod, is much larger than the device size. This will disturb the input sound wave to the directional microphone. Third, the sensor may drift at the tip of the mounting rod as it is secured by Scotch double-sided tape. Last, as discussed previously, the time resolution is limited by the sampling rate of 500 kHz, and a curve fitting method is used to improve the resolution. However, the simulation results show that even if the signals are perfect, the standard deviation of azimuth estimation is  $0.30^\circ$ .

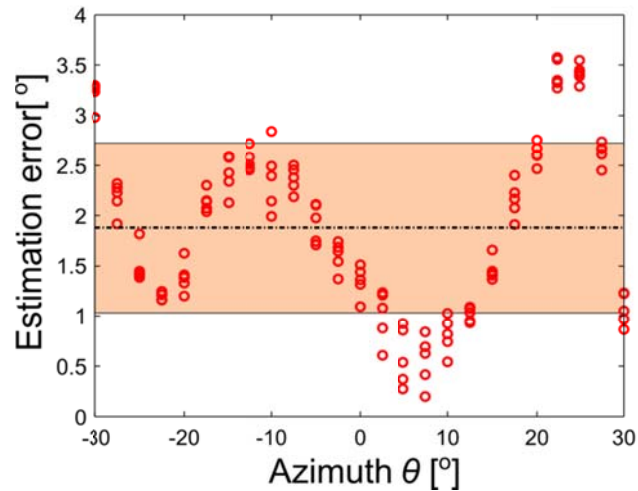


Figure 4-19: Estimation error using the fly-ear inspired sensor and bio-inspired localization/lateralization scheme. The mean and standard deviation of the error are  $1.88^\circ$  and  $0.85^\circ$ , respectively.

Given the non-perfect conditions, the developed sound source localization system is still shown to achieve a localization resolution of  $\pm 2^\circ$ , which is the same as that achieved by the fly in the phonotactic experiment (Mason et al., 2001). Note that the localization performance does not deteriorate when the testing setup is moved from the anechoic chamber to an in-door laboratory environment.

The developed robotic platform is also investigated to track a moving sound source (represented by the same 8 kHz chirp sound). Note that in the robotic platform, the fly-ear inspired sensor is mounted on the top of a rotational stage (sensor stage), which is stacked on top of another rotational stage (speaker stage). The random movement of the sound source is realized by operating the speaker stage. In the example shown in Figure 4-20, the sound source initially is located at an azimuth of  $80^\circ$ , and the sensor is able to



localize it in four steps as previously described. When the sound source starts to move randomly after that, the robotic platform is able to keep track of the moving source.

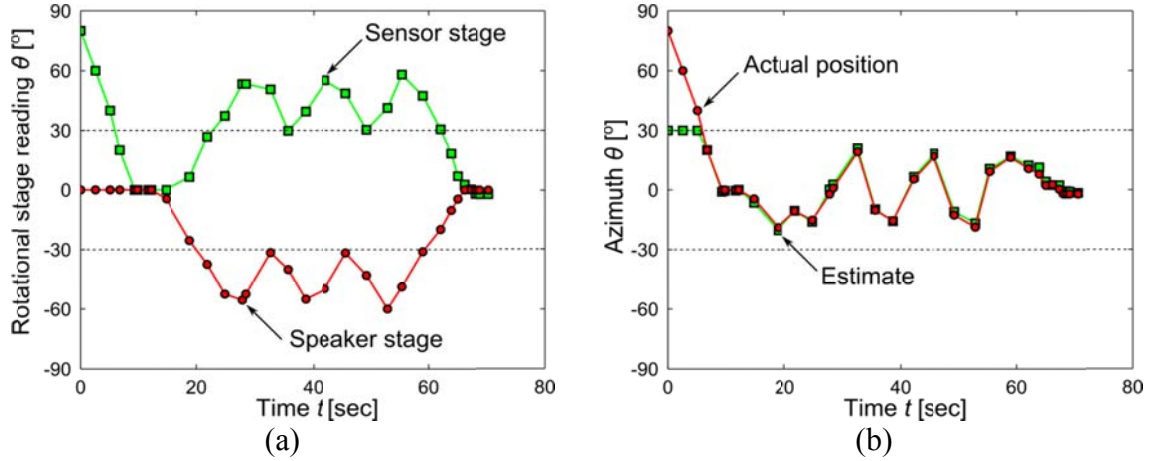


Figure 4-20: Tracking of a randomly moving source using the developed robotic platform. (a) Time history of the readings from the speaker and sensor stages. (b) Time history of the actual and estimated azimuths of the sound source.

#### 4.6 Summary

The framework established in Chapter 2 and the continuum mechanics model developed in Chapter 3 are used to guide the design of a fly-ear inspired miniature directional microphone. First, a low-coherence fiber optic interferometer system with high sensitivity and large signal-to-noise ratio is developed to detect the diaphragm vibrations subject to the sound stimulus. Then, as a proof-of-concept prototype, a large-scale directional microphone with an interaural separation of 25.4 mm is fabricated and characterized. At 1.1 kHz, the phase difference is amplified by more than 4 times. Next, a miniature directional microphone that is designed to mimic the fly's dual optimality at 8 kHz is micro-machined and characterized in an anechoic chamber. The experimental results show that the fabricated device indeed has the dual-optimality property as the fly ear. At

its optimal working frequency 8 kHz, the directional sensitivity is amplified by 10 times. Finally, a bio-inspired localization-lateralization scheme is developed and implemented on a robotic platform with the fly-ear inspired sensor mounted. A directional resolution of only  $0.5^\circ$  is demonstrated with this robotic platform, which is better than the fly's localization resolution of  $\pm 2^\circ$ .

## Chapter 5 Summary

### 5.1 Summary of the dissertation work

Hearing animals mainly rely on a few directional cues for sound-source localization, including interaural intensity difference (IID), interaural time difference (ITD), and sound spectral shape difference. Since these cues are proportional to an animal's interaural separation, there exists a fundamental physical constraint for sound source localization – a size constraint. With such a constraint, small animals, especially insects, face formidable challenges. The same fundamental physical constraint applies to a conventional microphone pair or array used for sound source localization, in which the separation between individual microphones need to be larger than a critical distance.

The striking innovation found in the tachinid fly *Ormia ochracea* provides a new solution to tackle the aforementioned size constraint through the mechanical coupling between the eardrums. This innovation helps the fly possess a superacute directional hearing capability, which can inspired one to address the size constraint in acoustic sensor development.

Although several fly-ear inspired directional microphones have been reported in the literature, their working principles cannot fully capture the essence of the fly ear mechanism. This is also due to the fact that before this dissertation work, no study has

been reported to investigate how the fly ear's structural parameters are tailored to facilitate the superior localization of the calling song of fly's host at 5 kHz.

This dissertation work aims to unravel the underlying science of the fly ear mechanism and provide a framework for developing miniature acoustic sensors for sound source localization. The dissertation work is summarized as follows.

First, by using the two degrees-of-freedom (2-DOF) model and the fly ear parameters reported in the literature, an enhanced understanding of the underlying science of the fly ear structure has been achieved. Since the fly is shown to only be able to accurately locate its host in the azimuth range of  $\sim -30^\circ$  to  $30^\circ$ , two performance metrics are defined: average directional sensitivity (*ADS*) and nonlinearity (*NL*). When using a straight line to approximate the relationship between phase difference *mIPD* and azimuth  $\theta$ , *ADS* represents the slope and *NL* is the resulting estimation error. Through an analytical study, it has been found that the fly possesses a unique dual-optimality characteristic; the fly ear achieves the maximum directional sensitivity *ADS* and the minimum nonlinearity *NL* at the calling song frequency of the crickets (5 kHz). This indicates that the fly ear represents a “nature designed optimal structure” for obtaining the best acoustic directional cues at 5 kHz. The 2-DOF model has also been used to study the effects of key parameters on the directional hearing performance, including the stiffness ratio, the damping ratios, and the separation-to-wavelength ratio. The key is to achieve proper contributions from both the rocking and bending modes. Moreover, it has been shown that this dual-optimality property is replicable in a synthetic device that can be tailored to work at any frequency or any device size. A framework has been developed to guide the

development of such a synthetic device. Given the target working frequency and/or desired size, the two natural frequencies for the rocking and bending modes have been obtained in this framework for both high damping and low damping scenarios. Parametric studies have been carried out to study the effects of the previously identified key parameters on the performance of the fly ear and fly-ear inspired device.

Next, a novel bio-inspired directional microphone has been designed. It consists of two clamped circular diaphragms with their centers connected by a medially-pivoted bridge. Different from the microphones reported in the literature, this design is intended to not only employ the mechanical coupling mechanism but also obtain a proper contribution from both the rocking and bending modes. Correspondingly, a comprehensive continuum mechanics model has been developed to further understand the mechanism and help guide the design. Parametric studies have also been carried out to analyze the effects of key parameters, including the ratio of Young's modulus, density and geometric dimensions of the beam. In particular, the results obtained with the continuum mechanics have shown that the air gap underneath a diaphragm has significant effects on the dynamics of the single air-backed diaphragm and the mechanically coupled diaphragms. In addition to the commonly known stiffness effect, the air gap has been shown to have a mass effect, which can be pronounced for short air gaps.

For proof-of-concept, a large-scale directional microphone has been developed by using traditional machining and assembly tools. In the experiments, the deflections of the diaphragms are detected by a low-coherence fiber optic interferometer. Experimental results have shown that phase difference can be amplified by 4 times.

Built upon the design framework, continuum mechanics model, and the knowledge gained in the development of the proof-of-concept large-scale device, a fly-ear inspired MEMS directional microphone has been developed, which has the same interaural separation as the fly ear but achieves the dual-optimality at a different working frequency (8 kHz). This device consists of four layers. The top layer has two circular clamped diaphragms connected by a pivoted bridge, which is similar to its large-scale counterpart. The bottom three layers are designed for tuning the damping characteristics of the system.

The micro-scale device has been characterized by measuring the directional cues for various frequencies and azimuths. The experimental results have shown that this device does possess the dual-optimality characteristic of the fly ear. Working at its optimal frequency of 8 kHz, the directional sensitivity is determined to be 1.69, which is equivalent to that obtainable by a conventional microphone pair of 10 times larger.

Inspired by the fly's localization/lateralization scheme, a control scheme for sound source localization has been developed and implemented on a robotic platform with two motorized rotational stages. The fly-ear inspired sensor is designed to have the best directional sensitivity and linearity in the azimuth range of  $-30^\circ \leq \theta \leq 0^\circ$ . To utilize this dual-optimality in the fly inspired localization scheme, the sensor is steered toward the sound source when the source is out of the linear range, and an accurate azimuth estimation is made once the source falls within the linear range. A localization accuracy of better than  $\pm 2^\circ$  (the same as the fly ear) has been demonstrated in an indoor lab environment.

The original contributions in this dissertation work are summarized as follows.

**Contribution 1: The fly ear has been revealed to be a “nature designed optimal structure” that achieve maximal directional sensitivity  $ADS$  and minimal nonlinearity  $NL$  simultaneously (dual-optimality) at the calling song frequency of host crickets.** This finding is consistent with the fly’s localization/lateralization scheme in that it utilizes the linear azimuth range to achieve the best localization accuracy. The investigation shows that properly tuned structural parameters are as important as the mechanical coupling mechanism itself in designing a fly-ear inspired directional microphone.

**Contribution 2: A framework is established to mimic the fly ear’s dual optimality in a synthetic device for other frequencies and sizes.** For given damping ratios, the natural frequencies of the rocking and bending modes are obtained as functions of separation-to-wavelength ratio.

**Contribution 3: A directional microphone consisting of two diaphragms connected by a center pivoted bridge is developed to mimic the fly ear.** Different from previously reported work in the literature, this design is intended to use the directional cues as the fly does to carry out sound source localization. It does not require any additional sensors to measure the absolute value of pressure or pressure gradient.

**Contribution 4: A novel comprehensive continuum mechanics model is developed for understanding the dynamics of a fly-ear inspired directional microphone with mechanically coupled diaphragms.** This model has been verified against a finite

element model in ANSYS and the equivalence of this model the 2-DOF model has been established. This model is expected to provide more accurate prediction of the sensor behavior and a better guideline for the sensor development. **The effects of air gap are studied from the perspective of sensor design to provide guidelines for pressure sensors with an air-backed diaphragm.** The key finding from this study is the air gap not only has a stiffness effect, but also a mass effect.

**Contribution 5: A bio-inspired localization/lateralization scheme is developed for sound source localization with a fly ear inspired sensor.** With the fly-ear inspired sensor mounted on a robotic platform, the fly's localization/lateralization scheme is implemented to achieve a standard deviation of  $0.84^\circ$  for the azimuth estimation.

## 5.2 Future work

Upon the completion of this dissertation work, the future work is suggested as follows.

- 1) **Active tuning of fly-ear inspired directional microphones.** In this dissertation work, the framework for designing acoustic sensors to mimic the fly's dual-optimality is passive. Once the sensor is designed and fabricated for a specific frequency, it cannot be changed and there is no mechanism to compensate the discrepancy between the designed value and the actual one. The active tuning is aimed to provide a means to fine tune some properties of the diaphragms or the bridge to minimize the discrepancy due to the fabrication process. When a continuous tuning is performed, the working frequencies can be swept to achieve a desired broadband operation and for



each of the frequency the device possesses the dual-optimality characteristic. One possibility to realize the active tuning is to apply a lead zirconate titanate (PZT) film on top of the diaphragms and/or the bridge. Biases can be applied to the films to change their equivalent stiffness.

- 2) **Integration of sensor system on a miniature platform.** Although the fly-ear inspired sensor is small, the optical detection system is fairly bulky as it is built using commercially available components, such as power source, light source, photodetectors, and data acquisition board. Research on this topic is being carried out by colleagues in our research group to integrate all the components into a package about the size of a business card. In addition to optical sensing mechanism, other detection methods, for example, capacitance and resistance based detection methods, which are friendlier and mature to MEMS/circuitry integration, can also be attempted.
- 3) **Extension the fly-ear inspired sensor to two or three dimensions.** The fly-ear inspired directional microphone can only locate a sound source in one dimension (1D) (i.e., the azimuth). However, this work can be readily extended to locate sound source in two or three dimensions (2D or 3D). Lisiewski in our research group has used the same fabrication process to develop a fly-ear inspired directional microphone consisting of three mechanically coupled diaphragms on a single plane (Lisiewski, Liu, Yu, Currano, & Gee, 2011). By using this sensor, localization of a sound source in two dimensions (i.e., azimuth and elevation) has been demonstrated. Taking the advantage of mass production of MEMS fabrications, an alternative

method is to use an array of 1D directional microphones. Without increasing the complexity of the individual device, the directional microphone array can also use the existing algorithms in sound source localization. One of the ultimate goals is to use the fly-ear inspired acoustic sensors as the “ears” of a micro air vehicle.

## Appendix A: Matlab codes and ANSYS input files

### A1 Matlab codes for the lumped two degrees-of-freedom model

---

**File name: getIPDNorm.m**

```
%% Calculate the interaural phase difference using the normalized formula
%
% IPD = getIPDNorm(eta,chil,xil,xi2,theta,omega)
%
% Input:
%
% eta      - resonance frequency ratio eta=f2/f1
% chil     - separation-to-wavelength ratio at f1
% xil      - damping factor for the first mode
% xi2      - damping factor for the second mode
% theta    - incident angle, deg
% omega    - normalized frequency, omega = f/f1
%
% Output:
%
% IPD      - phase difference, deg

function IPD = getIPDNorm(eta,chil,xil,xi2,theta,omega)
    theta = theta(:);
    omega = omega(:);
    [THETA,OMEGA] = meshgrid(theta,omega);
    Gamma = (1-OMEGA.^2+2*xil*li*OMEGA)./(eta^2-OMEGA.^2+2*xi2*li*eta*OMEGA);
    chi = chil*OMEGA;
    phi = 2*pi*chi.*sind(THETA);
    nom = Gamma+li*tan(phi/2);
    den = Gamma-li*tan(phi/2);
    IPD = angle(nom./den)*180/pi;
end
```

---

**File name: getDSNorm.m**

```
%% Calculate the directional sensitivity using the normalized formula
%
% DS = getDSNorm(eta,chil,xil,xi2,theta,omega)
%
% Input:
%
% eta      - resonance frequency ratio eta=f2/f1
% chil     - separation-to-wavelength ratio at f1
% xil      - damping factor for the first mode
% xi2      - damping factor for the second mode
% theta    - incident angle, deg
% omega    - normalized frequency, omega = f/f1
%
% Output:
%
% DS      - directional sensitivity, DS
```

```
function DS = getDSNorm(eta,chi1,xi1,xi2,theta,omega)
    theta = theta(:);
    omega = omega(:);
    [THETA,OMEGA] = meshgrid(theta,omega);
    Gamma = (1-OMEGA.^2+2*xi1*1i*OMEGA)./(eta^2-OMEGA.^2+2*xi2*1i*eta*OMEGA);
    chi = chi1*OMEGA;
    reGamma = real(Gamma);
    imGamma = imag(Gamma);
    tanphi = tan(pi*chi.*sind(THETA));
    nom1 = 2*reGamma.*(reGamma.^2+imGamma.^2+tanphi.^2);
    nom2 = (1+tanphi.^2)*pi.*chi.*cosd(THETA);
    den = (reGamma.^2+imGamma.^2-tanphi.^2).^2+4*reGamma.^2.*tanphi.^2;
    DS = nom1.*nom2./den;
end
```

---

## A2 Matlab codes for processing the acquired signals to calculate directional cues

---

**File name: getCues2Mic.m**

```
%% calculate interaural directional cues
%   number of microphones: two
%   syntax: [IPD,ITD,IID] = getCues2Mic(X,fc,fs)
%   input:
%       X       -   time signals, two columns
%       fc      -   signal frequency
%       bw      -   bandwidth
%       fs      -   sampling frequency
%   output:
%       IPD     -   interaural phase difference, deg
%       ITD     -   interaural time difference, sec
%       IID     -   interaural intensity difference, dB
%%
function [IPD,ITD,IID,A1,A2] = getCues2Mic(X,fc,bw,fs)

x1 = X(1:end,1);
x2 = X(1:end,2);
dt = 1/fs;

%%   Amplitude
A1 = sqrt(2)*norm(x1)/sqrt(length(x1));
A2 = sqrt(2)*norm(x2)/sqrt(length(x2));
IID = 20*log10(A1/A2);

%%   Filter data
Wn = [fc-bw/2 fc+bw/2]/(fs/2);
[b,a] = butter(2,Wn);
x1 = filtfilt(b,a,x1);
x2 = filtfilt(b,a,x2);

%%   Cross-correlation
[delay,~,fig] = getDelay(x1,x2,fs/fc);
ITD = delay*dt;
close(fig);
IPD = fc*ITD*360;
IPD = mod(IPD+180,360)-180;
ITD = IPD/360/fc;
```

---

**File name: getDelay.m**

```
%% Calculate the time delay between two signals
%
%   [delay_fit,delay_pk,fig] = getDelay(x1,x2,f,bw)
%
%   Input:
%       x1      -   first signal
%       x2      -   second signal
%       f       -   frequency of the puretone signals
%       bw      -   bandwidth for the filtering
```

```

%
% Output
%     delay_fit   -   time delay after the curve-fitting
%     delay_pk    -   time delay by finding the max
%     fig         -   figure handle
%
% peakdet.m is used to find the peaks of the cross-correlation. This is
% is written by Eli Billauer, and available to public
% http://www.billauer.co.il/peakdet.html

```

```
function [delay_fit,delay_pk,fig] = getDelay(x1,x2,f,bw)
```

```

%%
N = length(x1);
A1 = sqrt(2)*norm(x1)/sqrt(N);
A2 = sqrt(2)*norm(x2)/sqrt(N);
x1 = x1/A1;
x2 = x2/A2;
y = xcorr(x2,x1);
delta = (max(y)-min(y))/5;
[maxtab,mintab] = peakdet(y,delta);
%%
if exist('f','var') && exist('bw','var')
    Wn = [f-bw/2 f+bw/2];
    [b,a] = butter(6,Wn);
    x1 = filtfilt(b,a,x1);
    x2 = filtfilt(b,a,x2);
end
%% only use the center peak
[max_v,max_i] = max(y);
mintab1 = sort(mintab(:,1),'ascend');
[v1,index1] = min((mintab1-max_i).^2);
mintab2 = mintab1;
mintab2(index1) = [];
[v2,index2] = min((mintab2-max_i).^2);
cf_index1 = min(mintab1(index1),mintab2(index2));
cf_index2 = max(mintab1(index1),mintab2(index2));
cf_start = max_i-floor((max_i-cf_index1)/4);
cf_end = max_i+ceil((cf_index2-max_i)/4);
X = (cf_start:cf_end)-max_i;
Y = y(cf_start:cf_end);
X = X(:);
Y = Y(:);
p = polyfit(X,Y,2);
delay_fit = -p(2)/p(1)/2+max_i-N;
delay_pk = max_i-N;

fig = figure('Position',[100 300 1000 300]);
subplot(1,3,1)
plot(0:N-1,x1,'b-','linewidth',2)
hold on
plot(0:N-1,x2,'r--','linewidth',2)
legend('Mic 1','Mic 2')
xlabel('Sample #')
ylabel('Value')

subplot(1,3,2)
plot(1-N:1:N-1,y,'b-','linewidth',2)
set(gca,'xlim',[1-N N-1],'ylim',[min(y) max(y)])
xlabel('Sample #')

```

```
ylabel('Cross-correlation')

XX = min(X):0.2:max(X);
subplot(1,3,3)
plot(X+max_i-N,Y,'bs','markersize',6,'markerfacecolor','b');
hold on
plot(XX+max_i-N,polyval(p,XX),'g-','linewidth',2.5)
vline([1 1]*delay_pk,'b-.')
vline([1 1]*delay_fit,'g-.')
xlabel('Delay [samples]')
ylabel('Cross-correlation')

end
```

---

## A3 Matlab codes for the continuum mechanics model

---

**File name:** getPlateModes1Order.m

```
%% Get the vibration modes (radial direction) of circular clamped plate
% for a specific order within the specified frequency range
%
% Usage:
% [U,ALPHA] = getPlateModes1Order(m,modes,chi_t,alpha_min,alpha_max)
% Input:
% m - integer order number, starting from zero.
% modes - number of modes to solve
% chi_t - normalized tension parameter
% alpha_min - lower bound of normalized frequency
% alpha_max - Upper bound of normalized frequency
% Output:
% U - mode shape function
% ALPHA - normalized frequency

function [U,ALPHA] = getPlateModes1Order(m,modes,chi_t,alpha_min,alpha_max)
%%
if nargin < 1
    disp(['The first argument for order number is not specified. ' ...
        'The default value of zero is used.']);
end
if nargin < 2 || isempty(modes)
    modes = Inf;
end
if nargin < 3 || isempty(chi_t)
    chi_t = 0;
end
if nargin < 4 || isempty(alpha_min)
    alpha_min = 0;
end
if nargin < 5 || isempty(alpha_max)
    alpha_max = Inf;
end
if alpha_min < 0
    disp(['Low bound of frequency range has to be non-negative. ' ...
        'The default value of zero is used.'])
    alpha_min = 0;
end
if alpha_max <= 0
    disp(['Upper bound of frequency range has to be positive. ' ...
        'The default values of infinity is used.'])
    alpha_max = Inf;
end

if modes <= 0
    error('Number of modes has to be positive')
end

if isinf(modes) && isinf(alpha_max)
    error(['Either the number of modes or the upper bound' ...
        ' has to be specified'])
end

alpha2_min = sqrt((sqrt(chi_t^2+4*12*alpha_min^2)-chi_t)/2);
alpha2_max = sqrt((sqrt(chi_t^2+4*12*alpha_max^2)-chi_t)/2);
```



```

syms r alpha2 real;
% Eliminate alpha1 by substitution
alpha1 = sqrt(alpha2^2+chi_t);
alpha2_step = 0.2;

Ur = besselj(m,alpha2*r)*besseli(m,alpha1)...
    -besselj(m,alpha2)*besseli(m,alpha1*r);
dUr = diff(Ur,r);
% Apply boundary condition at r=1
f_bnd = vpa(subs(dUr,r,1));
% Find the roots
alpha2_value1 = alpha2_min;
alpha2_value2 = alpha2_value1+alpha2_step;

options=optimset('TolX',1e-6);
count = 0;
stop = 0;
U = sym([]);
while (~stop)
    if (subs(f_bnd,alpha2_value1)*subs(f_bnd,alpha2_value2) < 0)
        ALPHA2 = fzero(@(aa)real(subs(f_bnd,alpha2,aa)),...
            [alpha2_value1,alpha2_value2],options);
        ALPHA1 = sqrt(ALPHA2^2+chi_t);
        count = count+1;
        U(count) = besselj(m,ALPHA2*r)*besseli(m,ALPHA1)...
            -besselj(m,ALPHA2)*besseli(m,ALPHA1*r);
        ALPHA(count) = ALPHA1*ALPHA2/sqrt(12);
        % Normalize mode shape function
        integral = vpa(U(count)*U(count)*r);
        amn = quadl(@(radius)subs(integral,r,radius),0,1);
        U(count) = vpa(U(count)/sqrt(amn));

    end
    alpha2_value1 = alpha2_value2;
    alpha2_value2 = alpha2_value1+alpha2_step;
    if ~isempty(modes) && count >= modes
        stop = 1;
    end
    if ~isempty(alpha_max) && alpha2_value1 > alpha2_max
        stop = 1;
    end
end
if count == 0
    U = [];
    ALPHA = [];
end
U = U(logical(ALPHA >= alpha_min & ALPHA <= alpha_max));
ALPHA = ALPHA(logical(ALPHA >= alpha_min & ALPHA <= alpha_max));
U = U(:);
ALPHA = ALPHA(:);

end

```

---

**File name: getAirModes1Order.m**

```

%% Get the vibration modes (radial direction) of cylindrical air cavity
% for a specific order within the specified frequency range
%

```

```

% Usage:
% [U,BETA] = getAirModes1Order(m,modes,beta_min,beta_max)
% Input:
% m - integer order number, starting from zero.
% modes - number of modes to solve
% beta_min - lower bound of normalized frequency
% beta_max - upper bound of normalized frequency
% Output:
% U - mode shape function
% BETA - normalized frequency
function [U,BETA] = getAirModes1Order(m,modes,beta_min,beta_max)
%%
if nargin < 1
    disp(['The first argument for order number is not specified. ' ...
        'The default value of zero is used.']);
end
if nargin < 2 || isempty(modes) || modes <= 0
    modes = Inf;
end
if nargin < 3 || isempty(beta_min)
    beta_min = 0;
end
if nargin < 4 || isempty(beta_max)
    beta_max = Inf;
end
if beta_min < 0
    disp(['Low bound of frequency range has to be non-negative. ' ...
        'The default value of zero is used.'])
    beta_min = 0;
end
if beta_max <= 0
    disp(['Upper bound of frequency range has to be positive. ' ...
        'The default values of infinity is used.'])
    beta_max = Inf;
end
if isinf(modes) && isinf(beta_max)
    error(['Either the number of modes or the upper bound' ...
        ' has to be specified'])
end

syms r beta2 real;

Ur = besselj(m,beta2*r);
dUr = diff(Ur,r);
% Apply boundary condition at r=1
f_bnd = subs(dUr,r,1);

beta_step = 0.2;
beta_value1 = beta_min;
beta_value2 = beta_value1+beta_step;

options=optimset('TolX',1e-6);
count = 0;
stop = 0;

while (~stop)
    if (subs(f_bnd,beta_value1)*subs(f_bnd,beta_value2) <= 0)
        beta_sol = fzero(@(betabeta)subs(f_bnd,beta2,betabeta),...
            [beta_value1,beta_value2],options);
        count = count+1;
        U(count) = besselj(m,beta_sol*r);
        BETA(count) = beta_sol;
    end
end

```

```

        % Normalize mode shape function
        integrand = U(count)*U(count)*r;
        amn = double(int(integrand,r,0,1));
        U(count) = U(count)/sqrt(amn);
    end
    beta_value1 = beta_value2;
    beta_value2 = beta_value1+beta_step;
    if modes >= 0 && count >= modes
        stop = 1;
    end
    if beta_value1 > beta_max
        stop = 1;
    end
end
end
if count == 0
    U = [];
    BETA = [];
end
if ~isinf(modes)
    U = U(1:max(0,modes));
    BETA = BETA(1:max(0,modes));
end
U = U(logical(BETA >= beta_min & BETA <= beta_max));
BETA = BETA(logical(BETA >= beta_min & BETA <= beta_max));
U = U(:);
BETA = BETA(:);

end

```

---

**File name: getBeamModes.m**

```

%% Calcualte the mode shapes and natural frequency for a beam with
% free-pinned-free boundary condition
%
% Usage: [U,ETA] = getBeamModes(modes,chi_t,eta_min,eta_max)
%
% Inputs:
% modes - number of modes
% chi_t - chi_t = P*L^2/EI is the normalized axial load
% eta_min - lower bound of frequency range
% eta_max - upper bound of frequency range
%
% Outputs:
% U - mode shapes
% ETA - natural frequency parameter
% omega = sqrt(EI/mL^3)*eta^2
%
% Note: The beam has a length of 2L, and is pinned in the middle. x is
% normalized so that x=+/-1 on both ends

function [U,ETA] = getBeamModes(modes,chi_t,eta_min,eta_max)
%%
if isempty(modes) || modes <= 0
    modes = -1;
end
if nargin < 2 || isempty(chi_t)
    chi_t = 0;
end
if nargin < 3 || isempty(eta_min)

```

```

    eta_min = 0;
end
if nargin < 4 || isempty(eta_max)
    eta_max = Inf;
end
if isinf(modes) && isinf(eta_max)
    error(['Either the number of modes or the upper bound' ...
        ' has to be specified'])
end

syms x et real;
eh = sqrt(et^2-2*chi_t);

options = optimset('TolX',1e-6);

disp(['Solving the mode shapes and natural frequencies for' ...
    ' the coupling beam ...'])
fprintf(1,'\tMode #\t\tOMEGA\tType\n');

%% rigid motion
count = 1;
U(count) = x*sqrt(3/2);
ETA(count) = 0;

fprintf(1,'%8i\t%8.4f\tRIGID\n',count,ETA(count));

%% symmetric and anti-symmetric modes
et_step = 0.01;
et_min = sqrt(chi_t+sqrt(chi_t^2+12*eta_min^2));
et_max = sqrt(chi_t+sqrt(chi_t^2+12*eta_max^2));
et_le = et_min;
fsym = (eh*et^3-eh^3*et)*sinh(eh)*sin(et)+...
    2*eh^2*et^2*cosh(eh)*cos(et)+eh^4+et^4;
fsym_le = double(subs(fsym,et,et_le));
fanti = et*cos(et)*sinh(eh)-eh*sin(et)*cosh(eh);
fanti_le = double(subs(fanti,et,et_le));

stop = 0;
while ~stop
    et_ue = et_le+et_step;
    fsym_ue = double(subs(fsym,et,et_ue));
    fanti_ue = double(subs(fanti,et,et_ue));
    range = [et_le et_ue];
    ctrl_sym = 0;
    ctrl_anti = 0;
    % symmetric modes
    if fsym_le*fsym_ue < 0
        ctrl_sym = 1;
        etv = fzero(@(x)subs(fsym,et,x),range,options);
        ehv = subs(eh,et,etv);
        count = count+1;
        ETA(count) = ehv*etv/sqrt(12);
        c1 = ehv^2*etv^2*(etv*cos(etv)*sinh(ehv)-ehv*sin(etv)*cosh(ehv));
        c2 = ehv^5+ehv^3*etv^2*cos(etv)*cosh(ehv)...
            +ehv^2*etv^3*sin(etv)*sinh(ehv);
        c3 = etv^5+ehv^2*etv^3*cos(etv)*cosh(ehv)...
            -ehv^3*etv^2*sin(etv)*sinh(ehv);
        U(count) = c1*(cos(etv*x)-cosh(ehv*x))...
            +c2*sin(abs(etv*x))+c3*sinh(abs(ehv*x));
        integrand = U(count)*U(count);
        Bn = quadl(@(xx)subs(integrand,x,xx),-1,1);
        U(count) = vpa(U(count)/sqrt(Bn));
    end
end

```

```

        fprintf(1, '%8i\t%8.4f\tSYM\n', count, ETA(count));
    end
    % anti-symmetric modes
    if fanti_le*fanti_ue < 0
        ctrl_anti = 1;
        etv = fzero(@(x)subs(fanti,et,x),range,options);
        ehv = subs(eh,et,etv);
        count = count+1;
        ETA(count) = ehv*etv/sqrt(12);
        U(count) = ehv^2*sinh(ehv)*sin(etv*x)...
            +etv^2*sin(etv)*sinh(ehv*x);
        integrand = U(count)*U(count);
        Bn = quadl(@(xx)subs(integrand,x,xx),-1,1);
        U(count) = vpa(U(count)/sqrt(Bn));
        fprintf(1, '%8i\t%8.4f\tANTISYM\n', count, ETA(count));
    end
    %% sort the modes
    if ctrl_anti && ctrl_sym
        if ETA(count) < ETA(count-1)
            eta_swap = ETA(count-1);
            ETA(count-1) = ETA(count);
            ETA(count) = eta_swap;
            U_swap = U(count-1);
            U(count-1) = U(count);
            U(count) = U_swap;
        end
    end
    et_le = et_ue;
    fsym_le = fsym_ue;
    fanti_le = fanti_ue;
    if et_le > et_max
        stop = 1;
    end
    if modes > 0 && count >= modes
        stop = 1;
    end
end
U = U(logical(ETA <= eta_max));
ETA = ETA(logical(ETA <= eta_max));
disp('DONE!')
end

```

---

## A4 ANSYS input files

---

```
File name: dirMic-wo-cavity_using_shell-elements_modal.inp
!* MODAL ANALYSIS OF TWO MEMBRANES COUPLED BY A BRIDGE
!* NO AIR CAVITY

!* uMKSv Unit: http://www.kxcad.net/ansys/ANSYS/ansyshelp/Hlp_G_COU1_3.html
!* Length:   m      * 1e6      ->   um
!* Force:    N      * 1e6      ->   uN
!* Time:     s      * 1        ->   s
!* Velocity  m/s    * 1e6      ->   um/s
!* Mass:     kg     * 1        ->   kg
!* Pressure  Pa     * 1e-6     ->   MPa
!* Density   kg/m^3 * 1e-18    ->   kg/(um)^3
!* Power     W      * 1e12     ->   pW

NMOD = 20          ! NUMBER OF MODES TO BE CALCULATED
FREQLB = 1E1      ! LOWER BOUND OF THE FREQUENCY RANGE
FREQUB = 1E6     ! UPPER BOUND OF THE FREQUENCY RANGE
NDIVR = 20       ! NUM OF DIVS ALONG DIAPHRAGM'S RADIAL DIR
NDIVBX = 30     ! NUM OF DIVS ALONG BEAM'S AXIAL DIR
NDIVBY = 10     ! NUM OF DIVS ALONG BEAM'S WIDTH DIR

!* DIMENSIONS OF THE DIAPHRAGM/MEMBRANE
RD = 500         ! DIAPHRAGM RADIUS
HD = 0.50       ! DIAPHRAGM THICKNESS

!* DIMENSIONS FOR THE BRIDGE
L = 600          ! HALF LENGTH
B = 300          ! WIDTH
HB = 2.5        ! THICKNESS

!* MATERIAL LIBRARY
E_SI = 169E3     ! YOUNG'S MODULUS OF SILICON
NU_SI = 0.25     ! POISSON'S RATIO OF SILICON
RHO_SI = 2.3E-15 ! DENSITY OF SILICON

E_SIO2 = 90E3   ! YOUNG'S MODULUS OF OXIDE
NU_SIO2 = 0.17  ! POISSON'S RATIO OF OXIDE
RHO_SIO2 = 2.2E-15 ! DENSITY OF OXIDE

E_SI3N4 = 290E3 ! YOUNG'S MODULUS OF NITRIDE
NU_SI3N4 = 0.24 ! POISSON'S RATIO OF NITRIDE
RHO_SI3N4 = 3.1E-15 ! DENSITY OF NITRIDE

!* CHOOSE MATERIAL FOR THE DIAPHRAGME/MEMBRANE AND BRIDGE/BEAM
ED = E_SI
NUD = NU_SI
RHOD = RHO_SI

EB = E_SI3N4
NUB = NU_SI3N4
RHOB = RHO_SI3N4

/PREP7
!* ELEMENT TYPE: SOLID FOR THE DIAPHRAGM/MEMBRANE
```

```

ET,1,SHELL181

!* MATERIAL MODEL FOR THE MEMBRANE
MP,EX,1,ED
MP,NUXY,1,NUD
MP,DENS,1,RHOD

!* MATERIAL MODEL FOR THE MEMBRANE
MP,EX,2,EB
MP,NUXY,2,NUB
MP,DENS,2,RHOB

!* REAL CONSTANT/SECTION FOR THE DIAPHGRAM/MEMBRANE
SECTYPE,1,SHELL
SECDATA,HD,,

!* REAL CONSTANT/SECTION FOR THE BRIDGE/BEAM
SECTYPE,2,SHELL
SECDATA,HB,,

!* GEOMETRY
LOCAL,11,1,-L,0,0,, , ,1,1,
LOCAL,12,1,L,0,0,, , ,1,1,
CSYS,11
WPCSYS,-1
CYL4,0,0,RD,, , ,

!* MESH THE MEMBRANE
HPTCREATE,AREA,1,,COORD,0,0,0
AESIZE,1,RD/NDIVR,
MAT,1
TYPE,1
SECNUM,1
MSHAPE,0,2D
MSHKEY,2
AMESH,ALL

!* COPY THE AREA TO GENERATE ANOTHER DIAPHGRAM
CSYS,0
AGEN,2,1,, ,2*L,, , ,0

!* APPLY THE CLAMPED BOUNDARY CONDITION
CSYS,11
NSEL,S,LOC,X,RD
NSEL,R,LOC,Z,0
CM,NEDGEL,NODE
CSYS,12
NSEL,S,LOC,X,RD
NSEL,R,LOC,Z,0
CM,NEDGER,NODE
ALLSEL,ALL
CSYS,0
CMSEL,S,NEDGEL
CMSEL,A,NEDGER
D,ALL,UX,0
D,ALL,UY,0
D,ALL,UZ,0
D,ALL,ROTX,0
D,ALL,ROTY,0
D,ALL,ROTZ,0
ALLSEL,ALL

```

```

!* NODE AT DIAPHRAGM CENTERS
NDL = NODE(-L,0,0)
NDR = NODE(L,0,0)

!* GEOMETRY FOR THE BEAM
CSYS,0
WPCSYS,-1
BLC4,-L,-B/2,2*L,B

!* MESH THE BEAM
ASEL,S,LOC,X,0
LSLA,S
LSEL,U,LOC,Y,-B/2
LSEL,U,LOC,Y,B/2
LESIZE,ALL,,NDIVBY
ASEL,S,LOC,X,0
LSLA,S
LSEL,U,LOC,X,-L
LSEL,U,LOC,X,L
LESIZE,ALL,,NDIVBX
MAT,2
TYPE,1
SECNUM,2
AMESH,ALL
ALLSEL,ALL

! NODE AT THE JOINTS AND PIVOT
ASEL,S,LOC,X,0
NSLA,S,1
CM,NBEAM,NODE
NSEL,R,LOC,X,-L
NSEL,R,LOC,Y,0
NBL = NDNEXT(0)
ASEL,S,LOC,X,0
NSLA,S,1
NSEL,R,LOC,X,L
NSEL,R,LOC,Y,0
NBR = NDNEXT(0)
ASEL,S,LOC,X,0
NSLA,S,1
NSEL,R,LOC,X,0
NSEL,R,LOC,Y,0
NBC = NDNEXT(0)
ALLSEL,ALL

!* APPLY BOUNDARY CONDITION AT THE PIVOT
D,NBC,UX,0
D,NBC,UY,0
D,NBC,UZ,0

!* COUPLE THE MOTIONS AT THE JOINTS
CP,NEXT,UX,NDL,NBL
CP,NEXT,UY,NDL,NBL
CP,NEXT,UZ,NDL,NBL
CP,NEXT,UX,NDR,NBR
CP,NEXT,UY,NDR,NBR
CP,NEXT,UZ,NDR,NBR

FINISH

/SOLU
ANTYPE,MODAL

```



```
MODOPT,LANB,NMOD
EQSLV,SPAR
MXPAND,NMOD,,0
LUMPM,0
PSTRES,0
MODOPT,LANB,NMOD,FREQLB,FREQUB,,OFF
SOLVE
FINISH

/POST1
SET,LIST
FINISH
```

---

## Appendix B: List of Publications

### Journal Publications

1. A.P. Lisiewski, **H. Liu**, M. Yu, L. Currano, and D. Gee, Fly-ear inspired micro-sensor for sound source localization in two dimensions, *Journal of the Acoustical Society of America Express Letters*, 129(5): EL166-EL171, 2011.
2. H. Bae, X.M. Zhang, **H. Liu**, and M. Yu, Miniature surface-mountable Fabry-Perot pressure sensor construction with a 45-degree angled fiber, *Optics Letters*, 35 (10): 1701-1703, 2010.
3. **H. Liu**, M. Yu, and X.M. Zhang, Biomimetic optical directional microphone with structurally coupled diaphragms, *Applied Physics Letters* 93(24): 243902, 2008. (Selected for the January 1, 2009 issue of Virtual Journal of Biological Physics Research)
4. **H. Liu**, L. Currano, D. Gee, T. Helms, and M. Yu, Deciphering and mimicking the superior sound localization of the fly. (To be submitted)
5. **H. Liu**, and M. Yu, Dynamic analysis of a pressure sensor diaphragm backed with an cavity. (To be submitted).

### Conference Proceedings

1. L. Sawaqed, **H. Liu**, and M. Yu, Robotic sound source localization using bio-inspired acoustic sensors, *Proceedings of IMECE2012: ASME 2012 International Mechanical Engineering Congress and Exposition*, Houston, Texas, Nov 9-Nov 15, 2012

2. **H. Liu** and M. Yu, Effects of air cavity on fly-ear inspired directional microphones: a numerical study, *Proc. SPIE 7981 (SPIE Smart Materials/NDE): 79811V*, 2011
3. A.P. Lisiewski, **H. Liu**, and M. Yu, Fly ear inspired miniature sound source localization sensor: localization in two dimensions, *Proceedings of IMECE2010: 2010 ASME International Mechanical Engineering Congress and Exposition*, Vancouver, British Columbia, Nov 12-Nov 18, 2010
4. **H. Liu** and M. Yu, A new approach to tackle noise issue in miniature directional microphones: bio-inspired mechanical coupling, *Proc. SPIE 7647 (SPIE Smart Materials/NDE): 76470P*, 2010
5. **H. Liu**, M. Yu, L.J. Currano, and D. Gee, Fly-ear inspired miniature directional microphones: modeling and experimental study, *Proceedings of IMECE2009: 2009 ASME International Mechanical Engineering Congress and Exposition*, Lake Buena, FL, Nov 13-Nov 19, 2009
6. **H. Liu**, M. Yu, and X.M. Zhang, Understanding fly-ear inspired directional microphones, *Proc. SPIE 7292(SPIE Smart Materials/NDE): 72922M*, 2009
7. **H. Liu**, L. Currano, D. Gee, B. Yang, and M. Yu, Fly-ear inspired acoustic sensors for gunshot localization, *Proc. SPIE 7321(SPIE Smart Materials/NDE): 73210A*, 2009
8. L.J. Currano, **H. Liu**, B. Yang, M. Yu, and D. Gee, Microscale implementation of a bio-inspired acoustic localization device, *Proc. SPIE 7321, 73210B*, 2009
9. **H. Liu**, Z. Chen, and M. Yu, Biology-inspired acoustic sensors for sound source localization, *Proc. SPIE 6932(SPIE Smart Materials/NDE): 69322Y*, 2008

## Bibliography

- Arthur, B. J., & Hoy, R. R. (2006). The ability of the parasitoid fly *Ormia ochracea* to distinguish sounds in the vertical plane. *The Journal of the Acoustical Society of America*, 120(3), 1546-1549.
- Asano, F., Asoh, H., & Matsui, T. (2000). Sound source localization and separation in near field. *IEICE Transactions on Fundamentals of Electronics, Communications and Computer Sciences*, E83-A(11), 2286-2294.
- Bar-Cohen, Y. (2006). Biomimetics—using nature to inspire human innovation. *Bioinspiration & Biomimetics*, 1, P1.
- Benesty, J., Chen, J., & Huang, Y. (2004). Time-delay estimation via linear interpolation and cross correlation. *Speech and Audio Processing, IEEE Transactions on*, 12(5), 509-519.
- Benesty, J., Chen, J., & Huang, Y. (2008). *Microphone array signal processing* (Vol. 1): Springer Verlag.
- Beranek, L. L. (1954). *Acoustics* (Vol. 6): McGraw-Hill New York.
- Bhushan, B. (2009). Biomimetics: lessons from nature—an overview. *Philosophical Transactions of the Royal Society A: Mathematical, Physical and Engineering Sciences*, 367(1893), 1445-1486.
- Bleckmann, H., Schmitz, H., & Von der Emde, G. (2004). Nature as a model for technical sensors. *Journal of Comparative Physiology A: Neuroethology, Sensory, Neural, and Behavioral Physiology*, 190(12), 971-981.
- Brandstein, M. S., & Ward, D. B. (2001). *Microphone arrays: signal processing techniques and applications*: Springer Verlag.
- Brooks, T. F., & Humphreys, W. M. (1999). Effect of directional array size on the measurement of airframe noise components. *AIAA paper*, 1958, 1999.
- Cade, W. (1975). Acoustically Orienting Parasitoids: Fly Phonotaxis to Cricket Song. *Science*, 190(4221), 1312-1313.
- Chen, C.-C., & Cheng, Y.-T. (2012). Physical Analysis of a Biomimetic Microphone With a Central-Supported (C-S) Circular Diaphragm for Sound Source Localization. *Sensors Journal, IEEE*, 12(5), 1504-1512. doi: 10.1109/jsen.2011.2173931
- Csermak, B. (2000). A primer on a dual microphone directional system. *Hearing Review*, 7(1), 56-60.

- Cui, W., Bicen, B., Hall, N., Jones, S. A., Degertekin, F. L., & Miles, R. N. (2006, 2006). *Optical Sensing Inadirectional Memsmicrophone Inspired by the Ears of the Parasitoid Fly, Ormia Ochracea*. Paper presented at the Micro Electro Mechanical Systems, 2006. MEMS 2006 Istanbul. 19th IEEE International Conference on.
- Dowell, E. H., Gorman III, G. F., & Smith, D. A. (1977). Acoustoelasticity: General theory, acoustic natural modes and forced response to sinusoidal excitation, including comparisons with experiment. *Journal of Sound and Vibration*, 52(4), 519-542. doi: 10.1016/0022-460x(77)90368-6
- Eaton, W. P., & Smith, J. H. (1997). Micromachined pressure sensors: review and recent developments. *Smart Materials and Structures*, 6(5), 530.
- Gay, S. L., & Benesty, J. (2000). *Acoustic signal processing for telecommunication*: Springer.
- Gladwell, G. M. L., & Zimmermann, G. (1966). On energy and complementary energy formulations of acoustic and structural vibration problems. *Journal of Sound and Vibration*, 3(3), 233-241. doi: 10.1016/0022-460x(66)90092-7
- Gorman, D. G., Reese, J. M., Horáček, J., & Dedouch, K. (2001). Vibration analysis of a circular disc backed by a cylindrical cavity. *Proceedings of the Institution of Mechanical Engineers, Part C: Journal of Mechanical Engineering Science*, 215(11), 1303-1311. doi: 10.1243/0954406011524685
- Grattan, L. S., & Meggitt, B. T. (2000). *Optical Fiber Sensor Technology*: Springer.
- Guy, R. W. (1979). The response of a cavity backed panel to external airborne excitation: A general analysis. *The Journal of the Acoustical Society of America*, 65(3), 719-731.
- Hall, N. A., Bicen, B., Jeelani, M. K., Lee, W., Qureshi, S., Degertekin, F. L., & Okandan, M. (2005). Micromachined microphones with diffraction-based optical displacement detection. *The Journal of the Acoustical Society of America*, 118(5), 3000-3009.
- Hall, N. A., & Degertekin, F. L. (2002). Integrated optical interferometric detection method for micromachined capacitive acoustic transducers. *Applied Physics Letters*, 80(20), 3859-3861.
- Hall, N. A., Okandan, M., Littrell, R., Bicen, B., & Degertekin, F. L. (2007). Micromachined optical microphone structures with low thermal-mechanical noise levels. *The Journal of the Acoustical Society of America*, 122(4), 2031-2037.
- Hariharan, P. (2003). *Optical Interferometry, 2e*: Academic Press.

- Harris, J. D., & Sergeant, R. L. (1971). Monaural/Binaural Minimum Audible Angles for a Moving Sound Source. *Journal of Speech, Language, and Hearing Research*, *14*(3), 618-629.
- Hoy, R., Popper, A., & Fay, R. (1998). *Comparative hearing: Insects*: Springer Verlag.
- Hoy, R., & Robert, D. (1996). Tympanal hearing in insects. *Annual review of entomology*, *41*(1), 433-450.
- Kennedy, R. A., Abhayapala, T. D., & Ward, D. B. (1998). Broadband nearfield beamforming using a radial beampattern transformation. *Signal Processing, IEEE Transactions on*, *46*(8), 2147-2156.
- Lisiewski, A. P., Liu, H. J., Yu, M., Currano, L., & Gee, D. (2011). Fly-ear inspired micro-sensor for sound source localization in two dimensions. *The Journal of the Acoustical Society of America*, *129*(5), EL166-EL171.
- Liu, H., Yu, M., & Zhang, X. (2008). Biomimetic optical directional microphone with structurally coupled diaphragms. *Applied Physics Letters*, *93*, 243902.
- Mason, A., Oshinsky, M., & Hoy, R. (2001). Hyperacute directional hearing in a microscale auditory system. *Nature*, *410*(6829), 686-690.
- Meirovitch, L. (2001). *Fundamentals of vibrations*: McGraw-Hill New York.
- Michelsen, A., & Larsen, O. N. (2008). Pressure difference receiving ears. *Bioinspiration & Biomimetics*, *3*(1), 011001.
- Michelsen, A., Popov, A. V., & Lewis, B. (1994). Physics of directional hearing in the cricket *Gryllus bimaculatus*. *Journal of Comparative Physiology A: Neuroethology, Sensory, Neural, and Behavioral Physiology*, *175*(2), 153-164. doi: 10.1007/bf00215111
- Miles, R. N., Robert, D., & Hoy, R. R. (1995). Mechanically coupled ears for directional hearing in the parasitoid fly *Ormia ochracea*. *Journal of the Acoustical Society of America*, *98*(6), 3059-3070.
- Miles, R. N., Su, Q., Cui, W., Shetye, M., Degertekin, F. L., Bicen, B., . . . Hall, N. (2009). A low-noise differential microphone inspired by the ears of the parasitoid fly *Ormia ochracea*. *The Journal of the Acoustical Society of America*, *125*, 2013.
- Muller, P., & Robert, D. (2001). A shot in the dark: the silent quest of a free-flying phonotactic fly. *Journal of experimental biology*, *204*(6), 1039-1052.
- Olson, H. F. (1958). *Dynamical analogies*: Van Nostrand.

- Ono, N., Arita, T., Senjo, Y., & Ando, S. (2005, 5-9 June 2005). *Directivity steering principle for biomimicry silicon microphone*. Paper presented at the Solid-State Sensors, Actuators and Microsystems, 2005. Digest of Technical Papers. TRANSDUCERS '05. The 13th International Conference on.
- Ono, N., Saito, A., & Ando, S. (2003, 8-12 June 2003). *Design and experiments of biomimicry sound source localization sensor with gimbal-supported circular diaphragm*. Paper presented at the TRANSDUCERS, Solid-State Sensors, Actuators and Microsystems, 12th International Conference on, 2003.
- Oshinsky, M. L., & Hoy, R. R. (2002). Physiology of the Auditory Afferents in an Acoustic Parasitoid Fly. *The Journal of Neuroscience*, 22(16), 7254-7263.
- Pan, J. (1992). The forced response of an acoustic-structural coupled system. *The Journal of the Acoustical Society of America*, 91(2), 949-956.
- Popper, A., & Fay, R. (2005). *Sound source localization*: Springer Verlag.
- Pretlove, A. J. (1965). Free vibrations of a rectangular panel backed by a closed rectangular cavity by a closed rectangular cavity. *Journal of Sound and Vibration*, 2(3), 197-209. doi: 10.1016/0022-460x(65)90108-2
- Pretlove, A. J. (1966). Forced vibrations of a rectangular panel backed by a closed rectangular cavity. *Journal of Sound and Vibration*, 3(3), 252-261. doi: 10.1016/0022-460x(66)90094-0
- Pretlove, A. J., & Craggs, A. (1970). A simple approach to coupled panel-cavity vibrations. *Journal of Sound and Vibration*, 11(2), 207-IN201. doi: 10.1016/s0022-460x(70)80064-5
- Qaisi, M. I. (1988). Free vibrations of a rectangular plate-cavity system. *Applied Acoustics*, 24(1), 49-61. doi: 10.1016/0003-682x(88)90070-9
- Rajalingham, C., Bhat, R., & Xistris, G. (1995). Natural vibration of a cavity backed rectangular plate using a receptor-rejector system model. *Journal of vibration and acoustics*, 117(4), 416-423.
- Rajalingham, C., Bhat, R. B., & Xistris, G. D. (1998). Vibration of circular membrane backed by cylindrical cavity. *International Journal of Mechanical Sciences*, 40(8), 723-734. doi: 10.1016/s0020-7403(97)00065-9
- Robert, D., Amoroso, J., & Hoy, R. R. (1992). The evolutionary convergence of hearing in a parasitoid fly and its cricket host. *Science*, 258(5085), 1135-1137. doi: 10.1126/science.1439820

- Robert, D., & Göpfert, M. C. (2002). Novel schemes for hearing and orientation in insects. *Current opinion in neurobiology*, 12(6), 715-720. doi: 10.1016/s0959-4388(02)00378-1
- Robert, D., Miles, R. N., & Hoy, R. R. (1996). Directional hearing by mechanical coupling in the parasitoid fly *Ormia ochracea*. *Journal of Comparative Physiology A: Neuroethology, Sensory, Neural, and Behavioral Physiology*, 179(1), 29-44. doi: 10.1007/bf00193432
- Robert, D., Miles, R. N., & Hoy, R. R. (1998). Tympanal mechanics in the parasitoid fly *Ormia ochracea*: intertympanal coupling during mechanical vibration. *Journal of Comparative Physiology A: Neuroethology, Sensory, Neural, and Behavioral Physiology*, 183(4), 443-452. doi: 10.1007/s003590050270
- Robert, D., Miles, R. N., & Hoy, R. R. (1999). Tympanal hearing in the sarcophagid parasitoid fly *Emblemasoma* sp.: the biomechanics of directional hearing. *Journal of experimental biology*, 202(14), 1865-1876.
- Ryan, J. G., & Goubran, R. A. (2000). Array optimization applied in the near field of a microphone array. *Speech and Audio Processing, IEEE Transactions on*, 8(2), 173-176.
- Saito, A., Ono, N., & Ando, S. (2002, 5-7 Aug. 2002). *Micro gimbal diaphragm for sound source localization with mimicking Ormia Ochracea*. Paper presented at the SICE 2002. Proceedings of the 41st SICE Annual Conference.
- Touse, M., Sinibaldi, J., Simsek, K., Catterlin, J., Harrison, S., & Karunasiri, G. (2010). Fabrication of a microelectromechanical directional sound sensor with electronic readout using comb fingers. *Applied Physics Letters*, 96, 173701.
- Vincent, J. F. V., Bogatyreva, O. A., Bogatyrev, N. R., Bowyer, A., & Pahl, A. K. (2006). Biomimetics: its practice and theory. *Journal of the Royal Society Interface*, 3(9), 471-482.
- Walker, T. J. (1993). Phonotaxis in female *Ormia ochracea* (Diptera: Tachinidae), a parasitoid of field crickets. *Journal of Insect Behavior*, 6(3), 389-410. doi: 10.1007/bf01048119
- Wild, G., & Hinckley, S. (2008). Acousto-ultrasonic optical fiber sensors: overview and state-of-the-art. *Sensors Journal, IEEE*, 8(7), 1184-1193.
- Yager, D. D. (1999). Structure, development, and evolution of insect auditory systems. *Microscopy Research and Technique*, 47(6), 380-400. doi: 10.1002/(sici)1097-0029(19991215)47:6<380::aid-jemt3>3.0.co;2-p



- Yoo, K., Gibbons, C., Su, Q. T., Miles, R. N., & Tien, N. C. (2002). Fabrication of biomimetic 3-D structured diaphragms. *Sensors and Actuators A: Physical*, 97–98(0), 448-456. doi: 10.1016/s0924-4247(01)00808-1
- Yovel, Y., Falk, B., Moss, C. F., & Ulanovsky, N. (2010). Optimal Localization by Pointing Off Axis. *Science*, 327(5966), 701-704. doi: 10.1126/science.1183310
- Yu, M. (2002). *Fiber-optic sensor systems for acoustic measurements*. Doctor of Philosophy, University of Maryland.
- Yu, M., & Balachandran, B. (2005). Sensor diaphragm under initial tension: linear analysis. *Experimental mechanics*, 45(2), 123-129.
- Zheng, Y. R., Goubran, R. A., & El-Tanany, M. (2004). Robust near-field adaptive beamforming with distance discrimination. *Speech and Audio Processing, IEEE Transactions on*, 12(5), 478-488.